Université d'Ottawa · University of Ottawa

A 3-D Laser Range Scanner Based on the Self-Mixing Effect in a Laser Diode

by:

Eric Gagnon, B.A.Sc.

A thesis submitted to the
School of Graduate Studies and Research
in partial fulfillment of the requirements for the degree of

Master of Applied Science

Ottawa-Carleton Institute for Electrical Engineering
Department of Electrical Engineering
Faculty of Engineering
University of Ottawa
April 15, 1997

Abstract

In the last few decades, the field of artificial vision has witnessed an overwhelming growth through academic research and increasing industry demands. One of the more exciting and promising developments in the field has taken form in the 3D vision paradigm. With the advent of 3D vision, the possibility to directly map in three dimensions the shape of an object has opened a wealth of new possibilities.

The purpose of this work is to present the theory and design of a low-cost, portable and accurate 3D laser range scanning system. The system allows direct acquisition of 3D images from a scene. The proposed 3D imaging method uses a laser beam for measuring the distance to a target in a fixed point and computing its (X, Y, Z) coordinate in space. Through deflection of this beam using small motorized mirrors, a distant surface may be scanned into a full 3D range image.

Unlike conventional ranging systems, the present design uses a single semiconductor laser diode serving as both a laser source and detector. Laser ranging is achieved through frequency modulation of the laser with time-of-flight coherent detection, based on the self-mixing effect in a laser diode. This allows for unambiguous range measurement capabilities over several meters. The benefits of this sensing approach over existing laser-based systems are numerous, and include:

- Very low cost solution to the ranging problem.
- No need for external optical sensing elements.
- Coaxial source and detector configuration eliminates shadowing problems.
- Coherent detection yields constant ranging error over useful workspace.
- Velocity and range information available from a single measurement.
- Interferometric scale measurements possible in fixed-frequency regime.

Abstract

The purpose of this work is to present the theory and design of a low-cost, portable and accurate 3D laser range scanning system. The system allows direct acquisition of 3D images from a scene. The proposed 3D imaging method uses a laser beam for measuring the distance to a target in a fixed point and computing its (X,Y,Z) coordinates in space. Through deflection of this beam using small motorized mirrors, a distant surface may be scanned into a full 3D range image. Unlike conventional ranging systems, the present design uses a single semiconductor laser diode serving as both a laser source and detector. Laser ranging is achieved through frequency modulation of the laser with time-of-flight coherent detection, based on the self-mixing effect in a laser diode. This allows for unambiguous range measurement capabilities over several meters.

Acknowledgments

I would like to acknowledge the support of my thesis supervisor, Dr. Jean-François Rivest, from the University of Ottawa throughout the course of this work.

Partial funding was provided in the form of equipment and access to facilities by the National Research Council of Canada, at the Institute for Information Technology, Ottawa, Ontario, Canada. More specifically, I would like to thank Mr. Jacques Domey, Mr. François Blais and Mr. Michael Greenspan from the NRC for their help and support.

I also wish to duly acknowledge the personal financial support provided by an NSERC Industrial Postgraduate Scholarship partially funded by SPAR Aerospace Limited (Spar Space Systems), Brampton, Ontario. I would like to thank Mr. John Ballantyne, Mr. Alan Wilson, and Dr. Loris Gregoris from SPAR for their help and support.

Contents

List of Figures

Chapter 1

Introduction

1.1 Purpose

The purpose of this work is to present the theory and design of a low-cost, portable and accurate three-dimensional laser range scanner system. This range scanner, or range camera allows the direct acquisition of the 3D coordinates of sampled points over the surface of objects in a scene. Figure 1.1 illustrates the principle. By scanning the surface of these objects in a raster scan fashion, a 3D range image, or point cloud representing their surface is obtained [1] [2]. This data may then be processed by using techniques from the emerging 3D vision paradigm. As described in [1], applications of 3D range imagery include: shape recognition, 3D reproduction (stereolithography), rapid prototyping [3], shape editing, 3D facsimile transmission, mould printing, reverse engineering, and 3D object database compression. Other applications include: 3D imaging of the human body [4], object tracking [5] [6], differential inspection of shapes [7], robot control [8], and remote teleoperation [9].

1.2 Contributions

A 3D laser range scanning system was devised and implemented based on a novel laser ranging principle involving the self-mixing effect in a laser diode. This work constitutes only the second known implementation[10] of a 3D laser range scanner based on this principle. A study of the self-mixing effect in laser diodes was carried out and an extension to the existing theory was developed in order to obtain theoretical curves matching the experimental curves obtained. Considerable insight into the self-mixing effect was

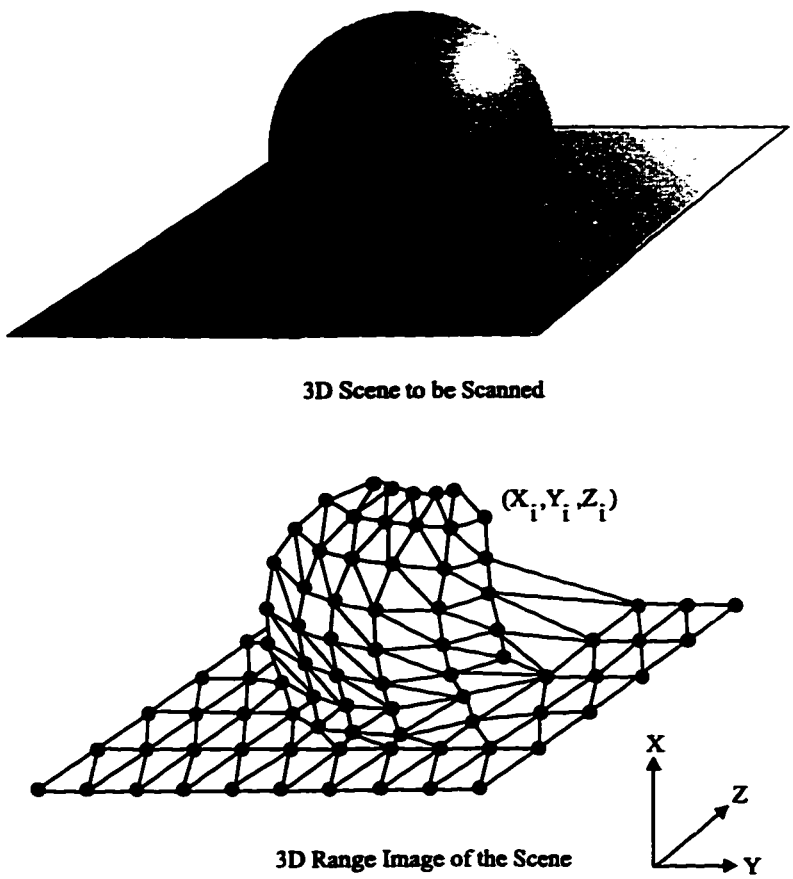

Figure 1.1: 3D imaging. 3D coordinates of a series of points over the surface of a scene are acquired, forming a 3D range image.

gained from the analysis of the developed theoretical model. Consequently, the 3D laser range scanner prototype was operated at a considerably higher laser diode modulation frequency than first planned in order to solve a mechanical sensitivity problem. Four novel circuits were devised to control the functions of the low-cost laser range scanner. A high accuracy ($\pm 1 \mu A$) circuit with protection features was designed to drive the laser diode and amplify the signal from the internal monitor photodiode. A high accuracy temperature controller ($\pm 0.001^{o}C$ accuracy) was designed based on a thermoelectric device for temperature stabilization of the laser diode for high frequency stability. A signal conditioning circuit was designed to enhance the detected interferometric signal for digital processing. A high stability digital triangular signal generator circuit was designed as the signal source for the modulation. Finally, a new signal processing algorithm was devised to automatically detect the mode hop spacing and calculate target range and velocity.

1.3 The 3D Vision Problem

Industrial applications constantly demand new solutions to challenging problems. The field of robotics in particular has witnessed over the last few decades a tremendous increase in the use of artificial vision in solving new and classical problems. Autonomous machine navigation, for one, has seen a transition from "blind navigation" where electromechanical and simple non-contact sensors [11] [12] [13] were used to provide depth cues, to full-fledged artificial vision systems [14]. In general, some problems lend themselves well to the 3D vision paradigm. A few of these problems are: robot navigation, automated surface and shape inspection, shape recognition, reverse engineering, automated CAD modeling, rapid prototyping, shape tracking, and surface following. Applications like these motivated a considerable amount of research in developing vision systems and algorithms over the years.

1.3.1 Passive 3D Reconstruction

Until recently, CCD cameras were exclusively the tool of choice for artificial vision researchers due in part to their low-cost, availability and ease of use. Over the last few decades, a considerable amount of research on 3D vision was carried out based on passive camera systems [15]. Most of these techniques involve some form of optical triangulation. Figure 1.2 illustrates an example of such a passive triangulation system based on a stereo camera pair. The major hurdles facing passive triangulation imaging systems

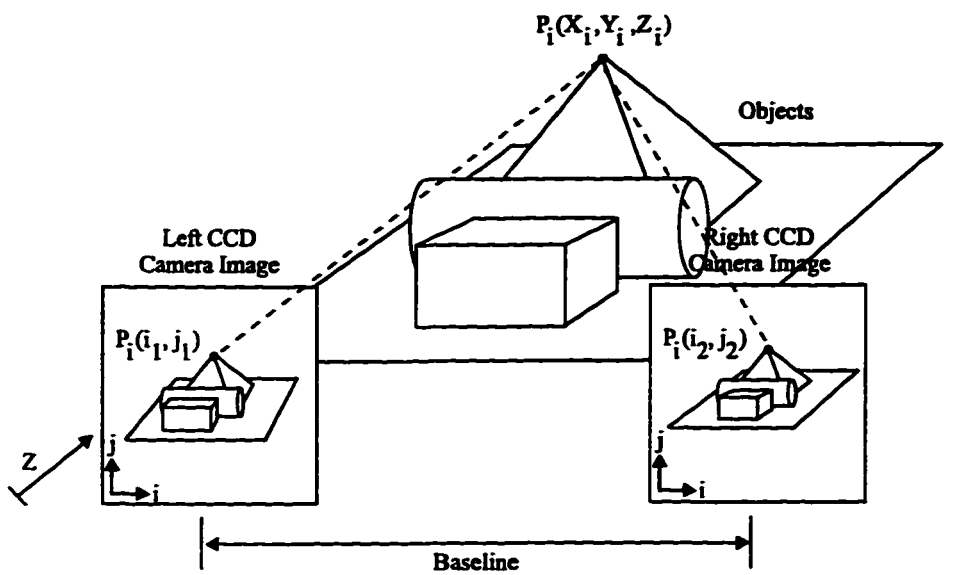

Figure 1.2: Stereo vision. Two CCD cameras are offset by a known baseline distance. By identifying the same point in the two offset images, range information may be extracted through triangulation. A major problem is the automatic identification of matching points in both images.

include:

- Uncontrolled scene lighting.
- Depth-of-field limitation (focus).
- Limited accuracy over large distances.
- Shadowing problems.
- Increasing triangulation errors with range.
- Difficult point-correlation problem (sometimes impossible).
- Scene-dependent performance.
- Large computation time.
- Use of scene markers not always practical.

1.3.2 Laser Range Scanning

In the late 70's, efforts were placed in devising systems capable of directly acquiring 3D information from a scene without exhibiting the constraints of conventional stereo vision. The approaches were based on the use of laser beams to extract a single point distance measurement either by triangulation or by time-of-flight [19] [20]. By deflecting the laser beam through a beam steering unit, or simply by expanding the beam into a sheet of light through a cylindrical lens, it is possible to acquire the distance to an arbitrary surface point in a 3D workspace. The full 3D coordinates of a sequence of points on the surface of an object may be obtained by sweeping the surface while acquiring discrete range samples. This is illustrated in Figure 1.3. The laser beam measures the distance ρ to the target at discrete intervals while being deflected, or scanned over the surface. A point grid is then formed, representing the scene's surface information. The use of the laser beam effectively eliminates the point correlation problem, the focusing problem, and the lighting problem as the laser serves both as its own light source and detection mechanism. Several approaches have been undertaken to obtain range information using laser beams. Mainly, they fall under two categories: triangulation, and time-of-flight.

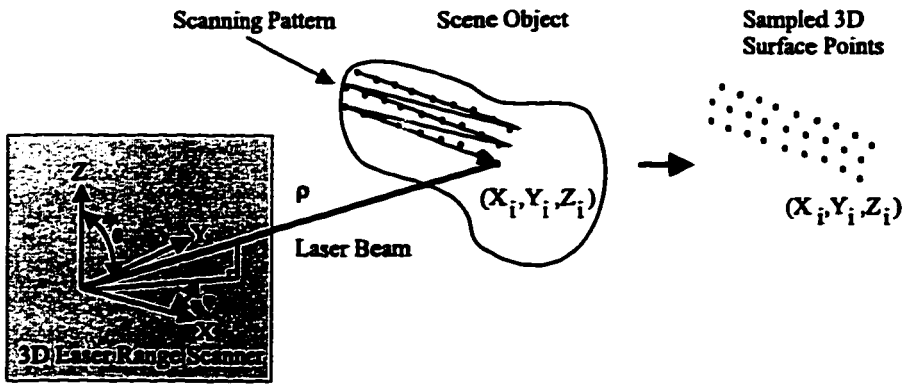

Figure 1.3: Laser range scanning. A laser beam measures the distance ρ to the target at a given point. By deflecting the beam, a grid of 3D points may be sampled over the surface.

1.4 Existing Laser-Based Approaches

1.4.1 Triangulation

Laser triangulation [19] [20] was demonstrated as an effective means to obtain range information from a target. A laser beam is first transmitted at known departure angles θ, ϕ as illustrated in Figure 1.4. The beam is then reflected off a distant target, re-enters the camera and is received by an optical lateral deflection sensor, such as a linear CCD array. The distance to the object will dictate the lateral position p of the laser spot on the CCD array.

Some limitations of this system include limited range for a given triangulation base (baseline). Also, since the laser light is emitted from one side and received from the other, some geometries such as sharp edges reveal a "shadowing" problem where some points visible from the point of view of the laser source are not visible from the point of view of the detector. This results in occlusion of the data. Nonetheless, this triangulation technique is widespread due in part to its simplicity, and ease of implementation.

Another triangulation-based system is illustrated in Figure 1.5. The system uses a sheet of light and a CCD camera. The sheet of light is generated by passing a laser beam through a cylindrical lens and projecting it onto the scene. By analyzing the shape of the reflected laser line captured by the CCD camera, 3D information may be obtained from the 2D camera image

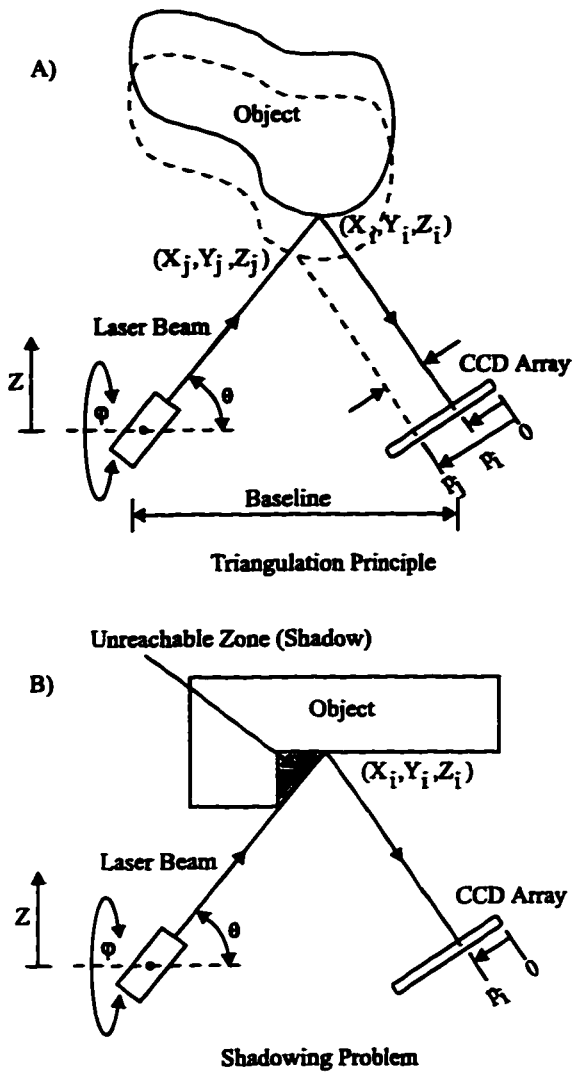

Figure 1.4: Laser triangulation. A) A laser beam is transmitted at known departure angles θ, ϕ from the scanner, and is then reflected off the surface of an object. The distance to the object dictates the lateral position p of the returning laser spot onto the CCD array. B) Shadowing problem associated with triangulation. For certain geometries, the offset between the laser source and the detector results in occluded points that cannot be seen by both the source and the detector.

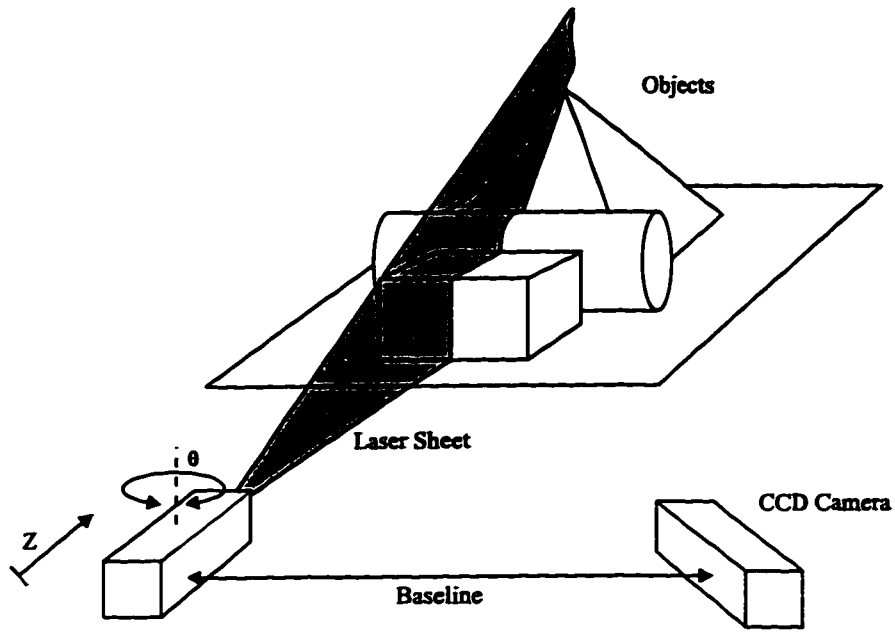

Figure 1.5: Line-based laser triangulation. A laser beam is converted into a sheet of light with a cylindrical lens. The sheet of light is projected onto the scene. By analyzing the shape of the reflected laser line captured by the CCD camera, 3D information may be obtained from the 2D camera image for an entire row of points at once. A single scanning axis is necessary to sweep a volume.

for an entire row of points at once. This system is similar to the previous single-spot triangulation system, but the sheet simulates a series of superimposed laser beams transmitted at the same time. Triangulation may thus be performed on the entire line as opposed to one spot at a time. A single scanning axis is necessary to sweep a volume.

Overall, laser triangulation systems offer the following advantages over passive stereo vision:

- No scene lighting problem.
- No point-correlation problem.
- Performance less sensitive to scene conditions.
- Faster computation time.
- No need for scene markers.
- Single camera or CCD array required.

Remaining problems include:

- Depth-of-field limitation.
- Limited accuracy over large distances.
- Shadowing problems.
- Increasing triangulation errors with range.
- Laser speckle.

Despite the remaining limitations, triangulation-based systems are relatively popular due to their low-cost and good close range accuracy.

1.4.2 Time-of-flight

A different approach to the ranging problem is based on measuring the time between the departure of a laser pulse and its arrival back to the camera after being reflected off a distant target [21]. Figure 1.6 illustrates the scenario.

Advantages of time-of-flight systems over laser-based triangulation systems include:

- Less sensitivity to depth-of-field limitation.
- Better accuracy over long distances.

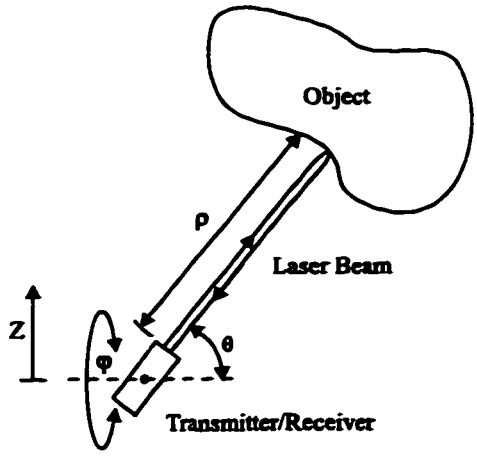

Figure 1.6: Time-of-flight ranging. A laser beam pulse is sent at known departure angles θ, ϕ. The range measurement ρ is obtained by determining the time required for the laser pulse to travel to and from the target.

- Constant ranging errors over workspace.
- Faster computation time.
- Coaxial source and detector eliminating shadowing problem.

Problems include:

- Reduced close range accuracy.
- Some implementations require expensive electronics.
- Some coherent detection methods result in ambiguous range measurements.
- Laser speckle.

Several different techniques exist to measure the laser pulse round-trip time interval. The most obvious one is simply to emit a laser pulse and directly measure the time interval before a sensor detects the reflected beam. This proves to be an effective method over very large distances, but poses a problem for close ranges. This is due to the extremely short times between the transmission and reception of the laser pulse of the order of picoseconds.

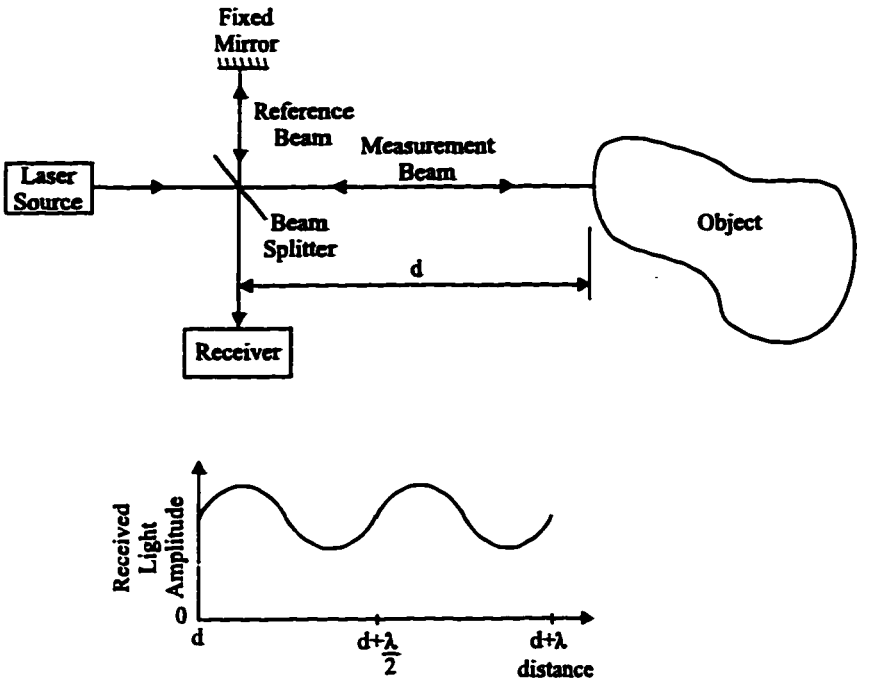

Figure 1.7: Interferometer. A laser beam is divided into a reference and a measurement beam. The difference in paths traveled by both beams results in a relative phase shifts between the two coherent beams. Constructive and destructive interference give rise to periodic amplitude modulation as a function of the target distance. The period of the fluctuation corresponds to a target displacement of $\frac{\lambda}{2}$, where λ is the wavelength of the laser light.

This calls for very sophisticated and expensive electronic circuitry. These interval timing systems are mainly used in long range sensors.

A second detection method used to determine the time of flight, known as coherent detection relies on the use of the self-interference property of coherent light [15]. The motivation behind this detection method is to reduce the high speed timing requirements of the detection circuitry. One of the earliest form of coherent detection, and certainly the best known is the interferometer. In an interferometer, a laser light source is separated into a reference beam and a measurement beam as shown in Figure 1.7. The measurement beam is reflected off a target of interest and is coherently mixed with the reference beam. Periodic intensity fluctuations occur when the rel-

ative phase shift between the two beams vary in multiples of the wavelength of the light, due to constructive and destructive interference. This allows measurement accuracies in the sub-wavelength range. The major problem associated with this technique, however, appears in taking range measurements longer than half of the wavelength of the laser light (i.e. He-Ne laser wavelength = 632.8 nm). Since the interference pattern is periodic, keeping count of the number of periodic fluctuations encountered is necessary in order to obtain an absolute measurement over a larger distance. This causes problems in identifying the absolute zero of the measurement. Another problem is posed by the accuracy of the period count in the presence of noise. Attempts have been made in devising absolute interferometric sensors based on multiple laser sources with different wavelengths [16] [17] whereby the processing of the two or more periodic fluctuations simultaneously yields a unique signal over a much larger distance. The useful range of these multiple-wavelength interferometers, although increased, is still not long enough to be useful in many industrial applications.

Other researchers have investigated the use of amplitude modulation (AM) in an attempt to increase the useful range of interferometric detection [15]. Figure 1.8 illustrates the principle. Here, the intensity of a laser is modulated by a time-varying periodic signal (i.e. sine wave) whose wavelength is considerably longer than the wavelength of the laser light. The phase shift of the detected AM envelope from the received signal with respect to that of the transmitted signal is proportional to the target distance. The problems of this technique include limited dynamic range, and laser speckle.

Frequency modulation (FM) systems were also devised [18] to resolve the time of flight measurement problem as illustrated in Figure 1.9. Here, the frequency of the laser light transmitted towards a fixed target is varied linearly through a triangular FM modulation signal. Due to the round-trip propagation time, the reflected beam has an instantaneous frequency slightly different than the instantaneous frequency of the reference light beam. Consequently, an envelope beat signal with frequency equal to the frequency difference between the light beams is observed at the output, proportional to the target distance. This principle is similar to the well-known Doppler effect, except that the frequency shift is induced by the time-varying frequency of the source instead of the moving target. The problems of this technique include limited dynamic range, and laser speckle.

Finally, an interesting twist on the FM ranging technique shown in Figure 1.10 appeared when researchers first investigated the effects of using the laser cavity itself in order to perform the mixing of a reference and a

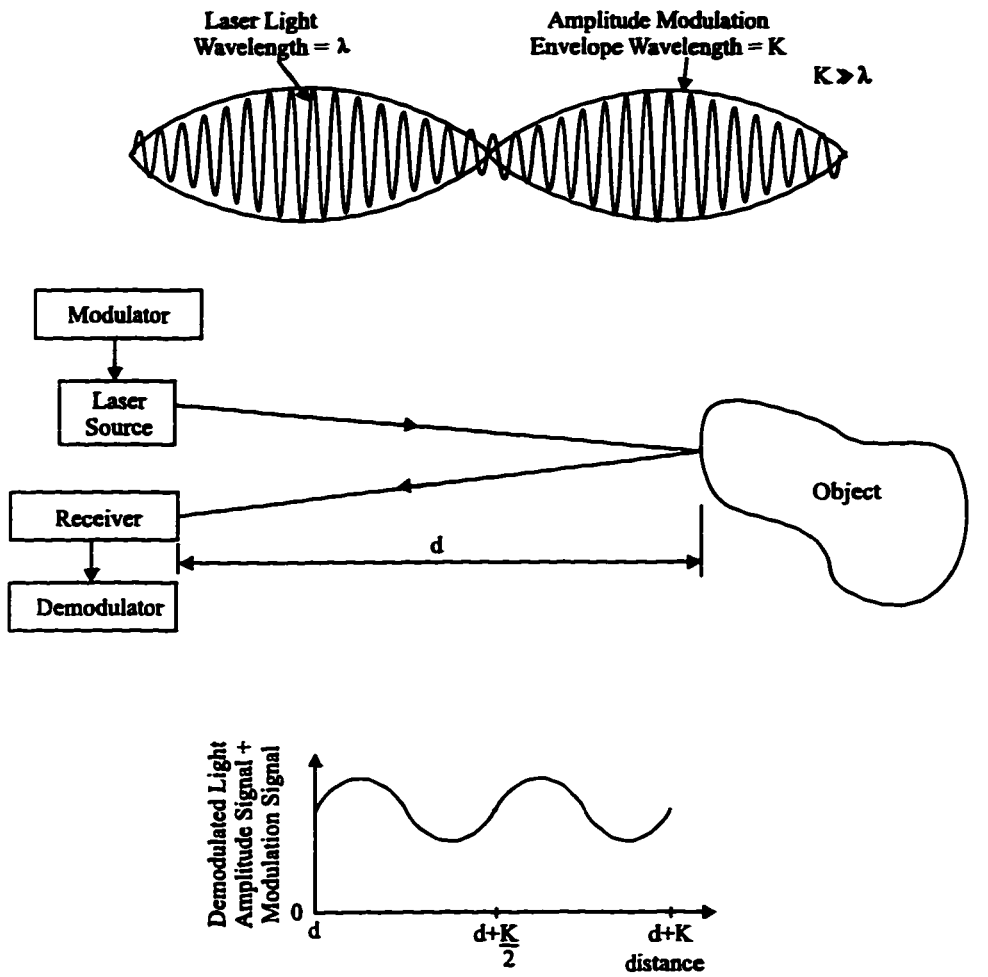

Figure 1.8: Amplitude modulation ranging. In order to increase the useful range of the interferometer, the laser beam intensity is modulated by a lower frequency sinusoidal signal. The phase shift of this demodulated light intensity signal is then used for range computation. The useful range of the technique is thereby increased.

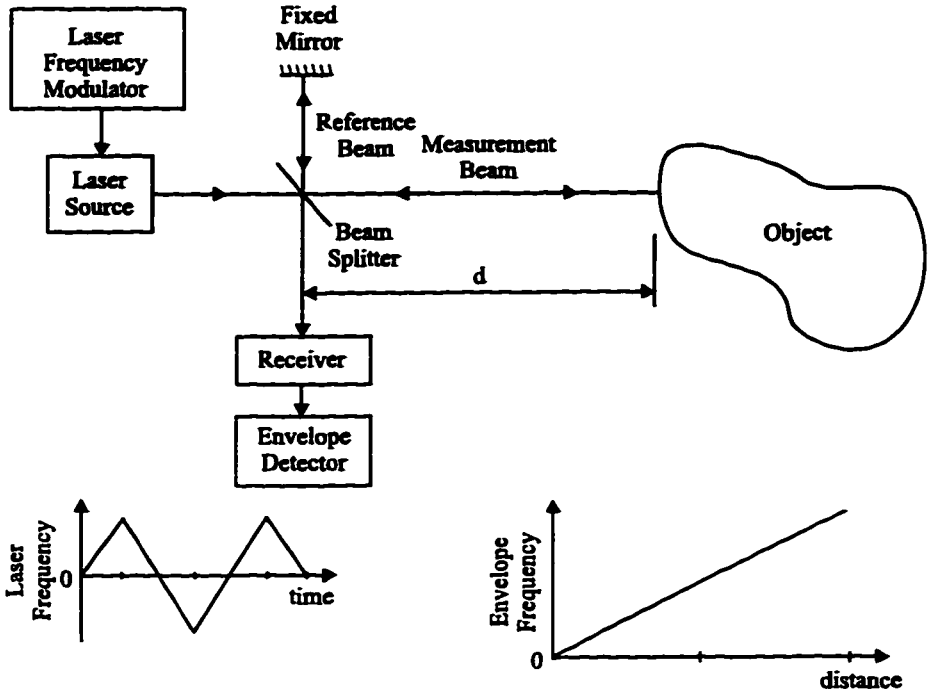

Figure 1.9: Frequency modulation ranging. The frequency of the laser light transmitted towards a fixed target is varied linearly through a triangular FM modulation signal. Due to the round-trip propagation time, the reflected beam has an instantaneous frequency slightly different than the instantaneous frequency of the reference light beam. Consequently, an envelope beat signal with frequency equal to the frequency difference between the light beams is observed at the output, proportional to the target distance.

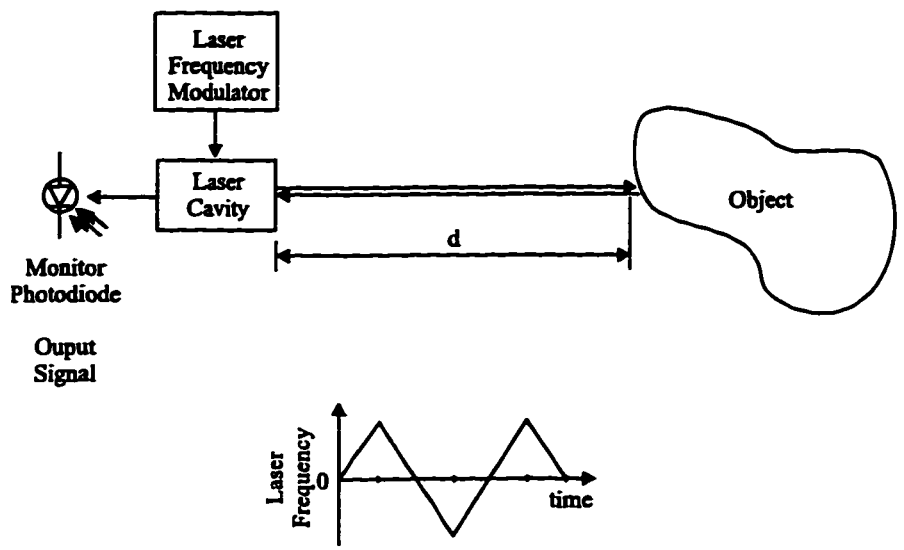

Figure 1.10: Frequency modulation ranging with the self-mixing effect. The frequency of the laser light transmitted towards a fixed target is varied linearly through a triangular FM modulation signal. The reflected beam is mixed inside the laser cavity itself, giving rise to fundamental changes in the emitted laser light properties. By taking advantage of the change of some of these properties, it is possible to compute the range and velocity of the target simply by processing the laser light intensity signal.

measurement beam [22]. This is possible by allowing the emitted light to be reflected or backscattered to the laser source. It was observed that peculiar asymetries appeared in the intensity interference signal unlike what is observed in conventional interferometry. The phenomenon was dubbed the "Self-Mixing Effect". With the advent of low-cost semiconductor laser diodes, much interest has developed in using the laser diodes as sources and detectors. Laser diodes usually have an internal photodiode used for power output regulation. By using this internal power monitoring photodiode, no added external components are needed to monitor the laser output power fluctuations. As a result, extremely small, compact and versatile sensors capable of performing high accuracy measurements are conceivable.

1.5 Proposed Method

The prototype 3D imaging system described in this work is based on time-of-flight laser ranging. As described previously, this laser-based technique offers advantages over conventional passive stereo vision which is limited by such problems as point matching, focusing, increasing triangulation errors, scene lighting, and shadowing.

The time-of-flight system uses coherent detection and FM ranging based on the self-mixing effect in a laser diode. This allows for unambiguous range measurement capabilities over several meters, unlike the wavelength range limited interferometric systems. A simple semiconductor laser diode is used, serving as both the laser source and sensor. This results in a very low-cost sensor, with coaxial source and sensing axis. Shadowing problems associated with laser-based triangulation systems are therefore eliminated. No external optical sensing elements (i.e. CCD array) are required. Moreover, because of the coherent detection technique, errors remain constant over the useful workspace unlike in laser-based triangulation systems. Another added benefit of using the self-mixing effect lies in the possibility to obtain velocity as well and range information at the same time. Interferometric scale measurements are also possible by using the system in a fixed-frequency regime.

Chapter 2

Literature Review

2.1 Self-Mixing Effect

Intensity fluctuations in a Helium-Neon (He-Ne) laser due to external feedback were first reported by J.D. Rudd in 1968 [22]. Rudd proposed the use of the He-Ne laser not only as a light source but also as a mixer-oscillator in measuring the Doppler velocity of scattering particles. Since this initial report by Rudd, a number of researchers have investigated the self-mixing effect and its potential applications.

In essence, the self-mixing effect describes the situation whereby laser light emitted by a laser source is allowed to re-enter the lasing cavity after being reflected by an external diffuse or specular target. The light re-entering the cavity gives rise to interference with the laser light inside the cavity. Similarly to conventional interferometry, fringe shifts appear as the phase of the external light is varied with respect to that of the source. The modulation depth of the light is also comparable to that observed in a conventional interferometer. The similarities with a conventional interferometer however end here. Indeed, the self-mixing interference exhibits some rather unique properties. Interference patterns were observed even when the optical path difference (OPD) between the laser and the target was well beyond the coherence length[1] of the solitary used [23], the conventional limit of interferometric systems. The intensity modulation waveform obtained as a result of feedback was also observed to be sawtooth-like. The orientation of the sawtooth waveform was also observed to be asymmetric with respect to the direction of motion of the external reflector [24]. The laser light output

[1] Upper bound on the maximum range beyond which light interference is no longer possible.

intensity modulation as a result of feedback was observed both from the rear and the front facet of a lasing cavity. The measured waveforms exhibited a sign inversion with respect to each other [25].

2.1.1 Early Theories

In order to explain these unique properties, a number of theoretical formulations have been described. Rudd [22] first formulated a simple feedback amplifier model for analyzing the intensity modulation observed in a He-Ne laser. Churnside [27] [28], in 1984, studied laser Doppler velocimetry using the self-mixing effect in a modulated CO_2 laser. He termed the self-mixing effect as "backscatter modulation" with diffusely reflecting targets. In his experiments, backscattered light from a CO_2 gas laser was actively mixed into the cavity of the laser. The light was reflected by means of a diffuse rotating reflective target. The modulation depth of the Doppler signal was measured under different conditions. Conventional Doppler interferometry was assumed as an explanation to the phenomenon and the spectral effects on the laser light output were not studied. Numerous other theoretical models devised to explain the self-mixing effect were based on conventional interferometry even up until recent years.

2.1.2 Self-Mixing Interference in Laser Diode Sensors

In 1976, Mitsuhashi [29] *et al.* proposed a novel scheme based on the self-mixing effect in which a semiconductor laser diode is used not only as a light source, but also as a detector, by monitoring the laser diode junction voltage variation caused by the external feedback. A few years later, Dandridge *et al.* reported a simple laser diode sensor for acoustic sensing [30]. The intensity of the laser light output was shown to vary periodically as a function of the displacement of an external reflective membrane. This principle was used as an acoustic pickup for membrane vibrations. These experiments demonstrated the potential for low-cost, compact, and high accuracy sensors by using laser diodes.

2.1.3 Velocimetry

In 1986, Shinohara *et al.* [42] presented a small laser Doppler velocimeter making use of the self-mixing effect in a semiconductor laser diode. By aiming the laser diode at a rotating disc serving as a particle scatterer, they were able to measure the rotational velocity of the disc using the power fluctuation signal detected by the internal photodiode of the semiconductor laser diode.

They also observed the interference signal in the variation of the terminal driving voltage of the laser diode. Based on this work, Shimizu [24] later observed the power fluctuation waveform in more detail. It was determined that the ramp-shaped signal was asymetric with respect to the direction of the moving target. This rather unique phenomenon was proposed as a directional discriminator for the velocimeter. The explanation given was based on the direction-dependent phase reversal of the second harmonic component of the detected Doppler signal. A later paper by Shinohara *et al.* [43] described the construction of a compact and versatile laser-diode based Doppler velocimeter with directional discrimination in which the asymetry property of the self-mixing Doppler signal was used. They were able to measure velocities with directional discrimination in the range of 23 mm/s to 83 km/h.

Jentink *et al.* [26] described in 1988 their Doppler velocimeter based on the self-mixing effect in a laser diode. Their explanation of the intensity modulation in the laser light due to optical feedback was again based on the conventional interference between the the light inside and the light reentering the laser cavity. This model was soon challenged by de Groot *et al.* [25], who developed a model based on the mode structure of a three-mirror Fabry-Perot cavity. In this model, the intensity modulation of the laser diode in the presence of optical feedback was explained to be due to the change of the carrier density inside the laser cavity.

2.1.4 FM Ranging

G. Beheim and K. Fritsch [31] introduced in 1986 a technique based on the self-mixing effect, in which a frequency-modulated laser diode was used to perform unambiguous range measurements over distances larger than the wavelength of the laser light source. Using the same technique, velocity measurements were also performed. By linearly ramping the emission frequency of the laser light with the help of a triangular modulation signal, conventional constructive and destructive interference were conjectured to give rise to power fluctuations as external cavity modes were swept. The derivative of the power fluctuation signal measured through the laser diode's internal monitor photodiode was used to in order to obtain target range and velocity information. This was accomplished by counting peaks in the derivative signal indicative of external cavity mode hops. They successfully measured target ranges of up to 1.5 m with subcentimeter accuracy. The best accuracy figure was obtained for ranges smaller than 40 cm with a 2.7 mm standard deviation error measured with respect to a linear fit curve. A few years later, Shinohara *et al.* [32] reported a range finder system using a similar

principle of determining the resonant mode spacing of an external cavity with a frequency modulated laser diode. They presented improvements on reducing the uncertainty and noise attributed to estimating the mode spacing. They obtained accuracies of $\pm 0.15\%$ over a range of $0.2 - 1$ m. Again, they relied on conventional interferometry to explain the power fluctuation phenomenon.

2.2 Spectral and Gain Effects in Self-Mixing Interference

Through parallel research motivated by more common commercial applications of laser diodes, other researchers have studied the effects of optical feedback on laser diodes. In fiber-optic communications, it was observed that reflections at a fiber facet in a diode-to-fiber optical circuit degrades the modulation response characteristics and increases intensity noise [34] [35] [36]. This situation is similar to that encountered in CD players where the laser light is reflected off the CD surface. It was discovered that optical feedback effects profoundly influence the spectral properties of the laser along with the threshold gain [37] [23] [40] [38] [39]. Lang and Kobayashi [37] introduced an approach by which the compound cavity model has been used to interpret the observed self-mixing effect phenomena when the distance of an external reflector is smaller than the coherence length of the solitary laser. The well-known ramp-shaped power modulation signal has been successfully modeled through their equations. The frequency output spectrum of the laser diode was also demonstrated to shift periodically with respect to the relative phase of the feedback light.

K. Petermann [49] described the self-mixing interference as being the consequence of the optical spectrum and threshold gain modulation in the laser source. The theory based on a three-mirror Fabry-Perot cavity successfully explained the asymmetry of the power fluctuation signal with the direction of motion of the target as observed experimentally. The ramp-shaped power modulation signal was shown to be dependent on the intensity of the reflected light into the optical cavity. The more intense the optical feedback, the more pronounced the ramp becomes. If a large enough optical feedback is present, the optical coupling gives rise to multiple modes of oscillation in the laser output. For very weak feedback, the power modulation signal approaches the shape of a sine wave as observed in conventional interferometry. The spectral linewidth was also shown to be dependent upon the phase of the feedback light. This linewidth in turn affects the coherence

length of the laser, a classical bound on the maximum range beyond which light interference is no longer possible. Wang *et al.* [40] later applied the theory to optical sensing applications. Their results were very similar to those of Petermann. One important additional conclusion was that since the coherence length of the laser is itself affected by the relative phase shift of the laser light, no simple method exists by which to predict the actual maximum range beyond which self-interference will no longer occur. As corroborating evidence, they cited the paper by Lenstra *et al.* [41] where the coherence length of a single-mode laser diode was reduced from several meters to a few millimeters with optical feedback. This drastic modification of the laser diode's output spectrum was termed "coherence collapse". Similarly, reports of coherence length increase have been made whereby the coherence length of a laser diode coupled to an optical fiber was increased to a theoretical length of 3×10^5 *km* [44]. Other references of the spectral effects due to optical feedback include [45] [47] [46].

In 1992, Koelink *et al.* [33] described a Doppler velocimeter used to perform *in vivo* blood flow measurements. Their velocimeter was composed of a laser diode coupled to a single glass fiber inserted into blood vessels to measure blood flow. In a parallel paper, they introduced a theory [50] for their velocimeter based on the work of Petermann [49] and Acket *et al.* [38]. They extended the existing theory in order to establish a relationship between the output power fluctuations and the threshold gain fluctuations of the laser diode induced by optical feedback.

2.3 Current State of Research

At this point, a reasonably clear, though not fully complete theory is in place to explain the laser spectral properties and threshold gain modulation induced by external feedback. Unlike conventional interferometry, the use of the laser cavity as a mixing medium results in fundamental variations of the laser source properties, such as frequency, linewidth, and threshold gain. More work however is still needed to fully model the interaction effects of the spectral linewidth variation, affecting the coherence length of the laser and the observed self-mixing interference given various levels and conditions of feedback. A theoretical model is also still not fully developed to model the experimental curves obtained in the FM ranging and velocimetry system as described in [31] and [32]. This last item is the focus of the current work.

Chapter 3

Theoretical Analysis of the Self-Mixing Effect

In order to model the self-mixing effect and gain sufficient practical insight into this phenomenon, a theoretical framework is presented based on the work of several different researchers. The development starts by introducing the Fabry-Perot cavity and a few other necessary notions. The strategy for solving laser equations is first presented, and is then applied to modelling the self-mixing effect. Following this key development, an extension of the theory will be introduced in order to suit our current needs, and accurately model the experimental curves obtained with FM ranging using the self-mixing effect.

This process will demonstrate the usability of the self-mixing effect in performing single degree of freedom (DOF) range measurements. Ultimately, 3D range images will be acquired through the combination of the 1 DOF ranging system and a laser beam steering unit. This will allow the range sampling of scanned surfaces. With this in mind, let us proceed with the investigation of the self-mixing effect as part of a 1 DOF ranging unit.

3.1 Basic Notions

3.1.1 Laser Fundamentals

A laser is effectively composed of two essential elements: an optical cavity and a gain medium. The optical cavity allows for optical energy buildup and storage around specific narrowband frequencies corresponding to the cavity's

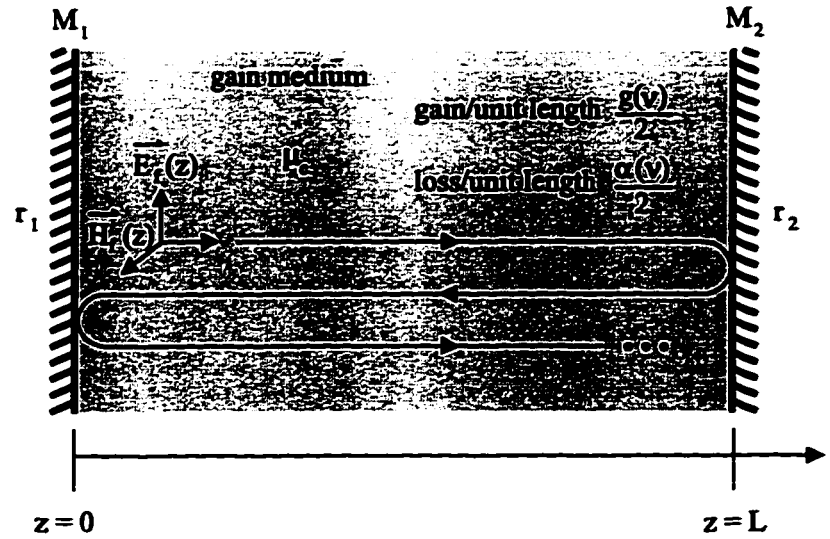

Figure 3.1: Fabry-Perot cavity with gain medium

resonant modes[1] of oscillation. The gain medium provides amplification of the light confined in the optical cavity through stimulated emission. The amplification (gain) profile is frequency dependent, such that the combination of the gain profile and cavity properties ultimately determine the lasing frequency of the laser. This frequency corresponds to the the dominant mode(s) of oscillation. Figure 3.1 illustrates an optical cavity, also known as a Fabry-Perot cavity. The cavity is composed of two parallel mirrors (M_1, M_2) placed at each extremity of the gain medium of length L and effective refraction index μ_e ($= 3.6$ for GaAs).

Consider a uniform plane wave propagating through the cavity. The wave is composed of two mutually perpendicular modes of oscillation corresponding to the transverse electrically (TE) polarized and transverse magnetically (TM) polarized modes. These two components are in turn perpendicular to the direction of propagation of the wave. Laser diodes usually emit the TE polarized mode only, since the facet reflectivities are higher for TE modes than for TM modes [49] yielding a lower threshold gain for the TE polarization. Therefore, the following derivations will concentrate on the electric field component.

[1] A cavity mode is defined [48] as a field distribution that reproduces itself in relative shape and in relative phase after a round trip through the system.

The electric field $\vec{E}_{f0}$ at the immediate right of mirror M_1 travels through the medium which possesses a gain per unit length parameter defined as $\frac{g(\nu)}{2}$ with respect to the electric field. Notice the dependence of the gain parameter to the frequency ν of oscillation of the electric field. Similarly, a loss per unit length $\frac{\alpha(\nu)}{2}$ with respect to the electric field also exists in the gain medium. Because of the exponential nature of the amplification/loss mechanisms in the gain medium, the overall gain seen by the electric field traveling from the immediate right of M_1 to a position z, to the left of M_2 is modeled as an exponential relationship [49] to these above quantities given by Equation 3.1

$$G(z) = e^{(\frac{g(\nu)}{2} - \frac{\alpha(\nu)}{2})z} \tag{3.1}$$

Here, we assume that $\frac{g(\nu)}{2}$ and $\frac{\alpha(\nu)}{2}$ are uniform over all the gain medium. After having traveled through the gain medium by a distance z, $\vec{E}_f(z)$, the electric field inside the cavity, is now:

$$\vec{E}_f(z) = \vec{E}_{f0}G(z)e^{-j\beta z} = \vec{E}_{f0}e^{(\frac{g(\nu)}{2} - \frac{\alpha(\nu)}{2})z - j\beta z} \qquad z \in [0^+, L^-] \tag{3.2}$$

Where $\beta = \frac{2\pi\nu\mu_e}{c}$ is the phase constant in $(\frac{\text{rads}}{\text{unit length}})$ of the propagating wave as part of the $e^{-j\beta z}$ term accounting for the phase shift over a distance z. The term μ_e is the effective refraction index of the gain medium (3.6 for GaAs). We shall now consider the expression of $\vec{E}_f$ for a round trip through the optical cavity. An incident electric field to the surface of a mirror is reflected according to Equation 3.3

$$\vec{E}_{reflected} = (\vec{E}_{incident})r \tag{3.3}$$

where r is the complex reflection coefficient of the mirror with respect to the electric field. This quantity is also related to the mirror's power reflection coefficient R as $R = |r|^2$. For standard mirrors, the quantity r may be assumed to be real and valued between 0 and 1 (0.52 typically for semiconductor laser diodes). After a round trip through the cavity, the electric field $\vec{E}_{frt}$ is given by:

$$\begin{aligned}
\vec{E}_{frt} &= \underbrace{\vec{E}_{f0}}_{\substack{\text{initial}\\ \text{field}\\ \text{at } 0^+}} \underbrace{e^{(\frac{g(\nu)}{2} - \frac{\alpha(\nu)}{2})L - j\beta L}}_{\substack{\text{pass through}\\ \text{gain medium}}} \underbrace{r_2}_{\substack{\text{reflec}\\ \text{tion}\\ M_2}} \underbrace{e^{(\frac{g(\nu)}{2} - \frac{\alpha(\nu)}{2})L - j\beta L}}_{\substack{\text{back through}\\ \text{gain medium}}} \underbrace{r_1}_{\substack{\text{reflec}\\ \text{tion}\\ M_1}} \\
&= \vec{E}_{f0}r_1r_2e^{(g(\nu)-\alpha(\nu))L}e^{-j2\beta L}
\end{aligned} \tag{3.4}$$

Intuitively, it is easy to observe that if $|\vec{E}_{frt}| < |\vec{E}_{f0}|$ then the round trip loss has exceeded the round trip gain and thus the electric field will decay to zero and no lasing action will take place. A fundamental requirement for lasing to occur is:

Net Round Trip Gain ≥ 1

Similarly, a requirement exists for the phase of the electric field which has to travel through an integral number of wavelengths yielding the second fundamental requirement:

Net Round Trip Phase Shift $= 2\pi m \qquad m = 0, 1, \ldots$

These two conditions are automatically imposed by setting $\vec{E}_{frt} = \vec{E}_{f0}$ in Equation 3.4 which then yields the threshold condition for the onset of lasing activity:

$$1 = r_1 r_2 e^{(g_{th}(\nu) - \alpha(\nu))L} e^{-j2\beta L} \tag{3.5}$$

We may solve the real and imaginary parts separately to obtain:

$$1 = r_1 r_2 e^{(g_{th}(\nu) - \alpha(\nu))L} \tag{3.6}$$

$$e^{j2\pi m} = e^{-j2\beta L} \qquad m = 0, 1, \ldots \tag{3.7}$$

Finally, we derive from Equations 3.6 and 3.7:

$$g_{th}(\nu) = \frac{1}{L} \ln \left[\frac{1}{r_1 r_2} \right] + \alpha(\nu) \tag{3.8}$$

$$\beta L = m\pi \qquad m = 0, 1, \ldots \tag{3.9}$$

where $g_{th}(\nu)$ represents the threshold gain, or the minimal gain per unit length required within the gain medium for lasing action to emerge. This gain is related to the pumping process used to generate the population inversion inside the laser gain medium [49]. The second constraint restricts the possible values of β which is related to the optical frequency ν. Equation 3.9 therefore yields the possible emission frequencies of the laser resonator. If we consider the effective refraction index μ_e inside the laser cavity and assume

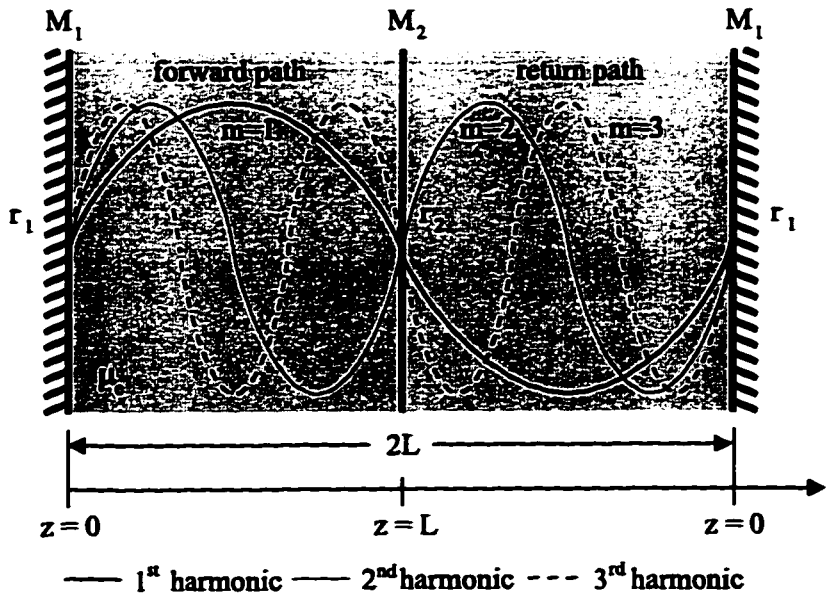

Figure 3.2: Resonant cavity modes in *unfolded* round trip path

negligible dispersion of the medium[2], then the possible emission frequencies ν are given as:

$$\nu = m\left(\frac{c}{2L\mu_e}\right) \qquad m = 1, 2, \ldots \tag{3.10}$$

where c represents the speed of light. The term $\frac{2L\mu_e}{c}$ represents the period of the fundamental resonant mode of the cavity ($m = 1$) as illustrated in Figure 3.2 also showing the $2^{nd}(m = 2)$ and $3^{rd}(m = 3)$ harmonics. The lasing frequency of a laser is therefore selected in part by the cavity length.

The energy level spectral distribution[3], a physical property of the gain medium inside the cavity, will dictate the selection of a dominant mode of oscillation among all the possible cavity resonant modes. In the end, for a single mode laser, the oscillation mode with the highest overall gain-to-loss ratio will be amplified and will monopolize the inverted population resources

[2]In some materials, waves of different frequencies travel at different velocities. It occurs when β is no longer a linear function of the frequency ν. This gives rise to signal dispersion. For signals of small bandwidth, an approximation is usually performed by taking a Taylor series approximation of the $\beta - \nu$ relation. This results in the introduction of an effective group refractive index $\overline{\mu_e}$[49].

[3]The probability of finding a photon at a given energy level (or frequency since $E = h\nu$).

of the gain medium for self-amplification through stimulated emission. This will effectively reduce the possibility of amplification of neighboring modes of oscillation. As the inverted population becomes depleted, the external pumping process of the laser re-injects additional carriers. An equilibrium is achieved when the depletion rate of the inverted population equals its rate of replenishment through the pumping process. At that time, a single mode of oscillation exists with considerably larger amplitude than any of its neighboring modes.

The final relevant basic concept describes the useful output of the laser exiting the laser cavity. This occurs at both extremities of the cavity when a portion of the incident electric field is transmitted through the mirrors as described by Equation 3.11

$$|\vec{E}_{transmitted}|^2 = T|\vec{E}_{incident}|^2$$

$$\text{where} \quad T = (1-R) = 1-|r|^2 \tag{3.11}$$

Here, T represents the power transmission coefficient for a lossless mirror, and r is the complex reflection coefficient of the mirror with respect to the electric field, as seen earlier.

3.1.2 Semiconductor Laser Diodes

Of all the different types of lasers, laser diodes prove to be the most versatile and widespread. This is in part due to their low cost, compactness and direct compatibility with the electrical world. A laser diode is simply a *pn* semiconductor junction combined with an optical resonator. The *pn* junction forms a diode which is operated in the forward biased regime. The injected carriers resulting from the application of a drive current to the laser diode recombine at the *pn* junction giving rise to the emission of photons. If the carrier density within the *pn* junction exceeds a threshold value, the light generated will be amplified and will finally yield the laser emission.

Since the required carrier density for laser operation is quite high, it is necessary to confine the recombining carriers in as small a volume as possible. This can be achieved very effectively through the use of a double heterojunction. The active layer (region in which the carriers combine) is sandwiched between heterolayers having a larger band-gap as may be inferred from the energy band diagram illustrated in Figure 3.3. The *pn* junction occurs at the active layer, exhibiting a lower band-gap. Due to the double-heterostructure, the recombination of carriers is possible only in this

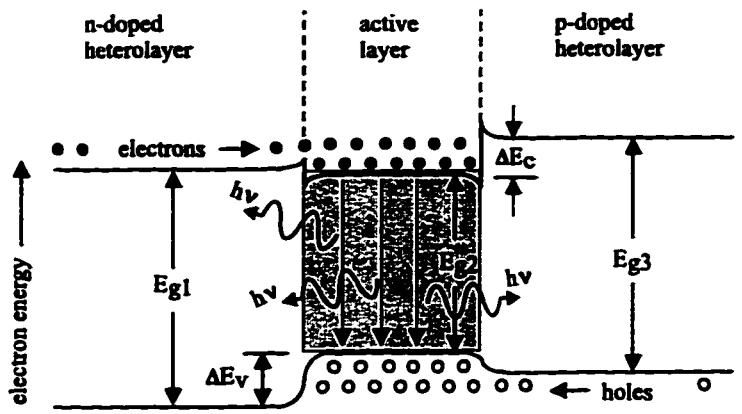

Figure 3.3: Energy band diagram for a double heterostructure laser diode

active layer. The energy band diagram is shown when the diode is biased in the forward direction. E_{g1}, E_{g2} and E_{g3} represent the energy gaps of the n-doped heterolayer, the active layer and the p-doped heterolayer, respectively. When current is applied, electrons form the n-doped heterolayer and holes from the p-doped heterolayer are injected into the active layer. At the junction of the heterolayers, the energy step ΔE_c prevents electrons from passing into the p-doped heterolayer and ΔE_v prevents holes from passing into the n-doped heterolayer. The injected carriers may therefore only recombine in the active layer since there, the electrons in the conduction band find holes in the valence band with which they recombine. As a result of the recombination of electrons and holes in the active layer, photons are emitted with frequency $\nu = \frac{E_{g2}}{h}$, where h is Planck's constant. At each end of the active layer (parallel to the page), an optical cavity is built by cleaving the GaAs semiconductor crystal. This produces two parallel facets, or mirrors allowing for resonant mode selection and energy storage. One of the facet is exposed and becomes the output aperture of the laser diode.

The optical power output versus drive current (P-I) curve of a typical laser diode is illustrated in Figure 3.4. The curve exhibits a "knee" below which minimal light output power is observed, and the laser diode behaves as a standard light emitting diode (LED). For current values beyond the knee, a quasi-linear dependence exists between the input current and the laser light output power. The current value at the knee of the curve corresponds to the threshold current of the laser diode I_{th} which is related to the minimum required gain g_{th} to sustain lasing in the gain medium. The

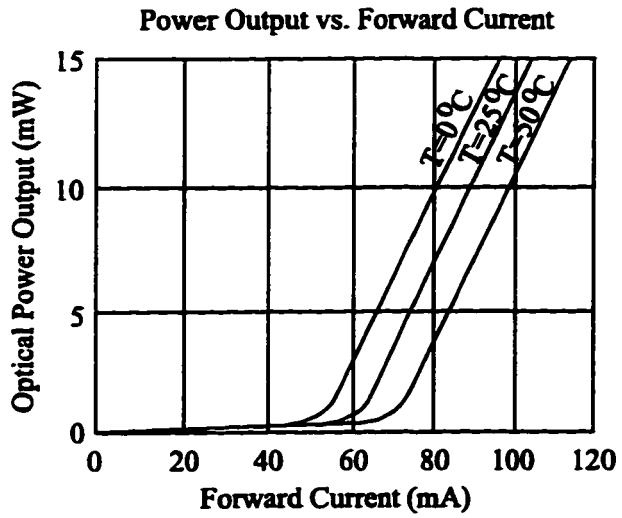

Figure 3.4: Optical output power vs. drive current for a semiconductor laser diode

P-I relationship is also temperature dependent as is shown in Figure 3.4. For a fixed operating current, a sudden decrease in temperature results in an increase in light power output. For a large enough temperature swing, this may result in physical damage to the laser diode. That is in part why a power monitor photodiode is usually built into the laser diode package, directly behind the rear facet of the optical cavity. The intensity of the output light is monitored through the photocurrent induced in the photodiode by the impinging laser light sampled from the cavity. This signal is then fed back to a current regulation system that increases/decreases the drive current automatically in the case of a temperature increase/decrease to ensure a constant light power output.

A problem arises when emitted laser light re-enters the laser cavity after being reflected by an external target. Emission frequency, output power and linewidth variations have been found to result from backscattered laser light [49]. This is usually a nuisance, for example in CD players, where the light reflected from the disc surface is reflected back to the laser cavity and modifies the laser light properties and results in increased noise. Manufacturers sometimes go to great lengths in an attempt to reduce the intensity of the light returning to the laser cavity. Anti-reflection coatings are often placed on lenses and other potentially reflective surfaces in front of the laser

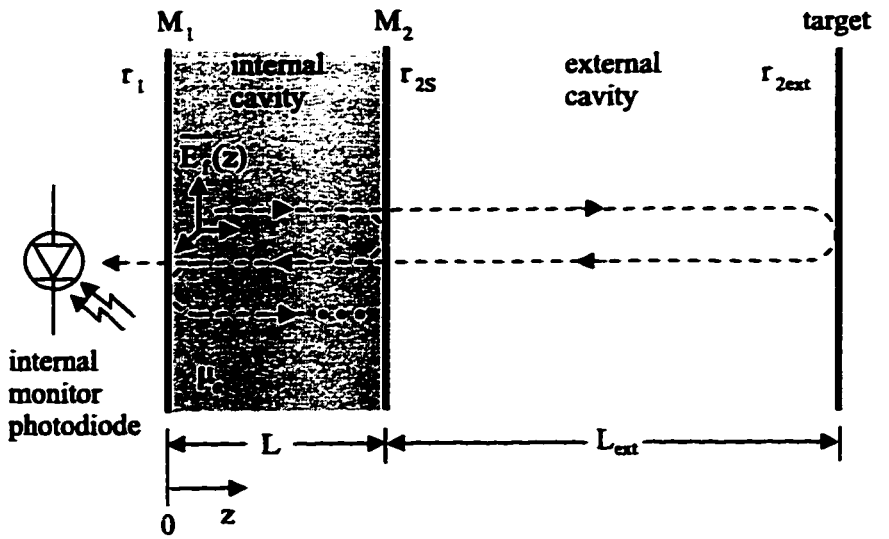

Figure 3.5: Three mirror optical cavity model

diodes. We however take advantage of this effect for ranging and velocimetry applications as will be demonstrated shortly. Although the self-mixing effect is applicable to various types of lasers, in this work we shall focus on single-mode semiconductor laser diodes.

3.2 The Self-Mixing Effect

The self-mixing effect describes a situation whereby emitted laser light is reflected off a target and is allowed to re-enter the laser diode cavity. Unlike conventional interferometry, this results in both emission frequency and output power fluctuations of the emitted laser light [49].

A theoretical model of this phenomenon will now be presented partly based on the work of Petermann [49] and Koelink et al. [50]. This will provide some practical insight into the self-mixing phenomenon. Following this key derivation, an extension of the theory will be introduced in order to suit our current needs, and accurately model the experimental curves obtained with FM ranging using the self-mixing effect used in our setup.

Figure 3.5 represents the self-mixing effect scenario. Facets r_1 and r_{2s} represent the semiconductor's optical cavity with r_{2s} being the output facet and r_{2ext} being an external reflector. Also illustrated is the monitor photo-

diode usually integrated inside the laser diode package for monitoring and regulating the output light intensity, which is very sensitive to temperature fluctuations. In our case, the temperature of the laser diode shall be regulated externally and the internal photodiode shall instead be used to monitor directly the laser light power fluctuations induced by the backscattered light from the distant target.

First, from Figure 3.5 we replace the mirror at $z = L$ whose reflection coefficient is currently r_{2s} by an equivalent mirror in the same position which combines r_{2s} and r_{2ext} yielding the new *complex* reflection coefficient $r_2(\nu)$ given by:

$$r_2(\nu) = r_{2s} + (1 - |r_{2s}|^2) r_{2ext} e^{-j2\pi\nu\tau_{ext}} \tag{3.12}$$

where ν is the optical frequency and $\tau_{ext} = \frac{2L_{ext}}{c}$ is defined as the round trip delay time of the traveling wave in the external cavity. The first term of the equation accounts for direct reflection off r_{2s}, and the second term accounts for the portion of the electric field passing through the facet r_{2s}, reflected off r_{2ext} and back. Note that we will neglect multiple reflections between r_{2s} and r_{2ext} as it is assumed that $|r_{2ext}| \ll |r_{2s}|$. The phase shift term accounts for the round trip phase shifts of the electric field in the external cavity. Since $r_2(\nu)$ is a complex number, we may write it as:

$$r_2(\nu) = |r_2(\nu)| e^{-j\phi_r} \tag{3.13}$$

Here, ϕ_r represents the electrical phase shift for a round trip through the external cavity. The problem has now become reduced to a two facet Fabry-Perot cavity with complex reflection coefficient $r_2(\nu)$. As in Equation 3.5, we write the necessary threshold equation for lasing to occur:

$$\vec{E}_{frt} = \vec{E}_{f0} r_1 |r_2(\nu)| e^{(g_{th}(\nu) - \alpha(\nu))L} e^{-j(2\beta L + \phi_r)} \tag{3.14}$$

We impose $\vec{E}_{frt} = \vec{E}_{f0}$ to get:

$$1 = r_1 |r_2(\nu)| e^{(g_{th}(\nu) - \alpha(\nu))L} e^{-j(2\beta L + \phi_r)} \tag{3.15}$$

Solving the real and imaginary parts separately yields:

$$1 = r_1 |r_2(\nu)| e^{(g_{th}(\nu) - \alpha(\nu))L} \tag{3.16}$$

$$2\beta L + \phi_r = 2\pi m \qquad m = 0, 1, \ldots \tag{3.17}$$

Since $\beta = \frac{2\pi\nu\mu_e}{c}$, the phase condition 3.17 may be re-written:

$$\frac{4\pi\nu\mu_e L}{c} + \phi_r = 2\pi m \qquad m = 0, 1, \ldots \tag{3.18}$$

Equations 3.16 and 3.18 constitute the basic requirements for lasing to occur for the three mirror cavity. Without loss of generality, we may consider r_{2s}, r_{2ext} to be real, and also $|r_{2ext}| \ll |r_{2s}|$, so as to derive expressions for $|r_2(\nu)|$ and ϕ_r. By expanding Equation 3.12 and simplifying negligible terms, we get:

$$|r_2(\nu)| = r_{2s}[1 + \kappa_{ext}\cos(2\pi\nu\tau_{ext})] \tag{3.19}$$

where

$$\kappa_{ext} = \frac{r_{2ext}}{r_{2s}}(1 - |r_{2s}|^2) \tag{3.20}$$

κ_{ext} represents the coupling coefficient to the external cavity. Similarly, the phase ϕ_r or $r_2(\nu)$ may be obtained from Equation 3.12 by expanding and simplifying negligible terms to get (for $\kappa_{ext} \ll 1$):

$$\phi_r = \kappa_{ext}\sin(2\pi\nu\tau_{ext}) \tag{3.21}$$

In the case of no feedback ($\phi_r = 0$), Equation 3.18 yields ν_{th}, the emission frequency of the laser without feedback. Due to feedback however, both the emission frequency ν and the threshold gain $g_{th}(\nu)$ may change. Using the threshold gain and phase conditions for lasing to occur given by Equations 3.16 and 3.18, we derive [49] the following two key equations describing the fluctuation of the the threshold gain (Equation 3.22) and of the emission frequency (Equation 3.23) under feedback for $\kappa_{ext} \ll 1$:

$$\Delta g = (g_c - g_{th}) = -\frac{\kappa_{ext}}{L}\cos(2\pi\nu\tau_{ext}) \tag{3.22}$$

where g_c is the threshold gain as a result of external feedback, and g_{th}, that without feedback. Δg therefore describes the variation of the threshold gain, or minimal gain per unit length required in the gain medium to sustain lasing activity. Figure 3.6 depicts the threshold gain fluctuation versus the external phase $\phi_{ext} = 2\pi\nu\tau_{ext}$. ϕ_{ext} may be varied by either changing the emission frequency ν or the target distance L_{ext} (through the round trip delay $\tau_{ext} = \frac{2L_{ext}}{c}$). We observe from Equation 3.22 that the maximum variation of the threshold gain Δg_{max} is given by $\pm\frac{\kappa_{ext}}{L}$. Also, the maximum *reduction* of the threshold gain occurs for $\phi_{ext} = 2\pi m \quad m = 0, 1, \ldots$ or in-phase feedback. This occurs when the target distance is an integer multiple of $\frac{\lambda}{2}$, where λ is the wavelength associated with the emission frequency ν. Maximum increase in Δg occurs at $\frac{\lambda}{4} + m\frac{\lambda}{2}$, $m = 0, 1, \ldots$

Now, before we may apply Equation 3.22, we first have to determine the actual lasing frequency ν which itself is modified by external feedback. This

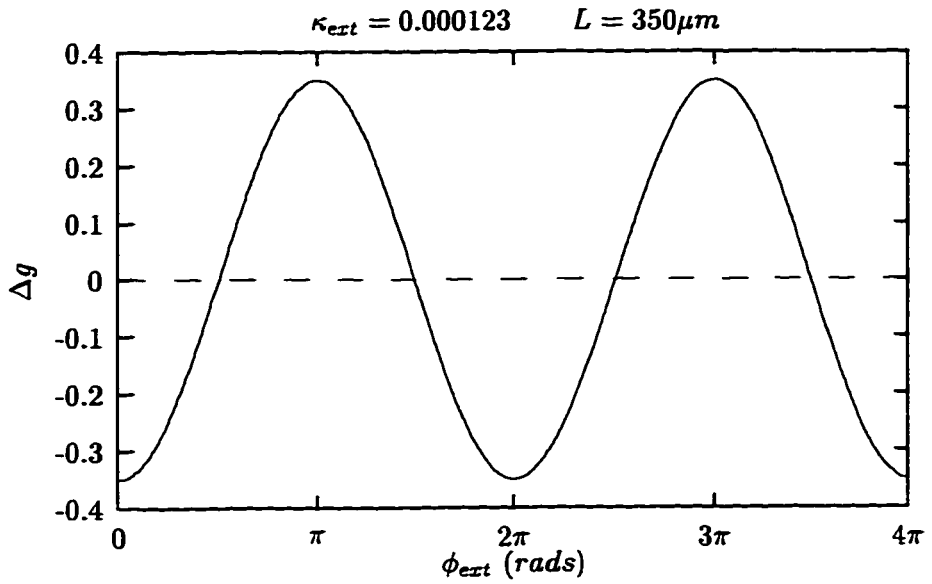

Figure 3.6: Threshold gain variation with optical feedback

is given by the second key equation describing the relationship between the lasing frequency ν and the excess phase $\Delta\phi_L$ of the cavity:

$$\Delta\phi_L = 2\pi\tau_{ext}(\nu - \nu_{th}) + C\sin(2\pi\nu\tau_{ext} + \arctan\alpha)$$

$$\text{where} \quad C = \frac{\tau_{ext}}{\tau_L}\kappa_{ext}\sqrt{(1+\alpha^2)} \tag{3.23}$$

The constant α, typically between 3 and 7 [49], is the laser linewidth enhancement factor. ν_{th} is the natural lasing frequency of the laser without feedback. $\tau_L = \frac{2\overline{\mu_e}L}{c}$ is the internal cavity round trip delay. $\overline{\mu_e}$ is the effective group refraction index accounting for the medium dispersion, and is typically between 3.5 and 5 [49]. $\tau_{ext} = \frac{2L_{ext}}{c}$ is the external cavity round trip delay. $\Delta\phi_L$ corresponds to a change in the round trip phase as compared to $2\pi m$, $m = 0, 1, \ldots$ for the compound cavity. Even in a compound cavity, we know that the round trip phase shift has to be 0 or an integral number of 2π for the lasing phase condition to be satisfied.

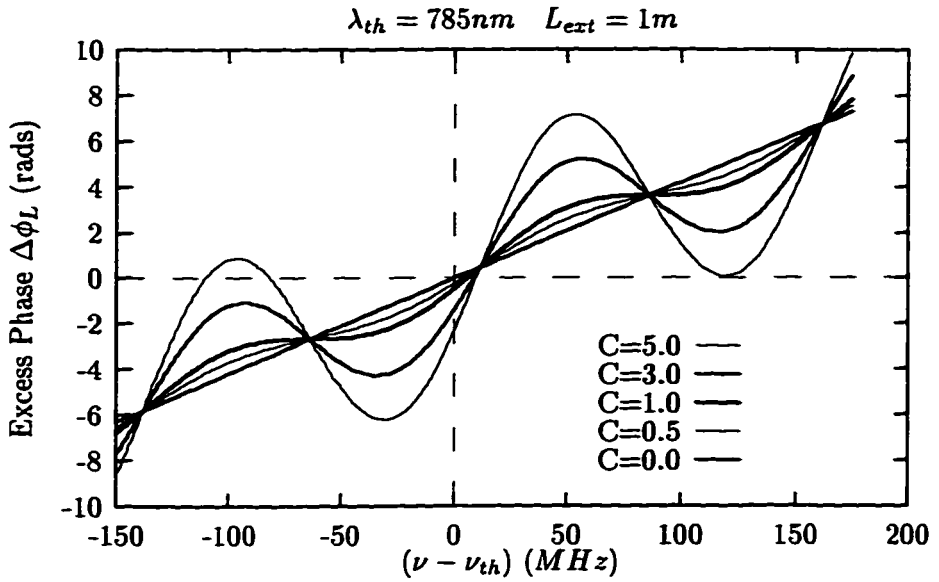

Figure 3.7: Excess phase variation vs. emission frequency

By setting the excess phase $\Delta\phi_L$ to 0, Equation 3.23 may be solved numerically for ν. Figure 3.7 shows a plot of the excess phase $\Delta\phi_L$ versus $(\nu - \nu_{th})$. When solved numerically for $\Delta\phi = 0$, it yields the emission frequency of the laser with feedback. This is seen by the abscissa intersects of the curve corresponding to the roots of the equation. Several curves are shown with different values of C, the coupling or feedback coefficient describing the intensity of the laser light coupling between the external reflector and the laser diode cavity. The larger the value of C, the more light is backscattered in the cavity. As seen in Figure 3.7, for $C < 1$ a single solution of the lasing frequency ν exists as the relationship is monotonic. For larger values of C, multiple solutions (roots) may exist. This indicates the presence of multiple modes of oscillation. The assumption that $C < 1$ will always be implied from now on in order to obtain a single mode operation. The other interesting aspect of the curves is their increasing asymmetry with increasing values of C.

We now have a method of determining the lasing frequency of the laser diode with external feedback by setting $\Delta\phi_L = 0$ in Equation 3.23 and solving numerically for ν, the lasing frequency in presence of feedback. By doing this repeatedly for varying target displacement, Figure 3.8 was ob-

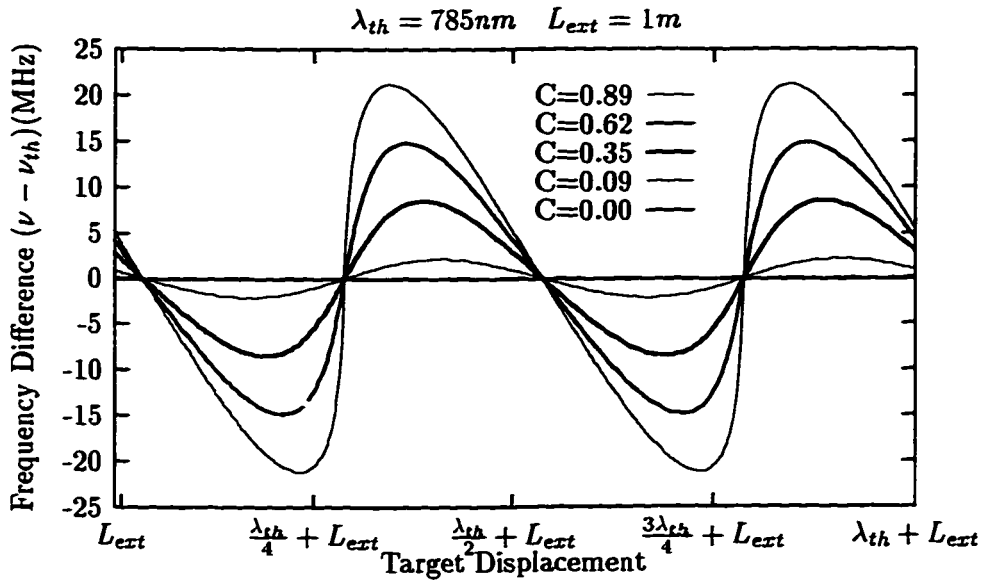

Figure 3.8: Frequency shift vs. target displacement

tained showing the variation of the lasing frequency induced by feedback for different target positions. Here, the theoretical target was placed at a nominal position L_{ext} in front of the laser diode and displaced by a distance corresponding to a number of wavelengths λ_{th} associated with the nominal emission frequency without feedback ν_{th}. The curves are shown for different values of C, the coupling coefficient. We observe that the curves show an abrupt hop in the emission frequency at every $\frac{\lambda_{th}}{2}$ of the target displacement corresponding to a full 2π phase shift of the round trip. The maximum frequency deviation is given by:

$$\Delta\nu_{max} = (\nu - \nu_{th})_{max} = \frac{\kappa_{ext}\sqrt{1+\alpha^2}}{2\pi\tau_L} \tag{3.24}$$

which is related to the reflection coefficient κ_{ext}. The abrupt shift in the frequency may be explained by Figure 3.9. Part (A) represents the initial spectral output when a target is placed at distance L_{ext} in front of the laser diode. As the target is moved closer to the laser diode, the possible resonant cavity modes are shifted to the right due to the reduction of the compound cavity length. When the target is approached by less than half a wavelength, as represented by part (B), a quasi-linear increase of the output frequency

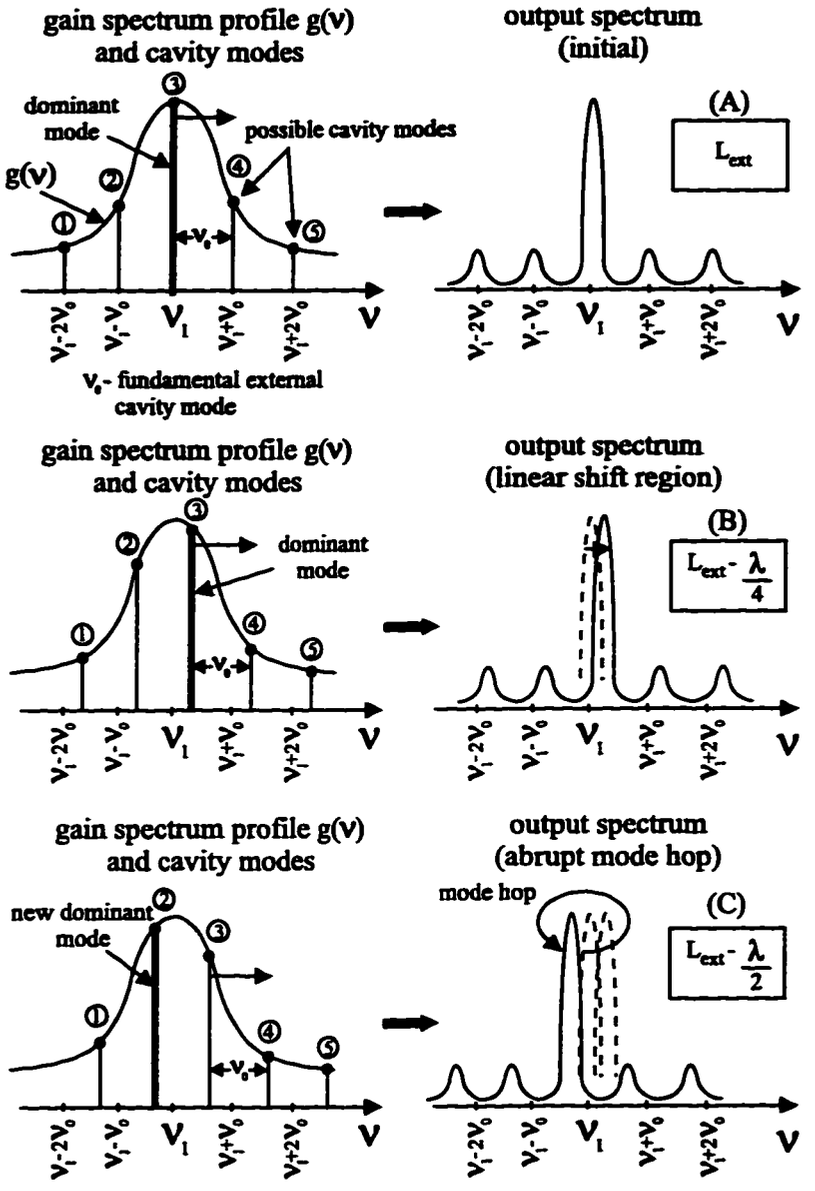

Figure 3.9: Mode hopping phenomenon. As the target distance is *decreased*, the laser frequency *increases* so as to satisfy the phase condition. When increased too far, a neighboring mode abruptly dominates and the cycle repeats.

of the laser is observed. This occurs in order to satisfy the lasing phase condition in the compound cavity. In part (C), the target is moved closer by half a wavelength. An abrupt jump in the laser frequency (mode hop) is observed as a neighboring mode suddenly becomes the dominant mode with respect to the frequency dependent gain spectrum $g(\nu)$ of the gain medium. Keep in mind that the gain spectrum is actually the exponent in an exponential expression (see Equation 3.1), thus the overall gain is very high for a mode who dominates even by a very small amount. Once triggered, self-amplification of a dominant mode monopolizes the inverted population resources as to reduce the gain to the other possible resonant modes. The figures at the right indicate the corresponding light output spectrum outlining the frequency shift due to target displacement.

Now that a method of computing the lasing frequency of the laser diode in the case of external feedback using Equation 3.23 exists, we shall concentrate on deriving a relationship describing the laser power fluctuation as a function of the target displacement, an easily measurable quantity. Since Equation 3.16 relates threshold gain fluctuation of the compound cavity versus the emission frequency, it is possible to relate Δg, the threshold gain fluctuation to ΔP, the laser power fluctuation [50].

By using a linearized dependence of the threshold gain g_{th} as a function of the carrier density n in a semiconductor laser diode, we may write:

$$g_{th} = a(n - n_{th}) \tag{3.25}$$

where a is a constant that depends on the threshold gain-carrier density characteristics. For small variations of the threshold gain with optical feedback ($\frac{|g_c - g_{th}|}{g_{th}} \ll 1$), we can expand both the threshold current I_{th} and the threshold gain g_{th} in the first order of the threshold carrier density n_{th} [49] [38]

$$\Delta I_{th} = (I_c - I_{th}) = eV\left(\frac{1}{T_s}\right)\Delta n_{th} \tag{3.26}$$

$$\Delta g = (g_c - g_{th}) = a\Gamma\Delta n_{th} \tag{3.27}$$

where e is the elementary charge, g_c is the threshold gain with feedback, I_c is the threshold current with feedback, V is the active volume of the laser cavity, T_s is the spontaneous recombination rate, and Γ is the mode confinement factor [49]. Combining Equations 3.26 and 3.27 yields:

$$\Delta g = \frac{T_s a \Gamma}{eV}\Delta I_{th} \tag{3.28}$$

Since the gain curve of a semiconductor laser is almost linear well above the gain threshold, we may write for the optical output P as a function of the current I driving the laser diode:

$$P = \eta(I - I_{th}) \tag{3.29}$$

where η represents the conversion efficiency between optical output power and drive current in (mW/mA). If we combine Equations 3.28 and 3.29, we get:

$$\begin{aligned} P &= \eta(I - [I_{th} + \Delta I_{th}]) \\ P &= \eta(I - [I_{th} + \frac{\Delta geV}{T_s a \Gamma}]) \end{aligned} \tag{3.30}$$

We observe that the output power is seen to *increase* with *decreased* threshold gain. This makes sense intuitively: for a fixed operating current, if we suddenly lower the required threshold gain (similar to the threshold current in a semiconductor diode), the light output power versus current curve of the semiconductor diode (see Figure 3.4) will shift to the left and the output intensity will increase. Substituting Equation 3.22 into 3.30, we get:

$$P = \eta\left(I + \frac{\kappa_{ext} eV}{L T_s a \Gamma} \cos(2\pi\nu\tau_{ext}) - I_{th}\right) \tag{3.31}$$

Where I_{th} is the laser diode threshold current without feedback, I is the operating current, η is the $(\frac{\text{optical power}}{\text{drive current}})$ conversion efficiency. Figure 3.10 shows the power fluctuation for a target placed in front of the laser diode at a nominal distance L_{ext} and displaced by a few wavelengths λ_{th} associated with the laser emission frequency without feedback ν_{th}. The frequency ν of the laser diode due to external feedback is first computed numerically from Equation 3.23 and then placed in Equation 3.31 to yield the output power of the laser diode in the case of feedback. We observe periodic fluctuations when the target is displaced by $\frac{\lambda_{th}}{2}$. The maximum power fluctuation is $\Delta P_{max} = \kappa_{ext}(\frac{eV}{LT_s a\Gamma})$.

In the next section, the extension to the current theory will be presented as to adapt the model to our experimental system configuration.

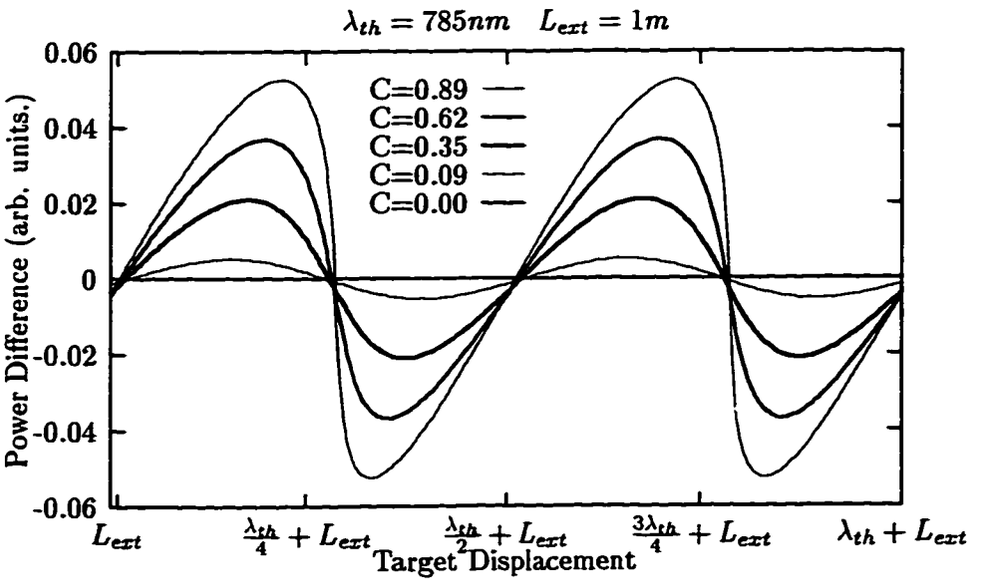

Figure 3.10: Laser diode output power fluctuation vs. target displacement

3.3 The Self-Mixing Effect in Ranging Applications

3.3.1 Ranging of Fixed Targets

We have observed so far in the current theoretical framework that discontinuities or small jumps in the laser's output power appear as a result of feedback when a target is moved through integer values of $\frac{\lambda_{th}}{2}$. This power fluctuation may be conveniently monitored by the internal photodiode. This principle has been employed in various published articles to monitor both displacements [54] [40] [25] and velocity[50] [26] [42] [43] of moving targets. In our case, we are interested in ranging, or measuring the distance between the laser diode and a fixed, noncooperative target in potentially harsh environments. In this case, moving the target or the laser diode is impractical. It is quite possible, however, to set the target position and instead modulate the frequency of the laser. By ramping up the frequency, a similar phase change is induced in the external cavity where a full 2π phase shift occurs at every resonant mode of the external cavity given by $\nu_{\text{resonant}} = m\left(\frac{c}{2L_{ext}}\right) \quad m = 1, 2, \ldots$ We therefore gradually ramp up the

frequency of the output light noting the frequencies where an abrupt power fluctuation occurs. Since, these frequencies correspond to the external resonant cavity modes, a simple difference between any two successive mode frequencies is sufficient to deduce the fundamental mode frequency ν_0 of the cavity (i.e. $m = 1$). To get better accuracy, an average over many successive modes is performed. Then, deducing the distance to the target is simply a matter of realizing that $L_{ext} = \frac{\lambda_0}{2}$ and $\lambda_0 = \frac{c}{\nu_0}$. Thus, the following relationship:

$$L_{ext} = \frac{c}{2\nu_0} \tag{3.32}$$

As mentioned previously, the value of the fundamental mode frequency ν_0 can be determined by taking an average over consecutive resonant mode spacings detected by monitoring power fluctuations as the frequency is ramped up. In practice, however, one cannot keep increasing the frequency indefinitely. A triangular modulation signal is then used to ramp the frequency up and down. It is well-known [40] that the asymmetry or inclined ramp (for large enough values of the reflection coefficient C) in the power variation versus external phase reverses its slope depending on the direction of the moving target, or in this case on the increasing or decreasing frequency ramp. This is evident from Figure 3.10 depending from which direction we traverse the graph when the waveform is asymmetric. This fact will be important for a moving target in order to recover its direction of motion.

3.3.2 Mechanical Analogy of the FM Ranging Principle

At this point, let us establish an intuitive mechanical analogy to the system. Figure 3.11 depicts an equivalent mechanical scenario of the FM ranging problem. Here it is desired to determine the length L of a cavity. The only tools available to determine the cavity length are a string fastened to one end of the cavity wall and to a variable frequency mechanical vibrator located at the other end of the cavity. According to the physics of vibrating strings, when the string is vibrated at certain discrete resonance frequencies, corresponding to the resonant modes of the cavity, a standing wave will be observed. By observing the string, it is therefore possible to determine at which frequencies the standing waves occur. The length of the cavity will be simply given by half the wavelength λ_0 of the fundamental resonant mode f_0 of the cavity as illustrated in the figure. In order to determine the fundamental resonant mode, the simplest method would be to start from a frequency of 0 Hz and gradually increase it until the first, or fundamental resonant mode f_0 is observed. If, let us assume, we did not have the option

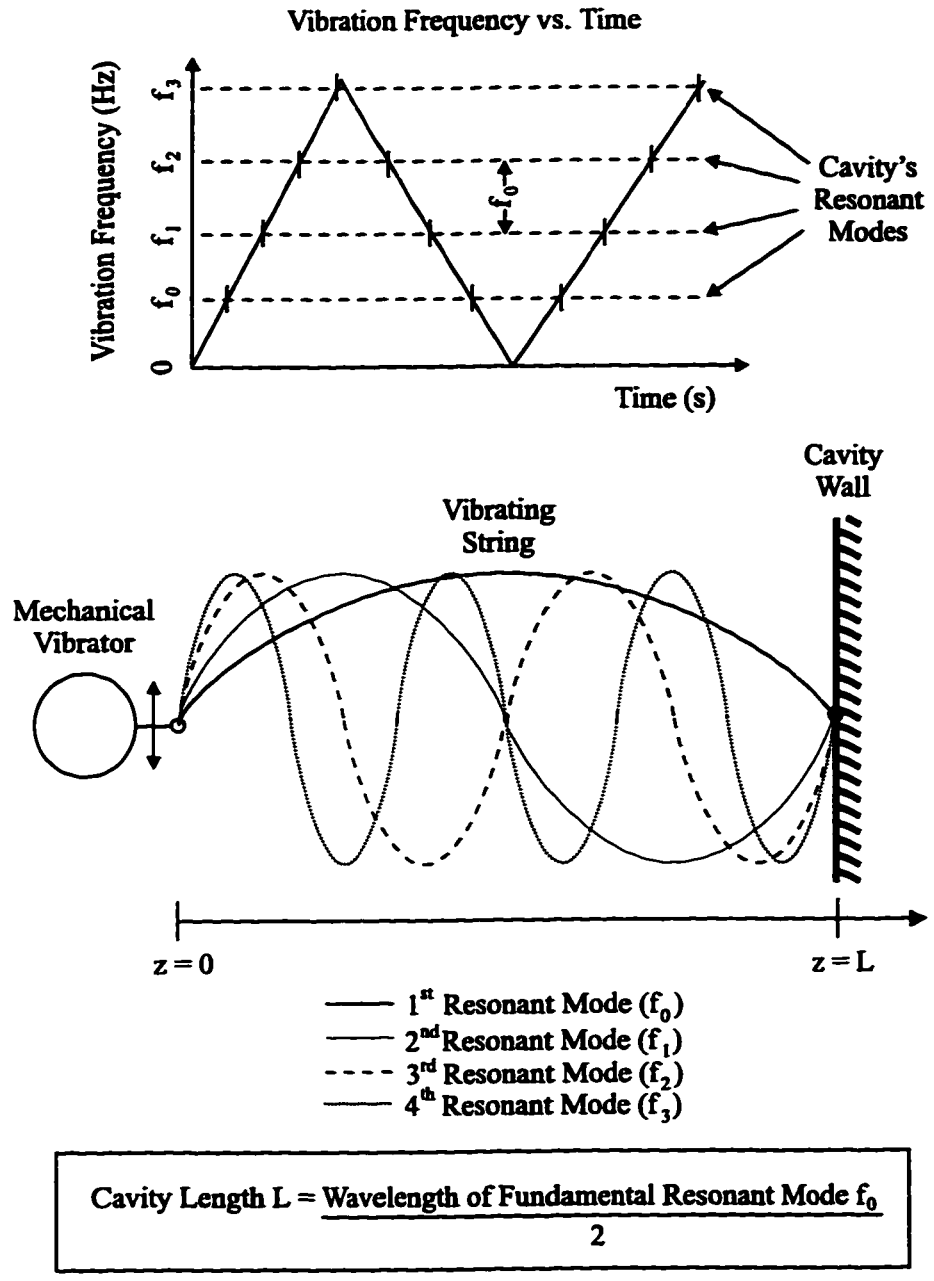

$$\text{Cavity Length } L = \frac{\text{Wavelength of Fundamental Resonant Mode } f_0}{2}$$

Figure 3.11: Mechanical analogy of the ranging principle. The problem is that of determining the length L of a cavity given only a variable frequency generator vibrating a string tied to to the cavity wall.

of starting at 0 Hz, but instead at another arbitrary frequency, than we would have to use another approach. Noting that the resonant modes of the cavity are simply multiples of the fundamental mode f_0, then it follows that the difference between two successive resonant modes is f_0. Therefore, all that is needed to determine f_0 are at least two successive resonant mode frequencies. To get better accuracy, however, it is possible to consider a large number of successive resonant frequencies and deduce an average frequency spacing corresponding to f_0. This mechanical analogy is very similar to the FM laser-based ranging system. An abrupt power fluctuation in the lasing power will serve as a marker indicating that a resonant frequency has been reached similar to the observation of a standing wave in the mechanical system. The frequency of oscillation of the laser light cannot be shifted down to zero, so the second technique of estimating the resonant mode spacing will employed. The frequency of the laser will therefore be swept over an arbitrary frequency range around the nominal lasing frequency of the laser as to observe the resonant cavity modes.

3.3.3 Frequency Modulation of Laser Diodes

Equation 3.31 shows that the optical output power of a laser diode is proportional to the drive current above the threshold. It is also be demonstrated [51] [52] [53] [49] [55] that thermal expansion of the laser diode cavity along with change of the refraction index are responsible for decreasing the lasing frequency ν_{th} of the laser diode as the drive current is increased. This effectively results in frequency modulation (FM) as a function of the drive current. For typical AlGaAs laser diodes, the variation in output frequency is approximately of $-3\frac{GHz}{mA}$ for modulation frequencies below about 1 GHz. This convenient property will be used in order to generate the required frequency sweep used to detect external cavity modes.

3.4 A Theoretical Model for FM Ranging

Beheim and Fritsch [31] were early discoverers of the possibility to use frequency modulated laser diodes to recover the distance to a fixed target through monitoring of laser power fluctuations. They modeled the power fluctuations by using conventional interferometry arguments. Experimental observations proved that the self-mixing effect exhibited peculiarities beyond the answers provided by classical theories. A few years later, Shinohara et al. [32] reported a range finder system using a similar principle of determining the resonant mode spacing of an external cavity with a frequency modu-

lated laser diode. They reported improvements on reducing the uncertainty and noise attributed to estimating the mode spacing. Again, they relied on conventional interferometry to explain the power fluctuation phenomenon. Other independent researchers [49] [54] [40] [25] mainly interested in interferometric scale measurements, have ventured successfully to explain the self-mixing effect based on target displacement instead of frequency modulation of the laser source.

3.4.1 Theory Extension

As an extension of the preceding theory to suit our specific needs, let us now derive a simple model taking into account the optical power fluctuation of the laser diode induced by feedback of a fixed external target while under frequency modulation.

First, in Equation 3.31, a current modulation term ΔI will be added to yield

$$P = \eta\left(I + \Delta I + \frac{\kappa_{ext} eV}{LT_s a\Gamma}\cos(2\pi\nu\tau_{ext}) - I_{th}\right) \tag{3.33}$$

In Equation 3.23, a frequency modulation coefficient Ω will be added to vary ν_{th}, the laser's emission frequency without feedback. This yields:

$$\begin{aligned} \Delta\phi_L &= 2\pi\tau_{ext}(\nu - (\nu_{th} + \Delta I\Omega)) + C\sin(2\pi\nu\tau_{ext} + \arctan\alpha) \\ \text{where } C &= \frac{\tau_{ext}}{\tau_L}\kappa_{ext}\sqrt{(1+\alpha^2)} \end{aligned} \tag{3.34}$$

For single mode laser diodes, Ω has a typical value of $-3\ \frac{GHz}{mA}$ at modulation frequencies under around 1 GHz [55].

Figure 3.12 shows a graph of the power fluctuation ΔP versus time for a fixed target distance ($L_{ext} = 30\ cm$) given a triangular modulation signal $\Delta I = 1\ \text{mA}_{p-p}$. Small sharp discontinuities, or more precisely steps, are observed corresponding to the power fluctuations caused by external cavity resonance modes being matched (i.e. external phase shift = multiple of 2π) by the laser light frequency sweep. These discontinuities correspond

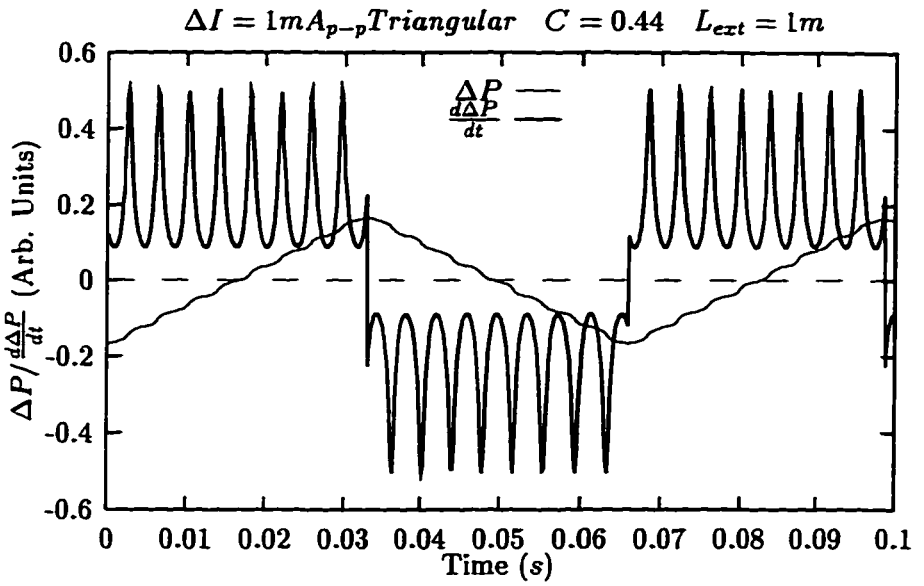

Figure 3.12: Theoretical power fluctuation curves for FM modulated laser

to the power fluctuation in the presence of feedback shown in Figure 3.10. Effectively, the power fluctuation signal as a result of feedback is superimposed onto the triangular modulation signal. As described earlier, while varying the current through the laser diode yields frequency modulation, it also results in amplitude, or light output power modulation. That is why the triangular signal is picked up by the monitor photodiode along with the superimposed power fluctuation signal. The corresponding frequency spacing between the small steps serves to deduce the fundamental resonant frequency of the cavity in order to compute the target displacement. As a comparison, a log of real data was obtained in Figure 3.13. The theoretical model is in very good agreement with the experimental curves. In order to better estimate the spacing between the power fluctuations and remove any common mode signal, the derivative of the photodiode signal ($\frac{d\Delta P}{dt}$) is taken as shown in the theoretical and experimental figures. The derivative signal is composed of positive peaks during the increase of frequency and negative peaks during the decrease. The positive portions of the signal will be termed "positive plateaus" and the negative portions, "negative plateaus". The task now becomes the detection of the peaks and the measure of the average frequency variation which occurred between them. Figure 3.14 illustrates the

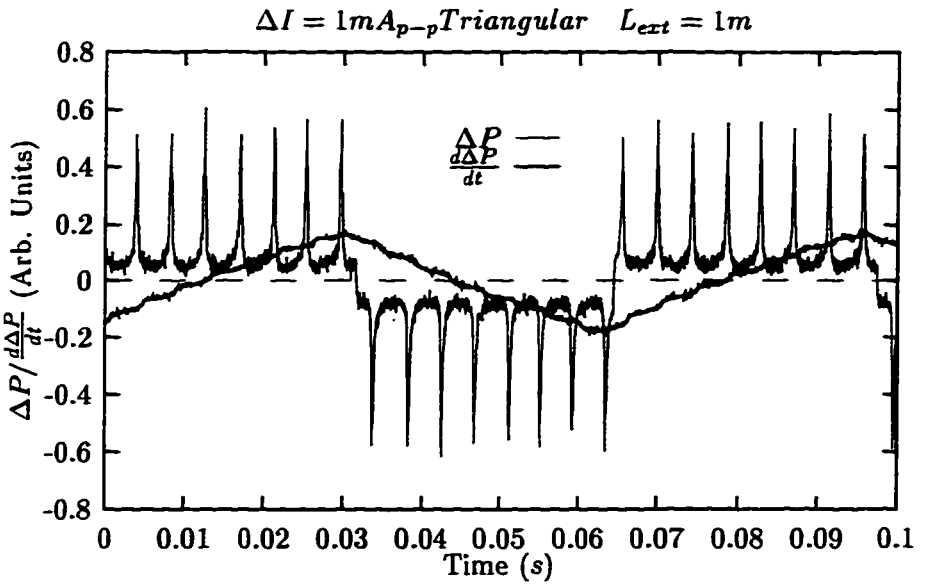

Figure 3.13: Experimental power fluctuation curves for FM modulated laser

effect of varying the coupling coefficient C on the power fluctuation signal (ΔP). As expected, the steps become sharper as C approaches 1, and less defined as C approaches 0.

As described in Equation 3.32, the length of the external cavity will given by $L_{ext} = \frac{c}{2\nu_0}$, where ν_0 is the fundamental frequency of the external cavity determined by measuring the average frequency spacing between successive resonant modes of the cavity. Since resonant modes occur when peaks are observed in the derivative signal, the average frequency spacing between modes will be proportional to the average distance between peaks as a linear relationship exists between the laser diode output frequency excursion and time for a triangular modulation signal. A general relationship may then be formulated:

$$\nu_0 = K_1 \times \text{average positive and negative peak spacing} \qquad (3.35)$$

The proportionality constant K_1 is determined by the current excursion induced by the modulating signal, the frequency of the modulating signal and the frequency modulation coefficient Ω of the laser diode in $\frac{GHz}{mA}$. In practice, this proportionality constant is determined empirically during the calibration of the system. Once ν_0 is measured, L_{ext} is readily obtained

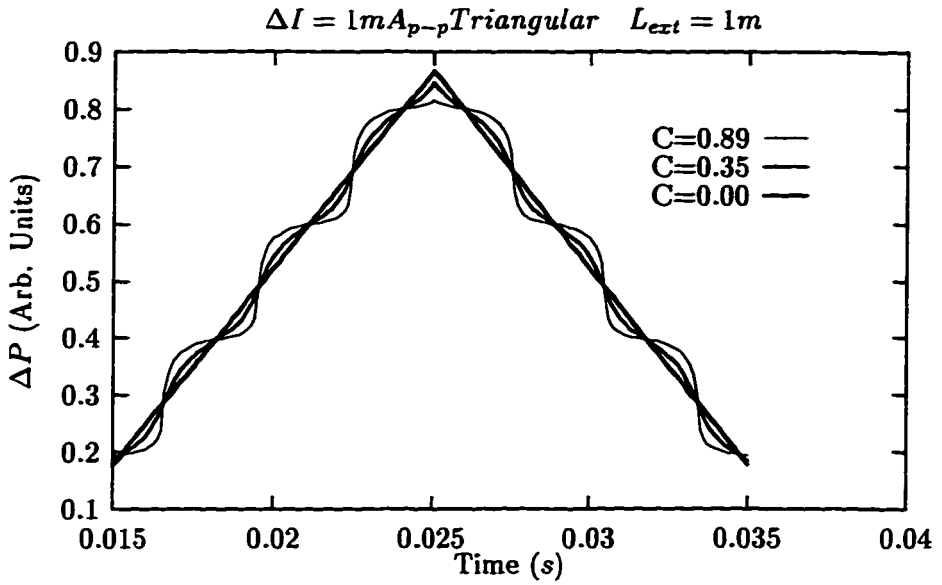

Figure 3.14: FM power fluctuation curves for various values of C

using Equation 3.32 to yield:

$$L_{ext} = \frac{c}{2K_1 \times \text{average positive and negative peak spacing}} \tag{3.36}$$

3.4.2 Velocity Measurement

An additional observation at this point is that it is also possible to measure target velocity based again on the derivative of the power monitor signal. Consider the scenario where the wavelength of the laser light passing through the cavity is linearly increased at a fixed rate (i.e. frequency is decreased). If the target is stable, then the resonant modes will be met at a fixed rate as the frequencies are swept. Now, should the target move away from the laser source at a fixed velocity, then the resonant modes of the cavity will be reached a little later by the frequency-scanning laser. Intuitively, it could be observed that as the target moves away from the source, that the possible resonant mode wavelengths of the cavity are increased. Because of this, it will take a little more time for the increasing wavelength of the scanning laser to catch up with a given cavity mode. Conversely, if the target moves towards the laser source at a fixed rate while the swept output light wavelength is increased (i.e. frequency is decreased), then the resonant modes

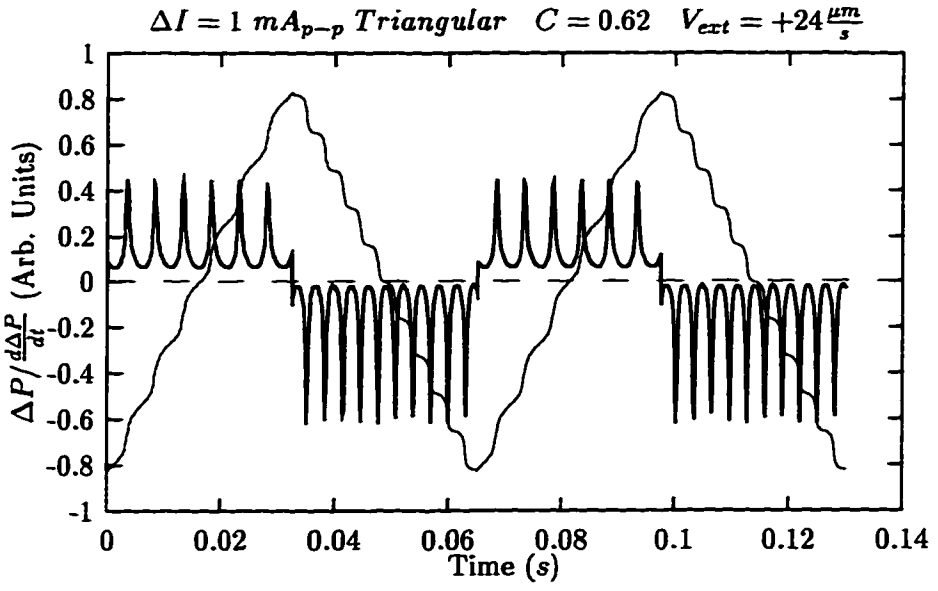

Figure 3.15: Theoretical power fluctuation for a receding target. The power modulation and derivative signal are shown for a target moving at a rate of $24\frac{\mu m}{s}$ away from the laser diode. The peak spacing varies depending on the increasing or decreasing laser diode output frequency.

of the cavity will be met a little sooner. When the wavelength of the laser light is instead decreased (i.e. frequency is increased), the resonant modes will be met sooner when the target moves away and later when it moves towards the laser source. Empirically, the results of this phenomenon will be observed in the difference in frequency spacing between the positive peaks and the negative peaks. In fact, if the target is moved away from the laser source, the peaks will be spaced closer together as the frequency of the laser diode is increasing and farther away when the frequency of the laser diode is decreasing. Figures 3.15 and 3.16 illustrate simulations obtained from the developed theoretical model of power fluctuation curves as the target is moved. Figure 3.15 illustrates the case where the target is moved away from the laser source at a rate of $+24\frac{\mu m}{s}$. As described earlier, the peaks in the derivative signal are more closely spaced as the frequency of the laser light is increasing, which corresponds to a decreasing slope of the power signal as observed in the figure. Remember that when the current (thus the optical power) in a laser diode is increased, the output frequency of the laser light

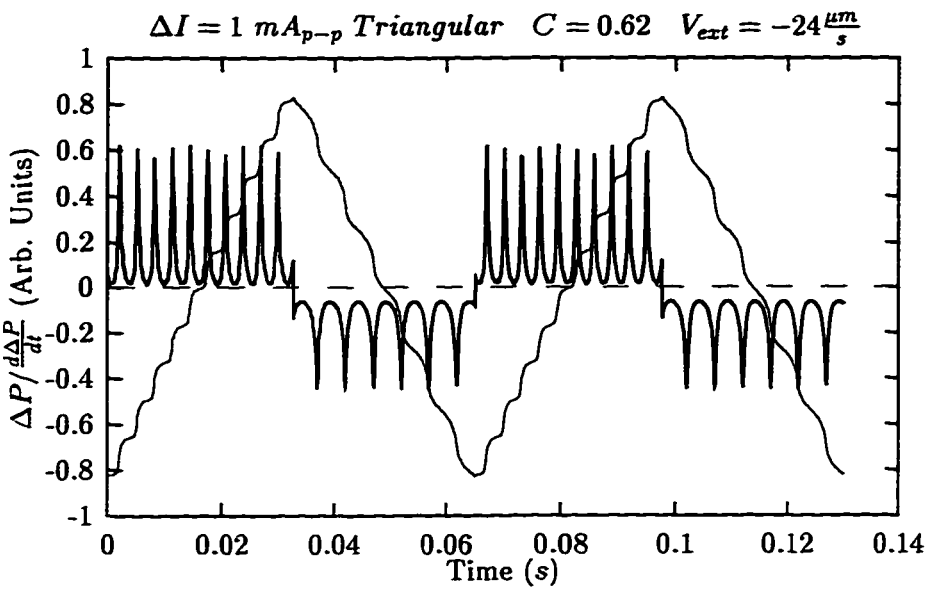

Figure 3.16: Theoretical power fluctuation for an approaching target. The power modulation and derivative signal are shown for a target moving at a rate of $24\frac{\mu m}{s}$ towards the laser diode. The peak spacing varies depending on the increasing or decreasing laser diode output frequency.

is correspondingly decreased due to thermal expansion of the lasing cavity. Again from the figure, it is observed that when the frequency of the laser source is decreased, the peak spacing is increased. Figure 3.16 displays the result of the target moving towards the laser source at the same rate. Here, as the light frequency is increasing, the peak spacing decreases, and as the light frequency is decreasing, the peak spacing increases.

The velocity of the target is related to the peak spacing by the following relation:

$$\text{velocity} = K_2 \times (\text{average negative} - \text{average positive peak spacing}) \quad (3.37)$$

where K_2 is the empirically determined proportionality constant. Note that when using the peak spacing for range measurements, averaging over the positive and negative peak spacings will cancel out this effect and yield an average value between the two.

3.4.3 Consideration of Target Vibrations

A practical observation was made using the developed theoretical model. As was described in the earlier theoretical developments, power fluctuations in the laser power monitor photodiode signal are detected as external cavity resonant modes are encountered, that is when the round trip phase shift of the light through the external cavity equals an integer multiple of 2π. This was shown to happen through motion of the target given a fixed laser light output frequency. A periodic power fluctuation was demonstrated every time the target was displaced by a distance equal to half the wavelength of the laser light. Alternatively, the power fluctuation was also shown possible through frequency ramping of the laser light source given a fixed target. In practice, it is difficult to image a truly fixed target, especially in an industrial setting where vibrations are ubiquitous. That is why it is important to simulate the interaction of target vibrations while operating in an FM modulation regime. Figure 3.17 illustrates the simulation results. Here, a target at a nominal distance L_{ext} in front of the laser diode is vibrated along a sinusoidal path ΔL_{ext} shown in the figure around this nominal distance. The amplitude of the vibration corresponds to a distance a little over a wavelength of the laser light. The frequency of the vibration is in this case comparable to that of the modulating signal. This example serves to simulate mechanical vibrations in a target to be imaged, a very practical scenario. As shown in the figure, the amplitude of the peaks becomes modulated in a non-trivial manner by the vibrating external cavity. Some peaks are higher when the cavity's resonant frequencies are decreasing/increasing

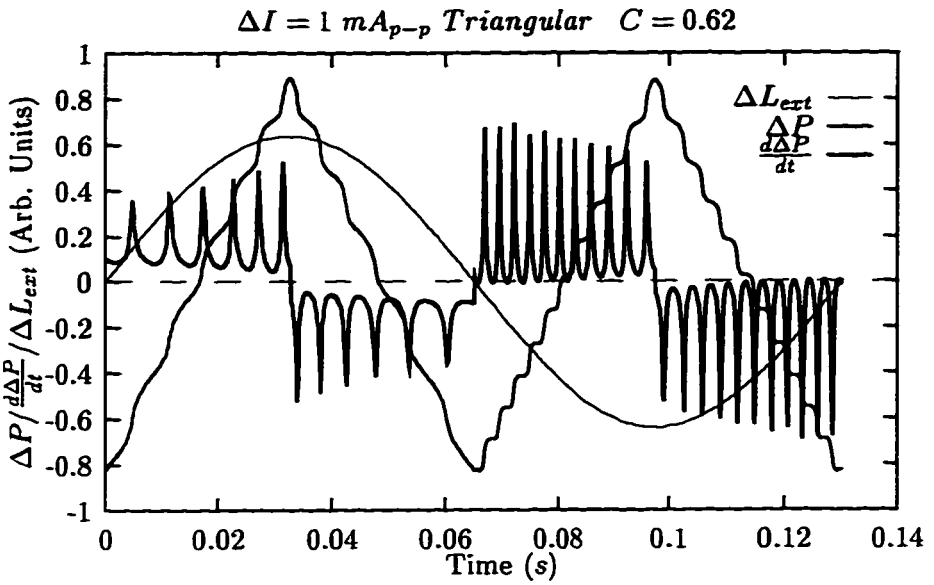

Figure 3.17: Theoretical power fluctuation for a vibrating target. The power modulation and derivative signal are shown for a target vibrating along a sinusoidal path ΔL_{ext} around the nominal target distance L_{ext}. The amplitude of the vibration corresponds to a distance a little over a wavelength of the laser light. The frequency of the vibration is in this case comparable to that of the modulating signal. Interference effects are observed in the amplitude of the peaks.

while the laser diode's sweeping frequency is increasing/decreasing. This may be likened to two automobiles meeting on the highway by traveling in opposite directions. Their encounter time will be much shorter than when the two cars are going in the same direction and one suddenly passes the other. Similarly, in our system, when the external cavity is expanding, its resonant frequencies are swept down, or decreased. If at the same time, the frequency of the laser is increased, the two will meet very quickly and the power fluctuation observed in time will be very brief as they are "going towards each other". The time derivative of the resulting power fluctuation signal will therefore have a high peak value. When the external cavity is instead contracting, its resonant frequencies are swept up, or increased. If the laser frequency is still increasing, the two will meet over a longer period of time as they are "catching up to each other" instead of "going towards each other". The resulting time derivative of the power fluctuation signal will therefore have a lower peak value. This explains the varying peak amplitude over the derivative signal. Note that this was also observed in Figures 3.15, and 3.16 where constant velocity target motion was used instead of sinusoidal motion. If excessive noise amplitude is present, some peaks may be lost and the overall signal distorted beyond recognition. The instantaneous peak spacing, however remains unchanged.

This example illustrates an important point. If the laser diode's FM modulation signal frequency were chosen to be well above the mechanical noise vibration frequency, then much of the signal distortion would be avoided. The mechanical time constants would effectively become negligible with respect to the short sampling time. This observation will represent a design guideline for the final 3D scanner as the beam steering unit will generate mechanical interference in the form of settling vibrations.

3.5 Operational Constraints

3.5.1 Temperature Dependence of Laser Diode Frequency

Note that one must be careful when selecting the operating current, the modulation current intensity, and most importantly the operating temperature of the laser diode. This is due to the potential mode-hopping of the laser frequency output due to thermal expansion of the laser cavity. Figure 3.18 shows a typical graph of the nominal output wavelength of a semiconductor laser versus temperature. The breaks in the curve indicate mode hops. In this case, mode hops occur when the laser being in a given mode of oscillation sees the resonant cavity increase in length as a result of thermal expansion.

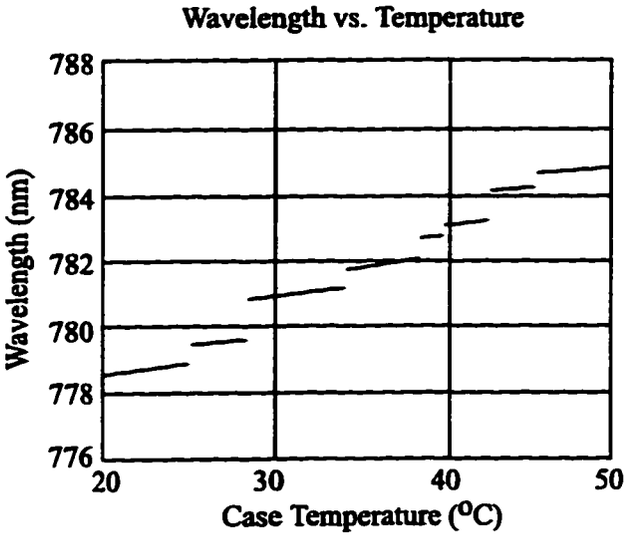

Figure 3.18: Output wavelength of a semiconductor laser diode vs. temperature

Typically, a cavity will expand by $0.06\frac{nm}{^oC}$ for AlGaAs devices [55]. The lasing frequency adjusts (lowers) to the new cavity length in order to satisfy the phase condition. The lasing medium however has an energy spectral distribution which varies at a different rate with temperature increase. Typically, the gain curve will vary by $0.25\frac{nm}{^oC}$ with respect to the laser wavelength for AlGaAs devices [55], a faster rate of increase (N.B. increase in wavelength $\Rightarrow$ decrease in frequency). Figure 3.19 illustrates the situation. Part (A) represents the initial spectral output with temperature at 27^oC. As the temperature is *decreased*, the possible resonant cavity modes are shifted to the right due to the reduction of the compound cavity length. In part (B), a quasi-linear increase of the output frequency of the laser is observed. This occurs in order to satisfy the lasing phase condition in the compound cavity. In part (C), the temperature is decreased beyond the point where a mode hop occurs. An abrupt jump in the laser frequency (mode hop) is observed as a neighboring mode suddenly becomes the dominant mode with respect to the frequency dependent gain spectrum $g(\nu)$ of the gain medium.

These temperature-dependent frequency jumps are undesirable in a ranging system in which a well-behaved linear frequency modulation is assumed to exist. For this reason, temperature stabilization is essential as the lasing frequency may vary as much as $-30\ \frac{GHz}{^oC}$ in addition to exhibiting mode

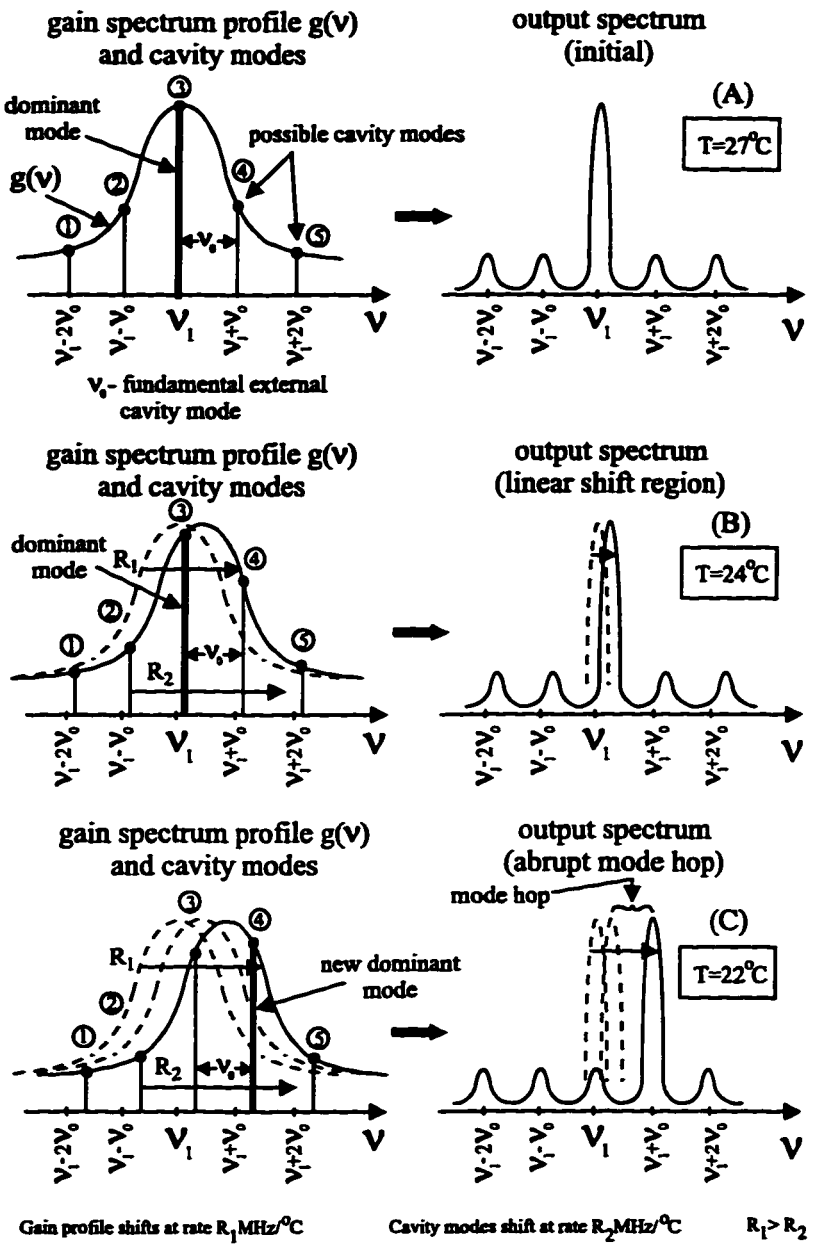

Figure 3.19: Mode hopping phenomenon. As the temperature is *decreased*, the laser cavity length *decreases*, thus the lasing frequency *increases* so as to satisfy the phase condition. When decreased too far, a neighboring mode abruptly dominates and the cycle repeats.

hops. By adjusting the regulated temperature operating point in the middle of a plateau, that is as far as possible from neighboring mode hops, stable operation is possible.

3.5.2 Coherence Length Ranging Limitation

A fundamental limit on all coherent detection systems is the coherence length of the laser light. The coherence length refers to the round-trip distance beyond which the laser light loses its coherence with respect to the light at the source. This is attributed to a random wandering of the phase in time. Beyond the coherence length, the laser light may no longer effectively give rise to constructive or destructive interference with the light inside the cavity. The coherence length is proportional to the inverse of the bandwidth of the output light frequency spectrum. The smaller the bandwidth, the purer the light becomes and thus, the longer its coherence length. An ideal laser source would emit a single frequency, yielding a zero bandwidth and an infinite coherence length. In practice, however, visible laser diodes have coherence lengths of the order of a few centimeters or less. GaAs single mode laser diodes may have typical coherence lengths of a few meters.

It is known [49] that the feedback of laser light in the resonant cavity of a laser changes its spectral bandwidth property. The relation describing this effect is given by Equation 3.38 (for $C \ll 1$):

$$\delta\nu = \frac{\delta\nu_0}{[1 + C\cos(\phi_{ext} + \arctan(\alpha))]^2} \tag{3.38}$$

where $\phi_{ext} = 2\pi\nu\tau_{ext}$ is the external cavity round trip propagation delay, C is the feedback coefficient, and α is the linewidth enhancement factor. $\delta\nu_0$ is the linewidth (spectral bandwidth) of the output light without feedback. Typically, $\delta\nu_0 = 60$ MHz. This linewidth can be increased or reduced depending on the external phase, yielding the new linewidth $\delta\nu$. The external phase may be varied through target displacement. This property may be conveniently used to reduce the linewidth of a laser source and increase its coherence length by several orders of magnitude. This is performed by adjusting the distance between the laser source and an external reflector. Maximum linewidth reduction occurs when $\phi_{ext} = -\arctan(\alpha)$. It is however difficult mechanically to maintain the crucial alignment accurate to within a quarter of a wavelength. If this distance should fluctuate by a quarter of a wavelength, the linewidth would be instead be enlarged.

In the FM ranging system, because of the coherence length limitation, the maximum measurable distance should therefore be equal to half of the

laser diode's coherence length. With the self-mixing effect however, the feedback from a distant target may actually increase the coherence length as described above. This effectively makes measurements beyond half of the coherence length possible. The converse however is also true. In general, it is therefore difficult to establish an exact limit on the maximum usable range of the system as it depends on the operating conditions of the system [40].

Chapter 4

Experimental 1 DOF Laser Ranging System

An experimental ranging system based on FM modulation of an infrared semiconductor laser diode was designed and built. This single degree of freedom (DOF) system serves to measure the range to a fixed target by evaluating the external cavity frequency mode spacing (see section 3.4). The final 3D laser range scanner requires the addition of a beam steering unit to this 1 DOF system, and will be presented in the next chapter. The details of the design of the 1 DOF system will now be presented.

4.1 System Architecture

Figure 4.1 illustrates the overall system architecture of the FM laser ranging system. A laser diode is first mounted on a temperature-stabilized heat sink. This allows for a steady output light frequency independently of the environmental temperature conditions. The operating temperature is adjusted as to be far away from temperature induced mode hops (see subsection 3.5.1). A temperature sensor is embedded into the heat sink, in thermal contact with the laser diode case. The temperature of this heat sink is controlled by means of a thermoelectric heating/cooling unit (Peltier junction). With the help of a closed-loop PID temperature controller circuit, the heat sink temperature is constantly being monitored through the temperature sensor, and is controlled by the thermoelectric heat pump. Depending on the direction of the current flow through the thermoelectric device, the unit will remove or add heat to the heat sink, allowing for a single point temperature regulation.

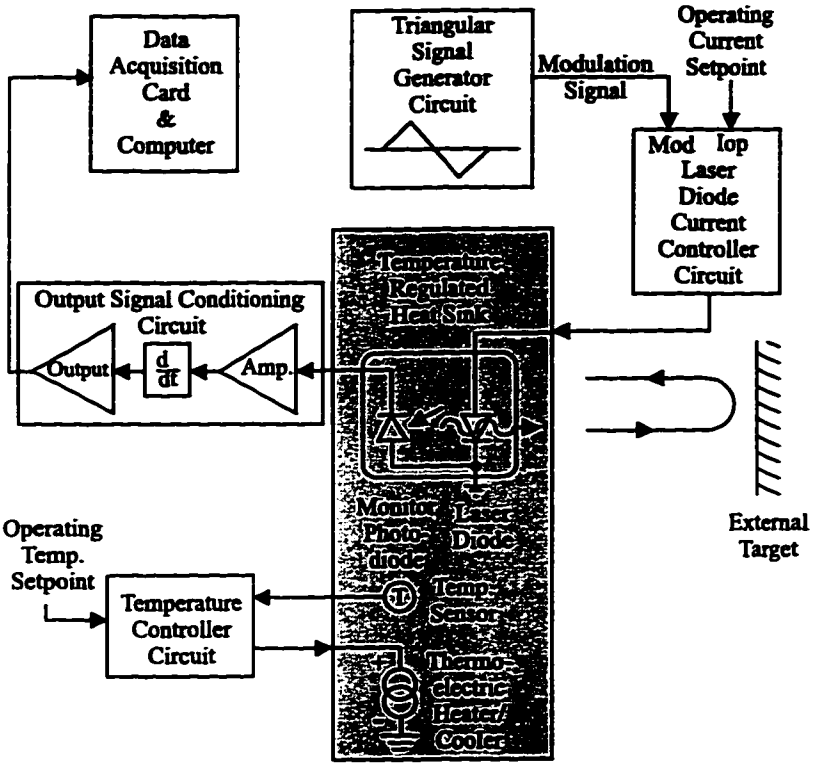

Figure 4.1: 1 DOF FM laser ranging system architecture

The laser diode is driven by a current controller circuit which biases it at a preset operating current value. A modulation circuit allows variation of the drive current around the operating point in proportion to the modulation signal. The source of the modulation signal is a triangular signal generator. The frequency and amplitude of the signal are preset by the user.

Finally, the monitor photodiode output is amplified and differentiated by the output signal conditioning circuit. Any common mode component of the signal is effectively eliminated through the differentiation operation (see Figure 3.13). An output stage also couples the resulting differentiated output signal to the computer's data acquisition board for digital processing. During processing, range (or velocity) information from the target is ultimately computed.

4.2 Performance Requirements

In subsection 3.5.1, it was mentioned that laser diodes exhibit strong output light frequency dependence on temperature. Typically, a laser diode's output frequency will vary by $-30\ \frac{GHz}{^oC}$ [55]. In comparison, it was mentioned in section 3.3.3 that the output frequency dependence on drive current for AlGaAs devices was of approximately $-3\ \frac{GHz}{mA}$ for modulation frequencies below about 1 GHz. The modulating signal will typically induce a ± 0.5 mA current fluctuation in the laser diode, resulting in a 3 GHz total frequency excursion. This is more than adequate to sweep numerous resonant modes of a practical external cavity.

4.2.1 Temperature Controller Requirements

The FM ranging system relies on the production of a controlled and steady output frequency sweep as the input triangular modulation signal is applied regardless of the external environmental conditions. Also, from Figure 3.4, it was observed that the output light intensity of a laser diode was dependent on temperature for a fixed drive current. The internal monitor photodiode usually reserved for the purpose of regulating the output light intensity through feedback current control of the laser diode will instead be used to monitor power fluctuations due to optical feedback. These two requirements impose the need for external temperature regulation. By actively regulating the temperature of the laser diode to within $\pm 0.001^oC$, the resulting temperature-induced frequency "noise" will be reduced to $-30\ \frac{GHz}{^oC} \times \pm 0.001^oC = \mp 30$ MHz. This represents a 1% frequency noise variation with respect to the 3 GHz useful current-induced excursion,

a respectable figure. Keep in mind that technically speaking, since we are interested only in resonant mode spacings, or relative measurements, the temperature only needs to be held constant during a sampling interval while the frequency is modulated over several cycles.

4.2.2 Laser Diode Driver Requirements

The laser diode driver and modulation circuit is a crucial part of the ranging system. It is important for the circuit to be low-noise and stable. As quoted above, the light output frequency dependence on current is of $-3\ \frac{GHz}{mA}$. Any noise in the laser diode driver will in turn induce FM noise in the output light which will directly affect the spacing measurement accuracy of the resonant frequencies of the external cavity. This will randomly increase or reduce the spacing between the observed peaks of the derivative output signal (see Figure 3.13). In essence, a linear relation is assumed between the modulation current and the frequency output excursion of the laser light. Any superimposed noise will result in the actual lasing frequency being slightly off the desired frequency by a random time-varying amount. Our goal is to reduce as much as possible this noise, which will obviously be present throughout the sampling interval of the ranging signal. By carefully designing a low-noise current regulation circuit with a peak noise figure of $\pm 1\ \mu A$, the corresponding FM noise will be $-3\ \frac{GHz}{mA} \times \pm 1\ \mu A = \mp 3$ MHz. This corresponds to 0.1% FM noise with respect to a standard 3 GHz excursion.

In addition to the low-noise modulation system, a laser diode needs protection against a number of potentially dangerous electrical conditions. In general, transients should be eliminated, or diverted away from the laser diode. This is especially important when the circuit is turned on or turned off. This may be dealt with by designing a slow current turn-on circuit and adding a protection high speed snubber circuit across the leads of the laser diode. Reverse current conditions should also be carefully monitored or avoided as the reverse breakdown voltage of laser diodes is usually fairly low, and as a consequence, large reverse currents may damage the device. A reverse-biased diode in parallel with the laser diode will provide some protection. Obviously, the maximum rated forward current of a laser diode should never be exceeded (including while under modulation). Laser diodes are also very susceptible to static electricity damage.

4.2.3 Waveform Generator Requirements

The modulation signal inducing the frequency sweep is to be a triangular signal. This implies that the frequency sweep relationship will be linear with time. Again, it is important for the linearity of the triangular wave to be as high as possible as it will be assumed linear in the signal processing step. The noise content of the waveform will also be replicated (though in a much smaller version) in the laser diode drive current waveform by the modulation circuit. The frequency stability of the waveform is also an issue as it was observed in the experimental system to induce final errors ($\frac{\Delta(mm)}{\Delta(Hz)}$) of the order of 20 $\frac{mm}{Hz}$. Thus, for every Hertz of frequency deviation, the final range measurement was off by roughly 20 mm. This constitutes a rather high sensitivity, and therefore might become one of the limiting accuracy factors.

4.3 Prototype Construction Techniques

All the circuit prototypes were built using wire-wrapping and soldering methods. Low-noise techniques were used such as minimizing long wire runs, and star grounding of the integrated circuits. All resistors used were 1% metal film resistors unless otherwise noted. The OP - 27 operational amplifier was used in the designs. 0.1 μF decoupling capacitors were placed across the supply rails of each integrated circuit, as close as possible to the actual power pins. Bypass capacitors have also been placed across the feedback paths of each amplifier in order to introduce poles in their closed-loop gain frequency response. This increases stability and reduces high frequency noise.

4.4 High Accuracy Temperature Controller

C.C. Bradley *et al.*[56] have described a temperature controller circuit capable of stabilizing the temperature of a heat sink-mounted laser diode to within $\pm 0.0003°C$ as measured for a period of 1 hour. The circuit consists of a PID controller coupled to a power output stage driving a thermoelectric heat pump (Peltier Junction). The temperature sensing element used is a thermistor mounted in a Wheatstone bridge configuration with the temperature setpoint potentiometer. It was observed that in order to regulate the temperature of the laser diode, the thermistor had to be mounted as close as possible to the laser diode casing. C.E. Wieman and L. Hollberg [55]

also described a temperature stabilization circuit for use in regulating the temperature of laser diodes. Here again, a PID feedback loop was employed with a thermistor temperature sensor. Their circuit achieved a $\pm 0.001°C$ temperature stability.

4.4.1 Electrical Design

A novel temperature stabilization circuit was devised based on the $AD590$ semiconductor temperature sensor while possessing some similarities to [56] and [55]. The circuit is illustrated in Figures 4.2, 4.3, and 4.4. The general principle behind the circuit is based on a negative feedback control loop with Proportional-Integral-Derivative (PID) gain driving a thermoelectric device. The temperature setpoint input to the control system is first provided by the help of a precision $10-$ turn wirewound potentiometer $R19$. The temperature coefficient of the potentiometer is of 25 $\frac{ppm}{°C}$. The potentiometer is connected in a voltage divider configuration, fed by $IC1$ an $R1$ which form a high stability voltage reference source. The following 2^{nd} order low-pass filter formed by $R20$, $R21$, $C17$ and $C18$ serve the purpose of filtering the noise from the temperature demand circuit. $IC1$ is a $LM399$ precision, temperature-stabilized monolithic Zener diode with a temperature coefficient of 0.5 $\frac{ppm}{°C}$. The high accuracy voltage reference provided by $IC1$ and $R1$ is also used as an input to the $AD590$ temperature sensor amplifier circuit formed by $IC3$ and surrounding components. $R4$ is first adjusted to produce a 0 mV output when the sensor is immersed in freezing water. This effectively nulls the offset. Then, $R6$ is adjusted to provide a 100 $\frac{mV}{°C}$ calibrated output. This adjusts the gain of the amplifier circuit. The output of the $IC3$ amplifier is then low-pass filtered, here again to remove noise. At this stage, a precision temperature setpoint and temperature monitor signal are available. $IC7$ configured as a voltage follower serves as a high input impedance buffer driving an LCD instrumentation digital panel voltmeter (DPM) module. The DPM requires an external floating power source provided by a $9V$ battery. The output is scaled by 0.1 by the $R24$, $R25$ voltage divider in order not to exceed the LCD display's input voltage range while conserving calibrated units directly displaying the temperature. Switch $SW2$ allows selecting the DPM's input source, the temperature setpoint, or the monitored temperature. LED's 1 and 2 serve as indicators of which of the two inputs is being displayed.

The next stage of the circuit involves the generation of the temperature error signal obtained by taking the difference between the temperature setpoint signal and the actual temperature signal. A high Common Mode

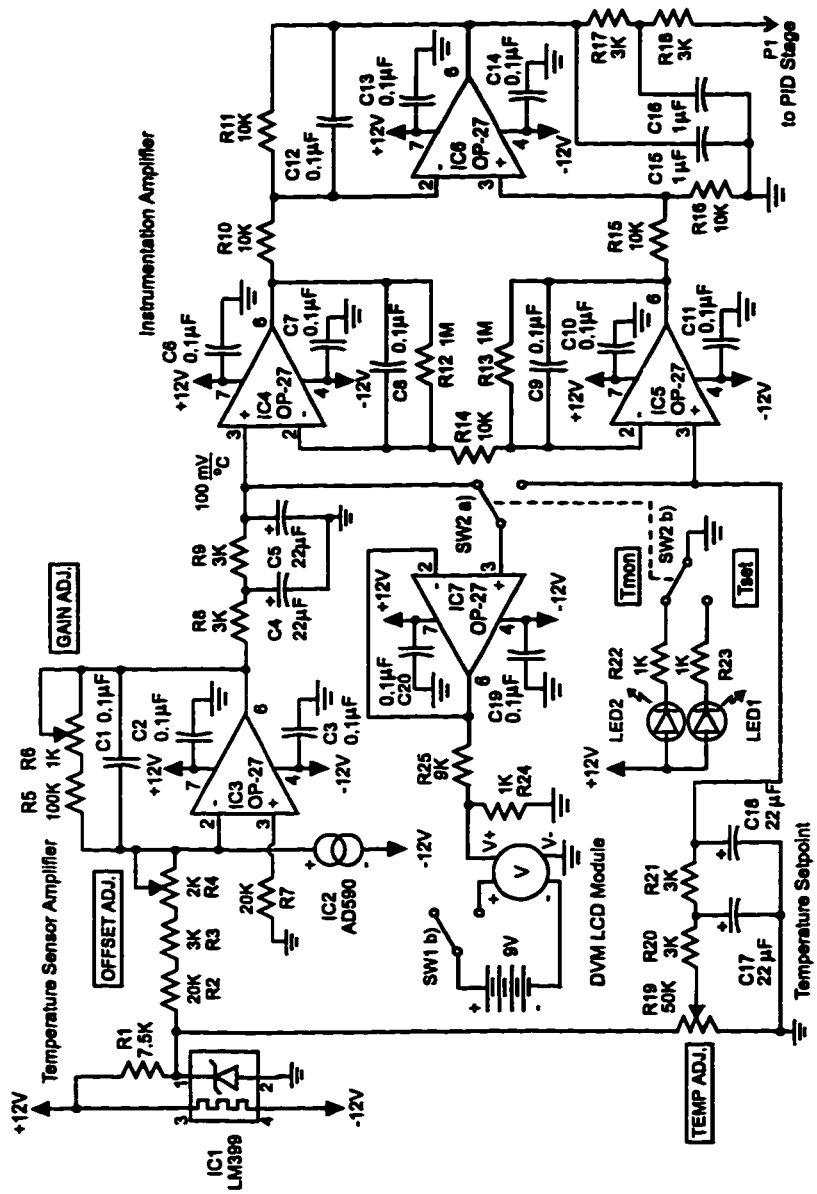

Figure 4.2: Temperature controller circuit part A

Rejection Ration (CMRR) differential amplifier is required in order to amplify the very small differences between the two signals while not being affected by the relatively high common modes. For example, a temperature difference of $\pm 0.001^{o}C$ at room temperature ($25^{o}C$) will yield a common mode signal of 2.5 V and a difference of 0.1 mV. For this reason, an instrumentation amplifier[57] design was chosen. $IC4$, $IC5$ and $IC6$ form a high CMRR instrumentation amplifier with a differential signal gain of 201. The output temperature error signal of the instrumentation amplifier is low-pass filtered by $R17$, $R18$, $C15$ and $C16$ as to reduce output noise. The resulting temperature error signal is then coupled to the PID gain stage illustrated in Figure 4.3.

The PID gain stage allows the tuning of the control loop parameters to ensure a fast response while maintaining good stability. $IC8$ serves as a high input impedance buffer to the RC filter and drives the PID stage along with the temperature monitor output provided by $IC9$. This output error monitor allows tracking of the temperature error signal with an output gain of 20 $\frac{V}{^{o}C}$. $IC11$ configured as an inverting amplifier provides the proportional gain adjusted by $R32$. $IC12$ configured as a standard integrator provides the integral gain set by $R31$. Finally, $IC10$ configured as a standard differentiator provides the differential gain which is adjusted by $R30$. The three quantities are then added together through the inverting summer formed by $IC13$. The output of the summer stage then is coupled to the power output stage driving the thermoelectric junction, illustrated in Figure 4.4.

$Q1$ and $Q2$ are complementary silicon power Darlington transistors. They form a push-pull output stage capable of supplying up to 12 A of current. The transistors are operated in a feedback loop through the use of $IC14$. The input voltage level on pin 3 of $IC14$ is used as a reference and is actively matched with the sampled voltage across the thermoelectric heat pump, or Peltier Junction induced by the output signal of the op-amp driving the transistors. When the current flows in one direction through the Peltier Junction, the heat is pumped from one side of the junction to the other. When the current is reversed, the heat flows in the opposite direction. The removal or addition of heat with respect to one side of the Peltier Junction may thus be controlled by the polarity of the current flow. $C42$ and $R43$ are inserted for loop stability. $R40$, $D1$, $D2$ and Zener diodes $ZN1$ and $ZN2$ form a bipolar input voltage clamp preventing the input demand to cause excessive current to pass through the Peltier Junction. The breakdown voltages of the Zener diodes have been selected as to let a maximum of 1 A of current to flow through the heat pump given a full input swing. Fuse $F2$ was added for additional protection in the event of circuit failure.

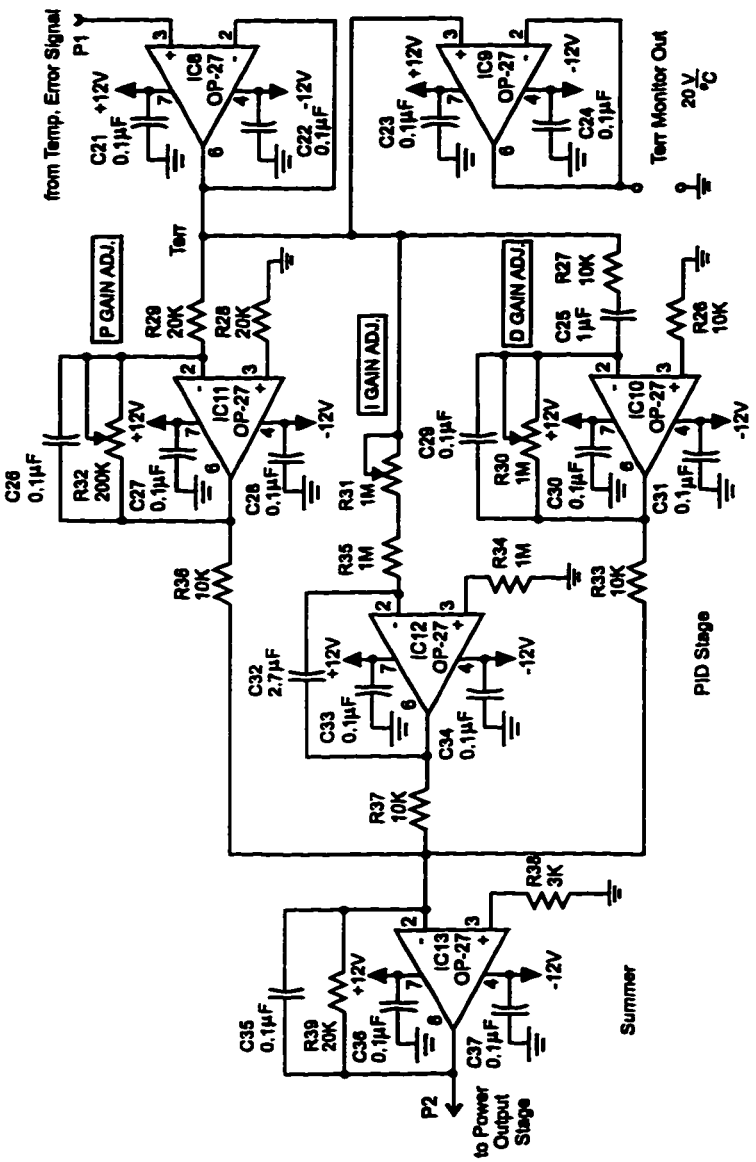

Figure 4.3: Temperature controller circuit part B

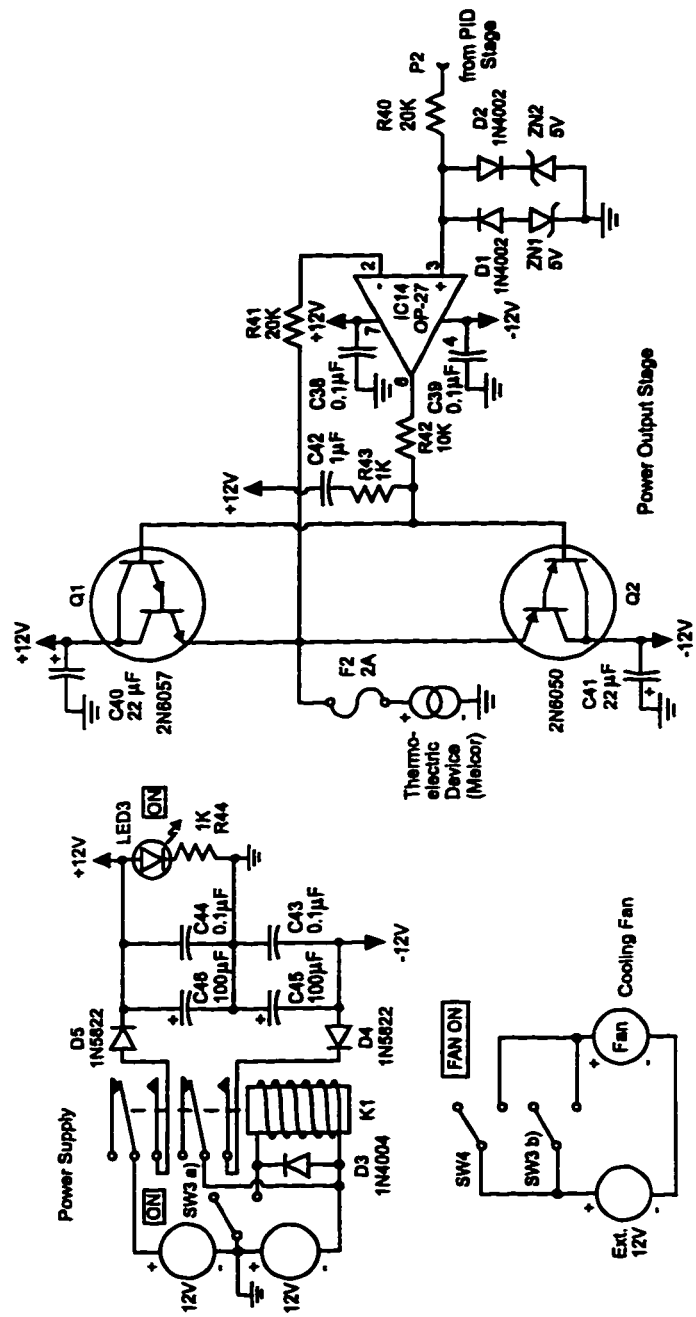

Figure 4.4: Temperature controller circuit part C

Figure 4.5: Picture of the temperature controller prototype

The power to the circuit is provided by an external bipolar supply. Relay $K1$ was installed to serve as the main switch to the temperature controller circuit when switch $SW3$ is operated. This eliminates the problem of one side of the bipolar power supply turning off before the other side when switched off. This may result in harmful turn-off transients in the output stage. By adding a relay cutting off the two sides quasi-simultaneously, this turn-off voltage mismatch time is considerably shortened, and is repeatable independently of the power supply used, and its filtering capabilities. $D5$ and $D4$ provide reverse polarity protection. $C43$ to $C46$ provide line filtering and $LED3$ is the indicator for the temperature circuit being enabled. A cooling fan is mounted near the power Darlingtons providing active cooling. It is automatically enabled by turning on the temperature controller switch $SW3$ or by an external switch $SW4$.

Figure 4.5 shows a picture of the built prototype circuit. The prototype was fabricated using wire-wrapping and soldering methods. Low-noise techniques were employed such as minimizing wire runs and using star grounding to all integrated circuits.

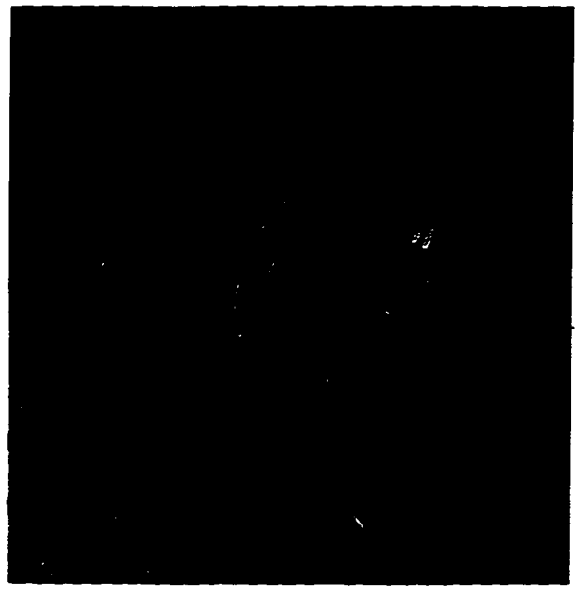

Figure 4.6: Picture of laser head unit. The laser diode is inside the cylindrical collimation unit at the center of the module.

4.4.2 Mechanical Design

It is necessary to regulate the case temperature of the laser diode which will be used in performing range measurements. The mechanical mounting detail of the laser diode and temperature regulation unit is shown in Figure 4.6. The laser diode is first inserted inside a special metallic lens collimating unit. This allows the collimation of the laser beam into a parallel beam. The collimation unit is cylindrical in shape. It is secured to a frontal aluminum rectangular plate serving as the laser diode heat sink. A $\frac{1}{2}$ " axle collar retains the collimation unit secured through the set screw. Two side clamps hold down the collar. All the metallic junctions are covered with thermal compound to increase thermal conductivity. The temperature sensor is mounted inside a hole drilled in the frontal heat sink very close to the laser diode. A rear heat sink is placed at the rear of the frontal one. The Peltier junction wafer is sandwiched between the two with the help of thermal compound and bolts. When activated, the Peltier junction effectively transfers heat from one of the heat sink to the other depending on the polarity of the current flow. Therefore, under normal thermal regulation through the feedback circuit, one heat sink will become the cold side and

the other, the hot side depending on the temperature setpoint.

4.4.3 Controller Performance

The circuit was energized and the PID gain loop was tuned as to yield a close to critically damped response. Once adjusted, the circuit was used to regulate the temperature of the laser diode heat sink both below and then above room temperature over the course of several hours. The output temperature error monitor signal was observed. Fluctuations within $\pm 0.001°C$ were recorded. For short periods of time (under a minute), fluctuations were less than $\pm 0.0005°C$. Experimentally, it was determined that a potential problem may arise when the heat accumulates on the hot side of the junction at a faster rate than it is being evacuated (i.e. by natural convection). This appears when the demanded temperature is set to be much lower than the room temperature. In this case, the power stage saturates, trying to remove heat from the laser diode as to lower its temperature. Effectively, the laser diode side of the Peltier juction cools down, and the other heats up as the pumped heat collects on the hot side. If this heat is not evacuated by an external means, such as natural convection or a fan, the excessive heat eventually heats up both sides of the device through convection currents and direct contact due to the small spacing between the cold and hot side (3 mm). The temperature of the cold side then begins to slowly heat up with increased current instead of cooling down, effectively causing a thermal runaway. To solve this problem, either the temperature setpoint may chosen to be above the room temperature or slightly below ($< 10°C$). If a much lower operating temperature is still required, than a fan should be installed to evacuate the heat at a faster rate than it builds up. In the experimental system, the setpoint was chosen to be around the room temperature and no external fan was added. It is usually good practice however to always include a heat removal fan when using Peltier Junctions.

4.5 Low Noise Laser Diode Driver

K.G. Libbrecht *et al.* [58] described a circuit used to drive a semiconductor laser diode. In essence, the circuit is based on a high accuracy resistor placed in series with the laser diode (LD). The potential drop across the resistor, proportional to the LD drive current is used in a feedback circuit. The feedback loop has a drive current setpoint input provided by a precision potentiometer and voltage reference. The error signal drives a MOSFET, supplying the drive current to the LD. Effectively, the feedback arrangement

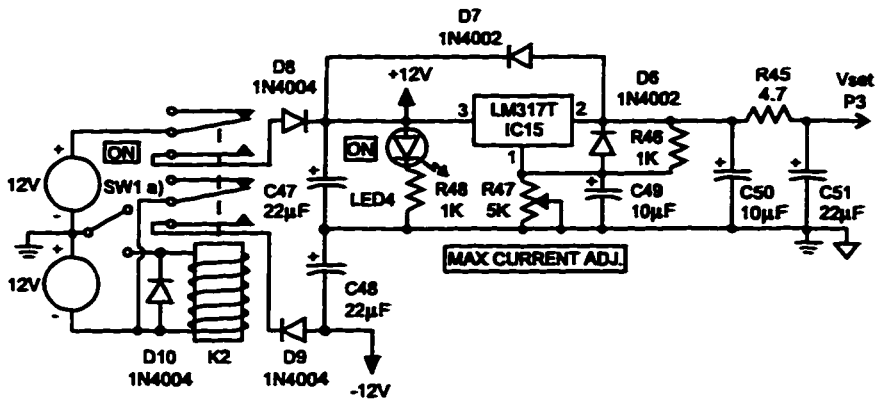

Figure 4.7: Laser diode controller circuit part A

matches the drive current to the demand current. Also, a modulation subcircuit was devised. Configured as a dual compensating circuit, it allows for the injection or the withdrawal of current through the LD branch without modifying the laser diode's operating point. Wieman [55] also presented two circuits capable of driving laser diodes. Here again, the laser diode current is regulated through the use of a current sense resistor. S. Cafferty *et al.* [59] have described a laser diode current controller with added protection circuits to be used with highly fragile and sensitive lead-salt laser diodes.

4.5.1 Electrical Design

A new laser diode controller circuit was designed and built. The circuit possesses some features similar to both [58] and [59]. The circuit allows driving of the laser diode through a high accuracy constant current source. It also has a modulation input to allow varying of the laser diode drive current around the operating point. Several safety features have also been added to protect the sensitive laser diode. They include fast shut-off of the laser diode current in the event of fault detection. Faults include supply undervoltage, laser diode overcurrent, and manual emergency stop. Protection against transients has also been added around the laser diode. Slow-start circuitry allows the slow increase of drive current at turn-on to avoid current spikes through the laser diode. The circuit is shown in Figures 4.7, 4.8, 4.9, and 4.10.

Figure 4.7 shows the power supply for the laser diode controller. The power to the circuit is provided by an external ± 12 V bipolar power supply.

Relay $K2$ was installed to serve as the main power switch to the circuit when switch $SW1$ is operated. $D10$ provides inductive kickback transient elimination from the relay $K2$. $D8$ and $D9$ provide reverse polarity protection. $C47$, $C48$, and $C50$ provide line filtering and $LED4$ is the indicator for the laser diode controller circuit being enabled. The purpose of the $LM317T$ adjustable voltage regulator ($IC15$) is to provide an adjustable voltage which will feed the laser diode branch. This allows setting through $R47$ of the maximum branch current able to pass through the laser diode. It constitutes the first level of overcurrent limit safety precaution. An RC filter is provided by $R45$ and $C51$ to produce reasonably slow ramp-up of the laser diode supply voltage V_{set} during turn-on.

Figure 4.8 shows the laser diode constant current control circuit along with the modulation subcircuit. The essence of the constant current driver is based on a feedback system which matches the current demand set by the user through a precision $10-turn$ potentiometer $R79$ to the monitored current passing through a high accuracy resistor $R60$ (Vishay $0.1\%, 25\ \frac{ppm}{^oC}$) in series with the laser diode $LD1$. The current demand circuit is similar to the temperature demand circuit described in 4.4.1 except that it is referenced to the V_{set} laser diode supply rail instead of being ground-referenced. The circuit consists of a high stability voltage reference formed by $IC18$ an $R55$. A 2^{nd} order low-pass filter then follows formed by $R56$, $R57$, $R58$, $C55$ and $C56$. It serves the purpose of filtering the noise from the current demand circuit. Also, since the time constant of the circuit is in the order of seconds, it produces a slowly increasing current demand at start-up, a protection feature for the laser diode. A $DG303$ analog switch $IC20$ allows the discharge of the capacitors of the RC filter when the laser diode is turned off either by a fault condition or manually. Essentially, it resets the slow start-up circuit for the next slow start-up cycle. This results in a smooth current increase at start-up. $IC18$ is a $LM399$ precision, temperature-stabilized monolithic Zener diode with a temperature coefficient of $0.5\frac{ppm}{^oC}$. The current demand signal is therefore a voltage valued below the V_{set} supply voltage. The larger the current demand, the lower the signal becomes with respect to V_{set}. This signal is fed to $IC19$ connected as a constant current source through $Q4$ and $R60$. Effectively, the current demand signal is actively matched to the potential drop across $R60$ with respect to V_{set} by feedback action. $R59$ and $C59$ are added for loop stability.

The lower section of the laser diode branch consists of the current flow switch. This is built from two n-channel MOSFETS, $Q8$ and $Q9$. During normal operation, $Q8$ is in conduction and drives the laser diode. With the help of transistors $Q6$ and $Q7$ forming logical inverters, $Q8$ and $Q9$

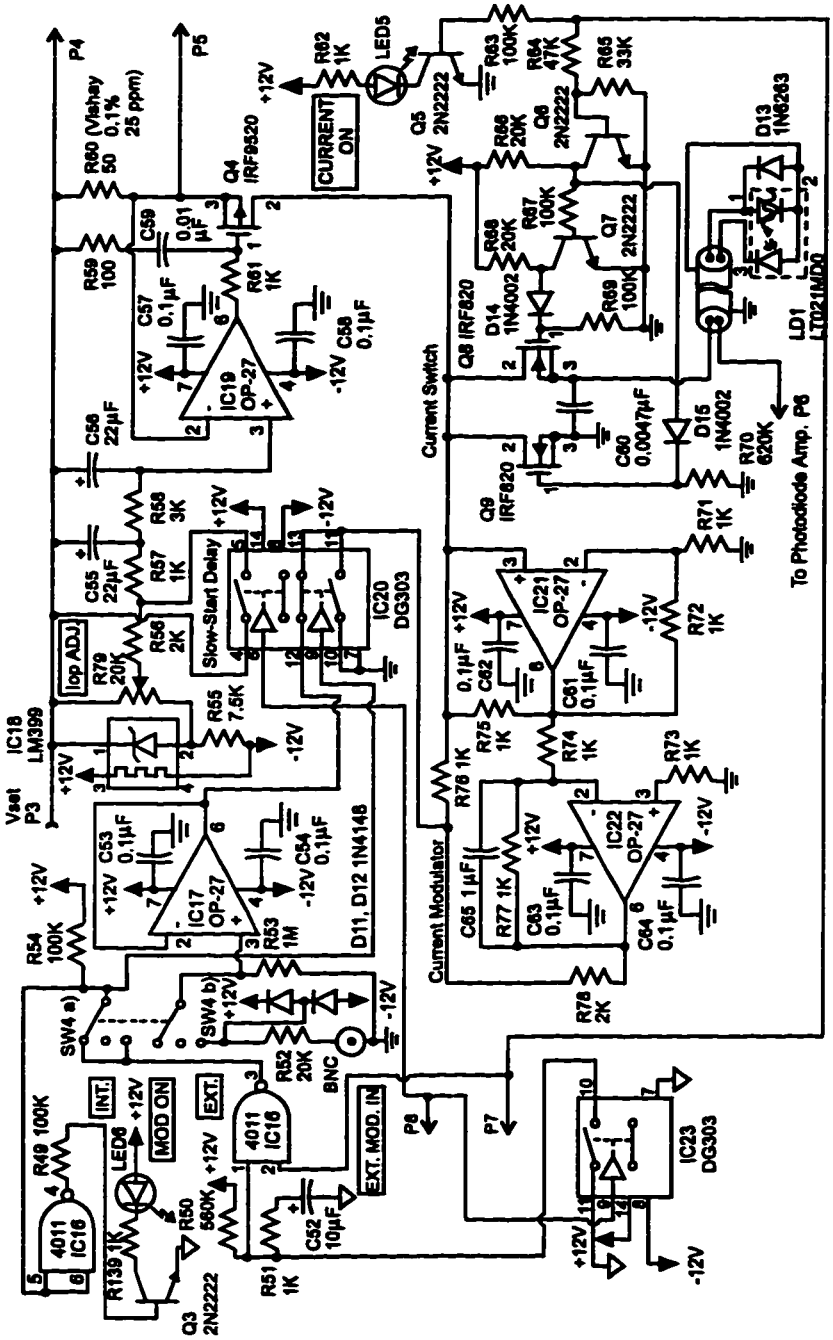

Figure 4.8: Laser diode controller circuit part B

are always in opposite logical states. When $Q8$ is on, $Q9$ is off and vice-versa. A logical signal will serve as an input to these inverters to allow enabling/disabling of the laser diode drive current. When $Q9$ is energized, it re-routes the drive current from the laser diode to a short circuit. This quickly shuts-off the current to the laser diode by essentially shorting it. However, keeping in mind that the top of the branch is effectively a constant current source which maintains a constant current in the branch regardless of the load, a potential problem arises during the switching transition between states. Effectively, in the middle of the switching cycle, $Q8$ and $Q9$ could potentially both be momentarily in the off state. When this happens, the constant current source will suddenly increase the supply voltage to saturation in an attempt to maintain a constant current across the resulting open circuit. When the switching cycle completes, before the constant current source has the time to bring back the supply voltage down as a result of the reestablishment of the circuit, a spike may result. The solution to this involves overlapping the switching states as to ensure that the situation where the two MOSFETS are off never happens. This is accomplished with the help of diodes $D14$, $D15$ and resistors $R69$ and $R70$. Effectively, this allows the MOSFETS to turn-on more quickly than they turn-off by taking into consideration the MOSFET gate capacitance. The charging of the gate capacitance occurs quickly with current flowing through the diode, but the discharge occurs by the capacitances discharging through the resistor, thus introducing an RC time constant in the turn-off cycle. Therefore, when the circuit starts in the short mode ($Q9$ energized, $Q8$ off), and switches in the laser diode enable mode ($Q8$ energized, $Q9$ off), $Q8$ turns-on very quickly while $Q9$ slowly-turns off. This results in the constant current source always "seeing" a load. A high-speed Schottky diode $D13$ is placed in parallel to the laser diode to protect against reverse polarity transients.

The next important circuit is the current modulation circuit. This circuit is formed by $IC21$ and $IC22$. The idea behind the circuit is based on the ability to add or remove a controlled amount of current from the preset operating current of the laser diode. This is normally performed by placing in parallel to the laser diode a circuit capable of injecting or subtracting current from the main branch which is being fed a stable bias current through the constant current source. Conventional laser diode modulation circuits will rely on direct connection through a series resistor of an external generator in parallel to the laser diode. Unfortunately, when a 0 V modulation input is applied, the laser diode is effectively shorted, or turned off. In practice however, this is undesirable as the modulation signal should effectively "rest" on the constant operating current which effectively biases the laser

diode in its linear region. A modulation signal should then vary the current slightly around this bias current within the linear region. To address this problem, a modulation circuit was configured as a double balanced circuit as in [58]. In essence, with this circuit, when $0V$ is applied at the modulation input located between resistors $R76$ and $R78$, no current is injected or drawn from the laser diode. The following explains this situation. The voltage U across the laser diode and the saturated MOSFET switch $Q8$ (pin 3 of $IC21$) is first amplified by a factor 2 by the non-inverting amplifier $IC21$. This signal then passes through the unity gain inverter $IC22$ to then drive the $2K$ resistor $R78$ connected to the modulation input. Since the other end of the resistor is grounded, the current through this resistor is given by $\frac{-2U}{2K}$. Moreover, it exactly cancels the current $\frac{U}{1K}$ coming through the $1K$ direct modulation resistor $R76$. To replace the current drawn from the laser diode branch flowing to this virtual ground, another $1K$ resistor $R75$ supplies a replacement current of $\frac{(2U-U)}{1K}$ from the output of the plus 2 gain stage. For a $0V$ input, the circuit then draws no current from the laser diode branch independently of the voltage drop across the branch. When a bipolar signal is applied, the circuit shown draws/adds current to the laser diode branch with a $-1\ \frac{mA}{V}$ gain regardless of the operating current or the voltage drop across the laser diode branch. The noise contribution for this added circuit is negligible.

As a protection measure, the modulation input signal is disconnected when the laser diode is disabled ($Q9$ ON, $Q8$ OFF). This is accomplished through the use of the $DG303$ analog switch $IC20$. This switch selects either the modulation input signal or the ground. During normal operation, when the laser diode is suddenly enabled, its drive current slowly increases due to the slow turn-on circuit. Only when the operation point current is reached should the external modulation signal be enabled. If this were not the case, a bipolar external modulation signal could damage the laser diode through reverse polarity when the laser diode bias current is at zero. The modulation enable timing is produced by an RC timer circuit formed by $R50$, $R51$, $C52$, $IC16$ and $IC23$. When the laser diode is suddenly enabled and its current is slowly ramping up, analog switch $IC23$ simultaneously opens and begin the RC timing sequence. The RC time constant is chosen to be larger than that of the slow-start current ramp up circuit as to ensure that the operating current of the laser diode has been reached before the modulation signal is enabled. When the RC timing circuit voltage exceeds the logic input threshold of NAND gate $IC16$, its output is turned on and enables the external modulation signal through the analog switch $IC20$. A manual switch $SW4$ also allows the modulation input to be disabled. The

modulation input port is a standard BNC connector. Diodes $D11$ and $D12$ and resistor $R52$ provide overvoltage protection for the input circuitry. $IC17$ is configured as a voltage follower and provides a high impedance input to the modulation circuit.

Figure 4.9 illustrates the overcurrent fault detection circuit. $IC25$ and $IC26$ form a high impedance differential amplifier circuit to monitor the voltage drop across the laser diode current-sensing precision resistor $R60$. This signal is compared with a maximum current setpoint adjusted through $R84$. Diodes $D16$ and $D17$, and resistor $R83$ provide a stable voltage reference for $R84$. $IC27$ is configured as a comparator circuit with hysterisis provided by $R89$. If the monitored current signal should exceed the current trip setpoint, transistor $Q11$ would become switched off. This logic signal would then trigger the flip-flop formed by $IC28$ and $LED7$ would indicate an overcurrent fault condition. $D18$ protects the transistor against reverse polarity breakdown due to the large voltage swings of the comparator. The fault signal would also immediately disable the laser diode by signalling to the laser diode current enable logic. The fault condition is therefore latched. This offers protection against both intermittent or continuous faults. $IC24$, a voltage follower drives an LCD digital voltmeter display module allowing the display of either the current trip setpoint or the monitored current as selected through switch $SW5$ and indicated by $LED8$ and $LED9$.

Figure 4.10 illustrated the undervoltage fault sensing circuits along with the laser diode current enable logic. $IC27$ is configured as a comparator. $R99$ allows the adjustment of the lowest positive voltage below which a fault condition is declared. This voltage level will vary with the positive supply rail voltage as $R99$ is setup in a voltage divider configuration. The comparator compares this voltage to a fixed reference supplied by Zener diode $ZN3$ and $R98$. The voltage drop across $ZN3$ will remain constant regardless of the supply voltage. When the supply voltage lowers the positive reference voltage below the Zener diode potential, the comparator turns off transistor $Q15$, and a fault condition is latched on the flip-flop formed by $IC32$. $LED10$ indicates the undervoltage condition. The $-12\ V$ circuit is similar, but opposite in polarity. In addition to being latched onto flip-flops, the undervoltage fault logic signals are also routed to the laser diode current enable logic circuit illustrated in the top part of the diagram. This circuit performs the function of turning off the laser diode circuit through the laser diode current switch as soon as any fault condition has occurred. The circuit has a latch such that intermittent as well as continuous faults may be detected and disable the laser diode. Pushbutton $SW6$ is depressed to enable the laser diode either at turn-on or following a fault condition. The current

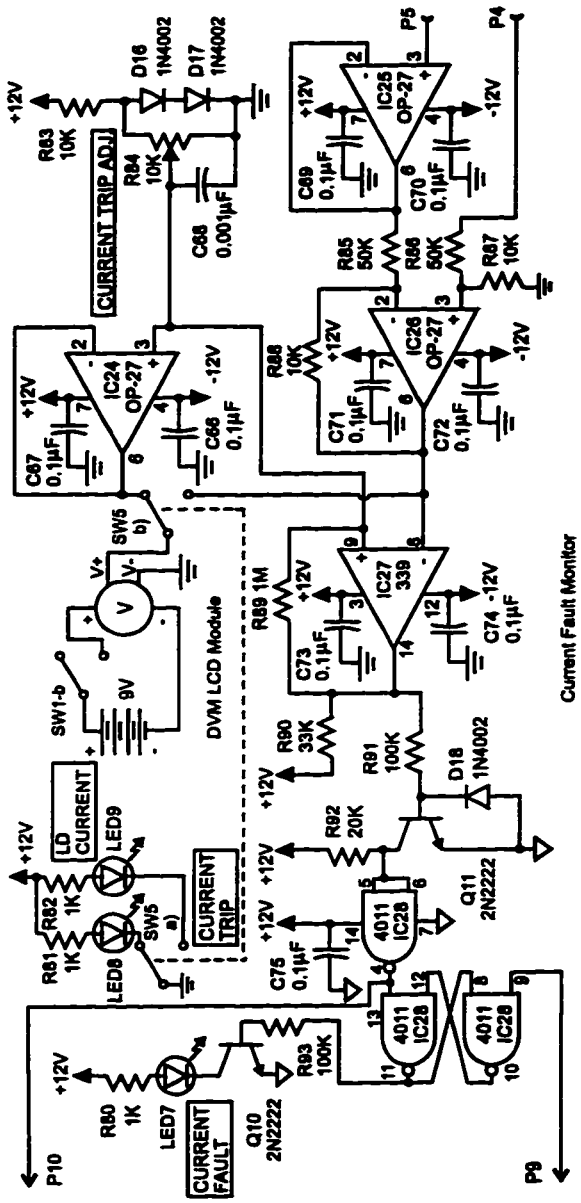

Figure 4.9: Laser diode controller circuit part C

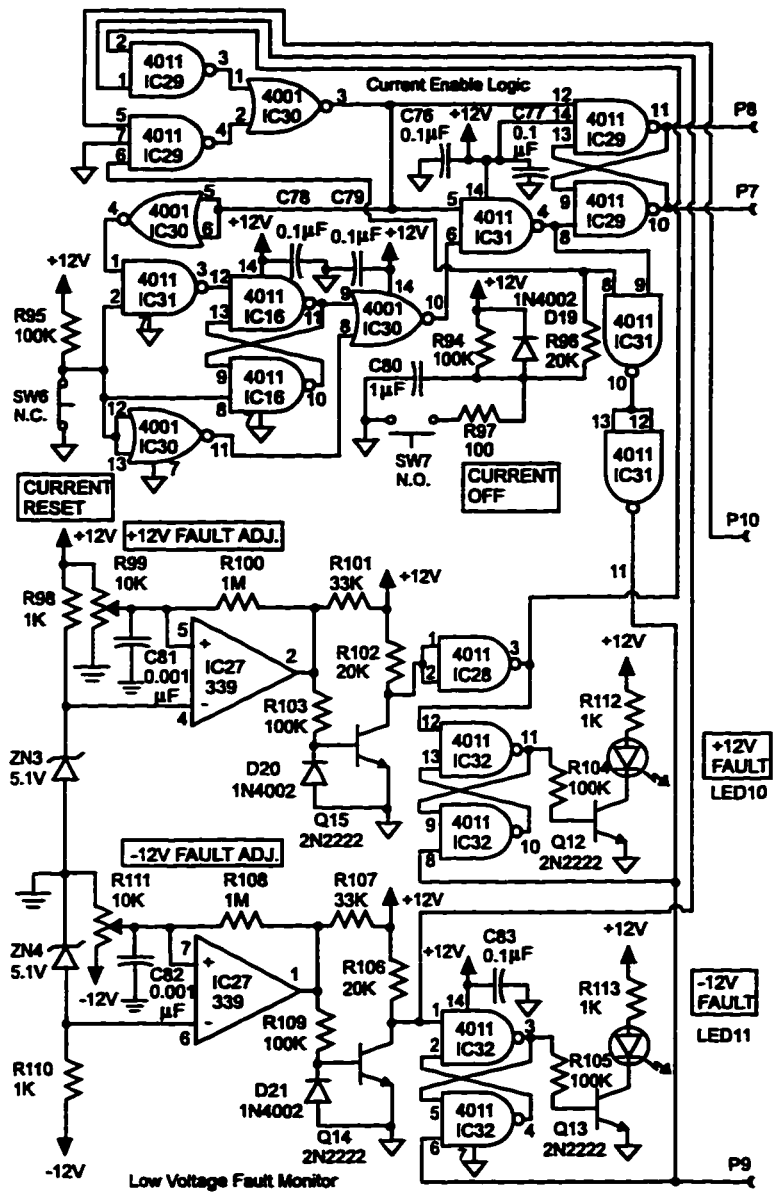

Figure 4.10: Laser diode controller circuit part D

enable logic will also prohibit the re-enabling of the laser diode current following a fault if the fault condition still exists. A manual emergency stop fault pushbutton is also provided by $SW7$ allowing the turn-off of the laser diode manually by the user. Note that a reset pulse is generated at circuit turn-on by $R94$, $D19$, $R97$, and $C80$ as to automatically generate a fault in order to ensure that the laser diode is initially turned off to avoid turn-on transient damage.

The circuit was constructed using wire-wrapping and soldering methods. Low-noise techniques were employed such as minimizing wire runs and using star grounding to all integrated circuits. Figure 4.11 shows a picture of the built prototype circuit.

4.5.2 Circuit Performance

The laser diode current controller circuit was tested over several hundreds of hours including continuous operation during 5 days. The original laser diode used in the design is still in use with no noticeable performance degradation. In some instances, the circuit was switched on and off several times per day. The laser diode transient and reverse voltage protection circuits seem adequate. The overcurrent trip circuit was tested manually by increasing the drive current setpoint beyond the current trip at which point the laser diode was automatically switched off. The undervoltage trip circuits were also tested by manually decreasing the supply voltage below the preset thresholds. Here again, the laser diode was automatically shut off when a fault was detected. The shut-off circuit, or MOSFET laser diode current switch was also extensively tested for fast and proper operation. Finally, the noise current generated by the constant current source was monitored. The voltage across the current-sensing 50 Ω high accuracy Vishay 0.1% tolerance resistor was observed through an oscilloscope. The current through the laser diode was set at a fixed level and the noise was observed through the AC-coupled oscilloscope signal. The noise amplitude was observed to be of approximately $\pm 1\ \mu A$.

4.6 Output Signal Conditioning Circuit

The internal monitor photodiode usually reserved for the purpose of laser output intensity regulation will instead be used for detecting the laser light power fluctuations induced through the self-mixing effect. Processing of the digitized power fluctuation signal will ultimately yield the desired range (and velocity) information. To this effect a circuit was designed to first

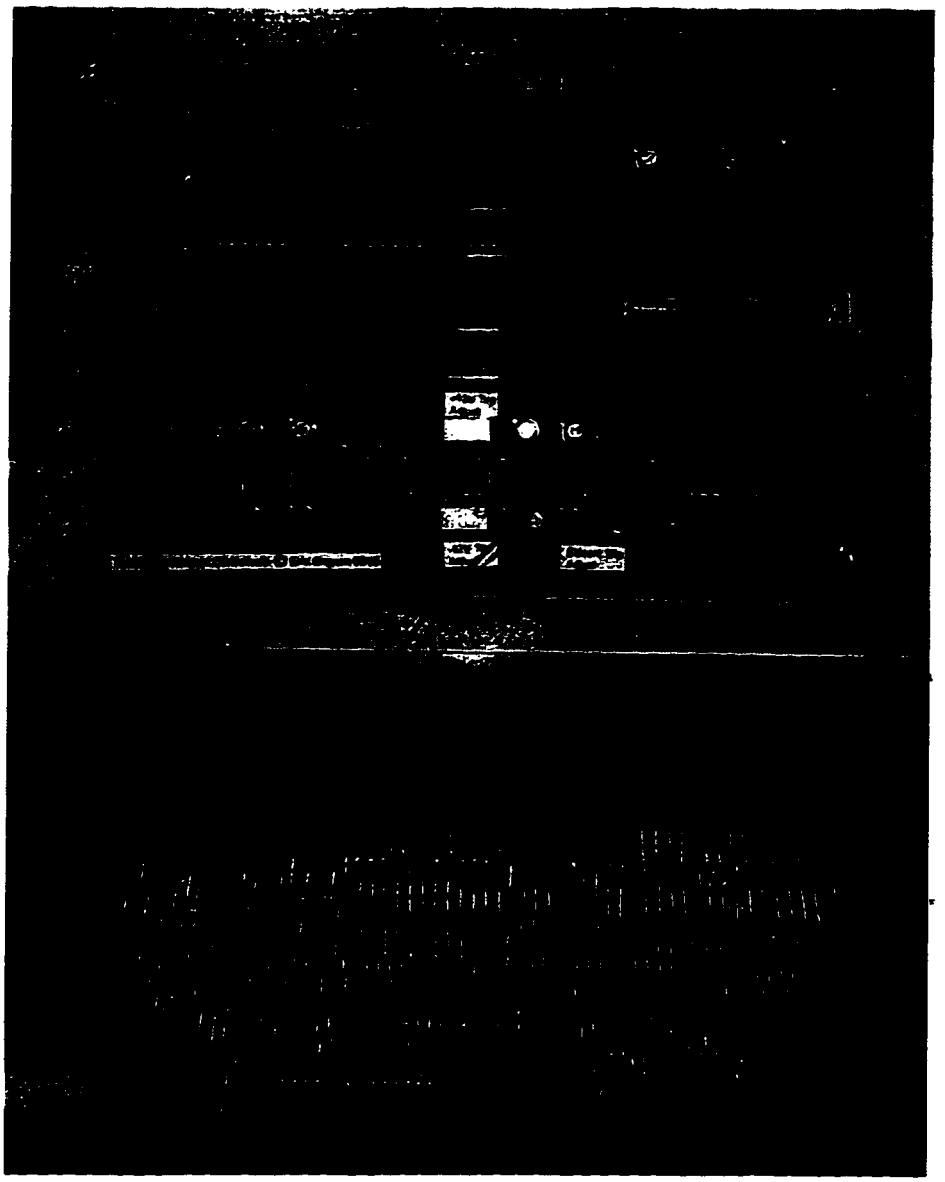

Figure 4.11: Picture of laser diode driver circuit (top). The underside also illustrates the wire-wrapping construction technique(bottom).

amplify the monitor photodiode signal, and then preprocess it before being output to the computer for digitization. Section 3.4 described how taking the derivative of the power fluctuation signal would greatly simplify the signal processing to be performed in order to determine the spacing between power fluctuation steps. This constitutes the basis of the preprocessing step. An output buffer has also been designed to allow low-noise coupling of the derivative signal to the analog acquisition card of the PC. The circuit eliminates potential ground loops problems.

4.6.1 Electrical Design

Figure 4.12 illustrates the photodiode signal conditioning circuit. Diodes $D22$ and $D23$ provide reverse polarity protection from the power supply. $IC33$ forms a transimpedance amplifier circuit used to amplify the current from the internal monitor photodiode of the laser diode. The photodiode current is proportional to the laser light output power impinging upon its surface. The transimpedance amplifier converts the photodiode current signal into a voltage signal proportional to the laser light output power. The gain of the amplifier may be set through potentiometer $R115$. At this stage, the output signal will consist of a signal with a DC and an AC component. The DC component is provided by the laser diode's fixed output light power bias, and the AC component, by the power modulation signal in superposition.

$IC34$ corresponds to the differentiator circuit. This circuit effectively generates the derivative of the photodiode power monitor signal, simplifying the eventual digital processing to be performed to recover range (and velocity) data. The differentiator circuit also eliminates the DC component, or bias, of the power monitor signal. This leaves the relevant AC component of the signal for processing. $IC35$ is configured as a high gain inverting amplifier for amplification of the AC component of the power monitor signal. An offset trim potentiometer $R121$ was added to allow trimming of the zero output level of the amplifier. This proved necessary due to the high gain of the last stage. Note that the capacitor and resistor values shown are valid for a 60 Hz modulating triangular wave (limited by maximum acquisition frequency of low-end PC A/D card). For higher frequencies, the capacitor values simply have to be adjusted accordingly.

Finally, the coupling of the output signal to any external device may prove problematic if careful attention has not been paid to the avoidance of ground loops. Ground loops are formed when several ground returns are provided to a given circuit. For example, the ground of a PC is usually

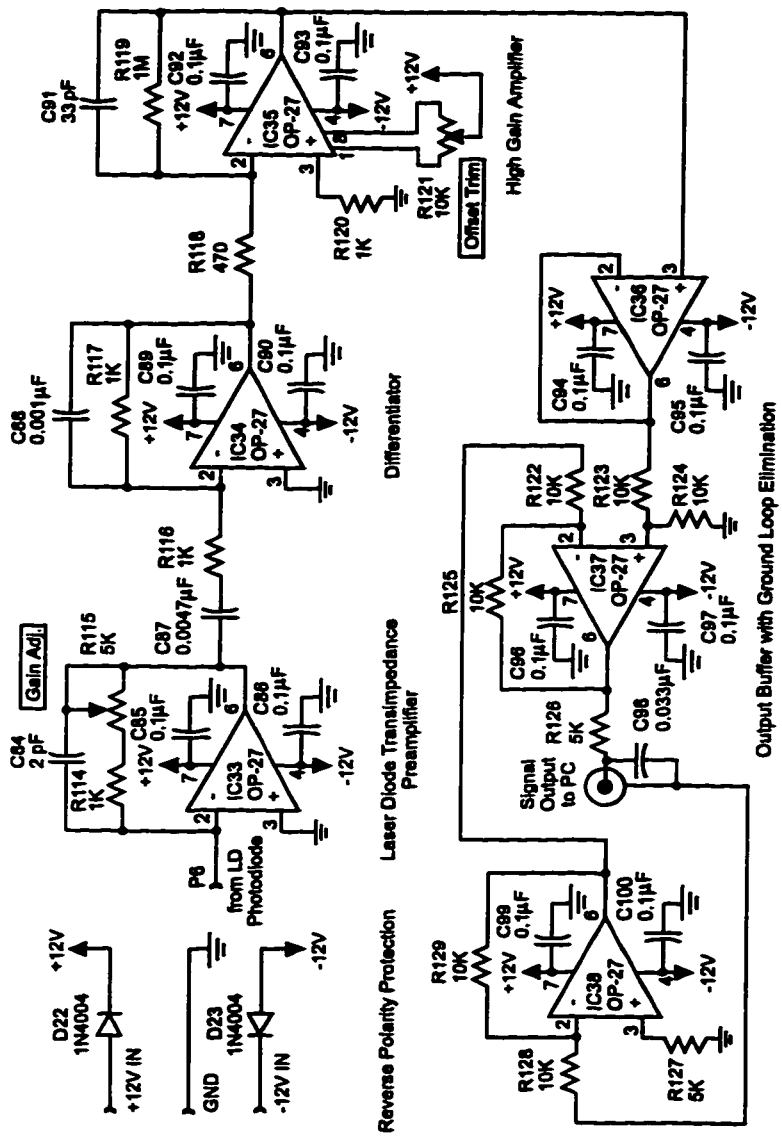

Figure 4.12: Signal conditioning circuit

connected to the outlet ground. In turn, the ground line of the analog acquisition card plugged into the PC will be grounded to this same outlet ground. The ground of the laser diode controller circuit will also be connected to the outlet ground through its grounded power supply. Theoretically all these grounds are at the same electrical potential. In practice, however, because the ground wires have finite resistance, the respective ground potential of each machine may differ slightly. Typically of the order of hundreds of millivolts for two machines plugged into the same grounded outlet, the potential mismatch is usually also very noisy. If the output of the laser controller circuit should be directly connected to the the acquisition card input through connection of the mutual signal and signal ground lines, a second ground path connection will thus be formed. The first ground path here is the indirect ground connection of the two devices through their outlet grounds. The potential differences between the two different ground connections cause a current flow through the connected signal ground lines. Because of the finite resistance of the signal grounding wires, this induces potential differences across the signal ground lines and results in dissimilar ground potentials. This effectively adds noise to the signal of interest which is being transferred between the laser diode controller and the PC through the transmission line. In the worst case, if large enough currents flow through the signal ground lines, physical damage may also result through overheating. To address the problem of connecting ground lines which may already be connected through alternate ground paths (i.e. outlet ground), one solution involves "floating" the measuring equipment, that is disconnecting the ground prong of the power cord. This way, a single ground connection will exist through the signal ground cables. For safety reasons, however, this is not recommended. Instead, a circuit has been designed to measure the ground potential of the signal ground line from the PC through a high impedance measurement circuit formed by $IC38$. This circuit is configured as a unity gain inverting amplifier. $R128$ and $R129$ have high enough values to ensure that no harmful current levels will flow from the PC's ground to the laser diode controller's ground if high enough potential differences should exist between the two grounds. The signal of interest (laser output power derivative signal) output from $IC35$ and buffered by $IC36$, a voltage follower, is then algebraically added to this measured ground noise voltage component with the help of $IC37$, a differential amplifier. The output signal of the circuit is therefore composed of the useful signal added to the measured ground noise. The data acquisition card will then receive the composite signal and will perform the data acquisition with respect to its "noisy" ground signal, effectively subtracting the added ground noise and recovering the unaffected

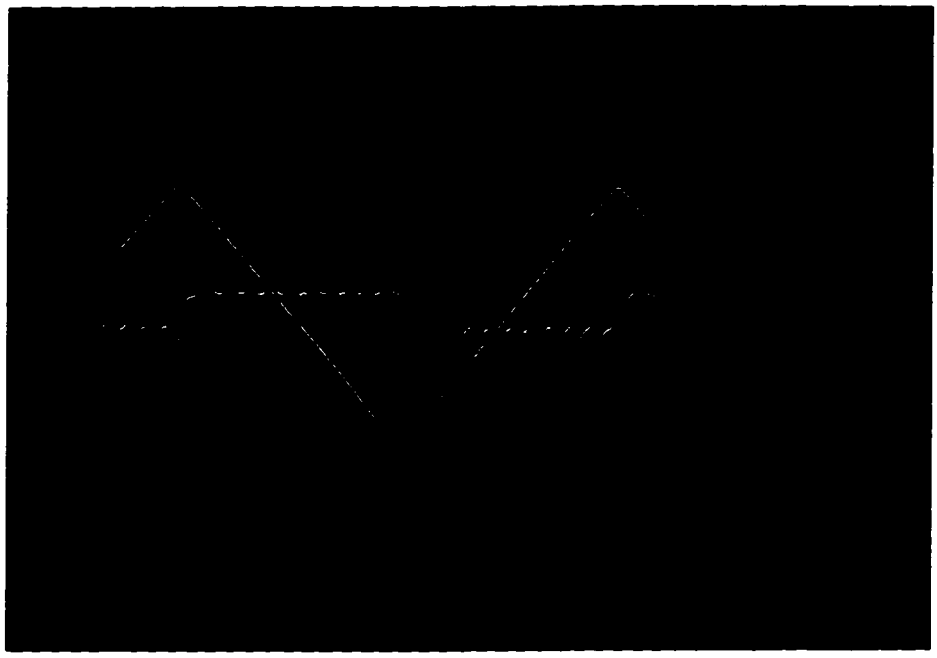

Figure 4.13: Oscilloscope picture showing output of signal conditioning circuit. The triangular signal is the modulating signal.

useful signal. The circuit was constructed using wire-wrapping and soldering methods. Low-noise techniques were employed such as minimizing wire runs and using star grounding to all integrated circuits.

4.6.2 Circuit Performance

The circuit was tested by aiming the laser beam from the laser diode at a fixed sheet of paper serving as a target. Figure 4.13 shows a picture of the oscilloscope displaying the output signal from the signal conditioning circuit. The triangular signal corresponds to the modulating signal input to the laser diode current controller circuit and has an inverted phase with respect to the current modulation signal. The superimposed "peak" signal is the derivative of the internal monitor photodiode signal with feedback. As can be observed from the picture, or more precisely from Figure 3.13, the derivative circuit effectively generates the derivative of the power fluctuation signal. The capacitor and resistor values for the differentiator circuit were adjusted as to yield the best derivative signal given the frequency of

the modulating triangular wave. The cutoff frequency of the differentiator and gain properties may be adjusted through $C87$, $C88$, $R116$, and $R117$. The ground loop elimination circuit was verified by injecting a small sinusoidal signal at the ground monitor input while sending a steady DC signal across the transmission line. The resulting output signal clearly showed the superposition of the two signals.

4.7 High Accuracy Digital Waveform Generator

As mentioned earlier, sensitivities of the final 1 DOF ranging unit to the triangular modulation wave frequency were of the order of 20 $\frac{mm}{Hz}$ error, a significant sensitivity figure. Because of this, a digital waveform generator circuit was designed. Using a high stability crystal oscillator, a waveform frequency stability of $\pm 0.1\%$ of the fixed oscillation frequency was achieved.

4.7.1 Electrical Design

The circuit design for the high-accuracy waveform generator is illustrated in Figures 4.14, 4.15, and 4.16. The circuit is based on a digital look-up table stored in an Erasable Programmable Read Only Memory (EPROM). The digital data stored at every memory address is read in sequence and then converted to an analog value through a digital-to-analog (D/A) converter integrated circuit. EPROMs usually are manufactured having output bus widths of 8-bits. In this design, 12-bit output accuracy was desired yielding 4096 possible discrete steps, so two 8-bit EPROMs were placed in parallel. The first EPROM thus provides the lower 8-bits and the second provides the higher 4-bits to form the final 12-bit data word.

Figure 4.14 shows the clock and sequencer circuit. $IC44$ is a 1.0 MHz crystal oscillator module. This provides the clock signal for the whole circuit. The clock signal is then fed to $IC39$, a counter used as a user-configurable clock divider. This allows the setting in four discrete increments of the final output frequency of the triangular signal through the jumper block. The resulting clock signal is fed through a cascade counter formed by $IC40$ to $IC43$. By ignoring the 3 most significant bits, this effectively forms a 13 bit free-running binary counter which increments its count every clock pulse and automatically recycles when an overflow occurs. The 13 bit bus is used as the address sequencer for the EPROM memories $IC45$ and $IC46$ shown in Figure 4.15. The EPROMs were programmed with an EPROM programmer in such a way as to provide a sequence of 12 bit data values in contiguous memory addresses by combination of the two side-by-side EPROMs. The

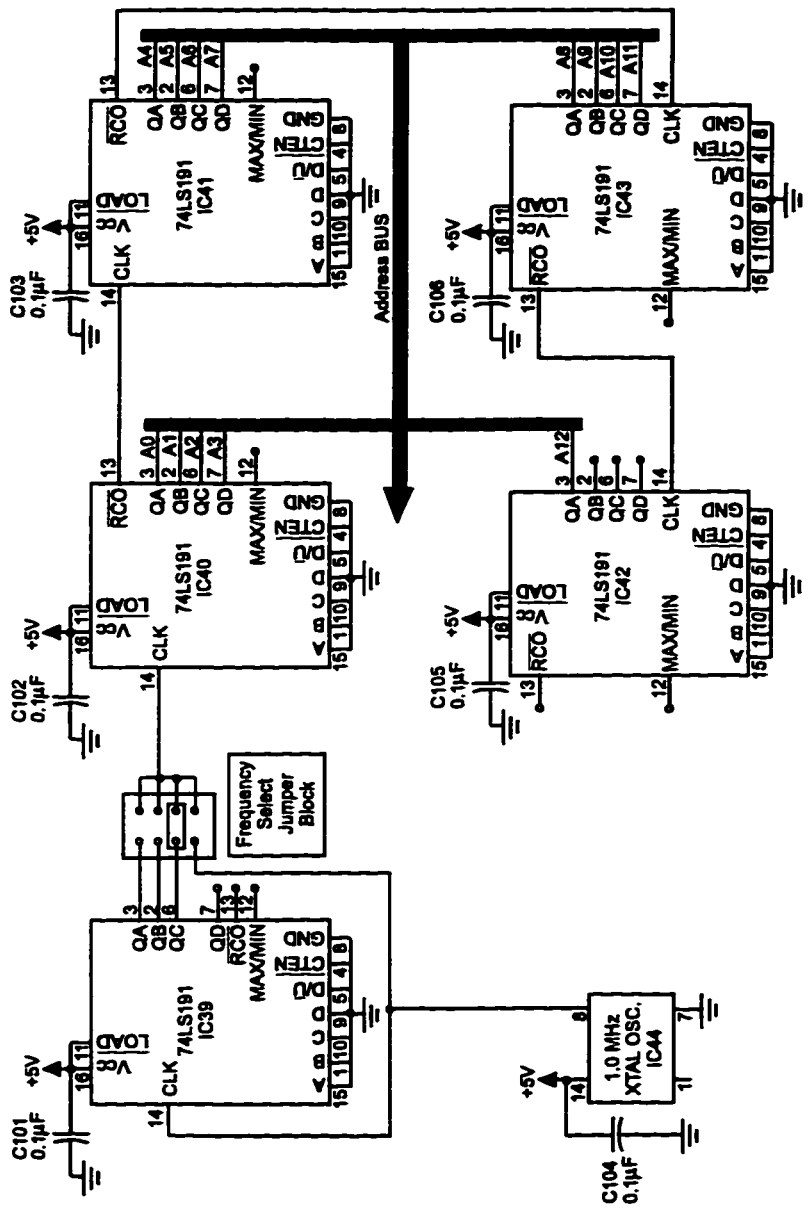

Figure 4.14: Digital waveform generator circuit part A

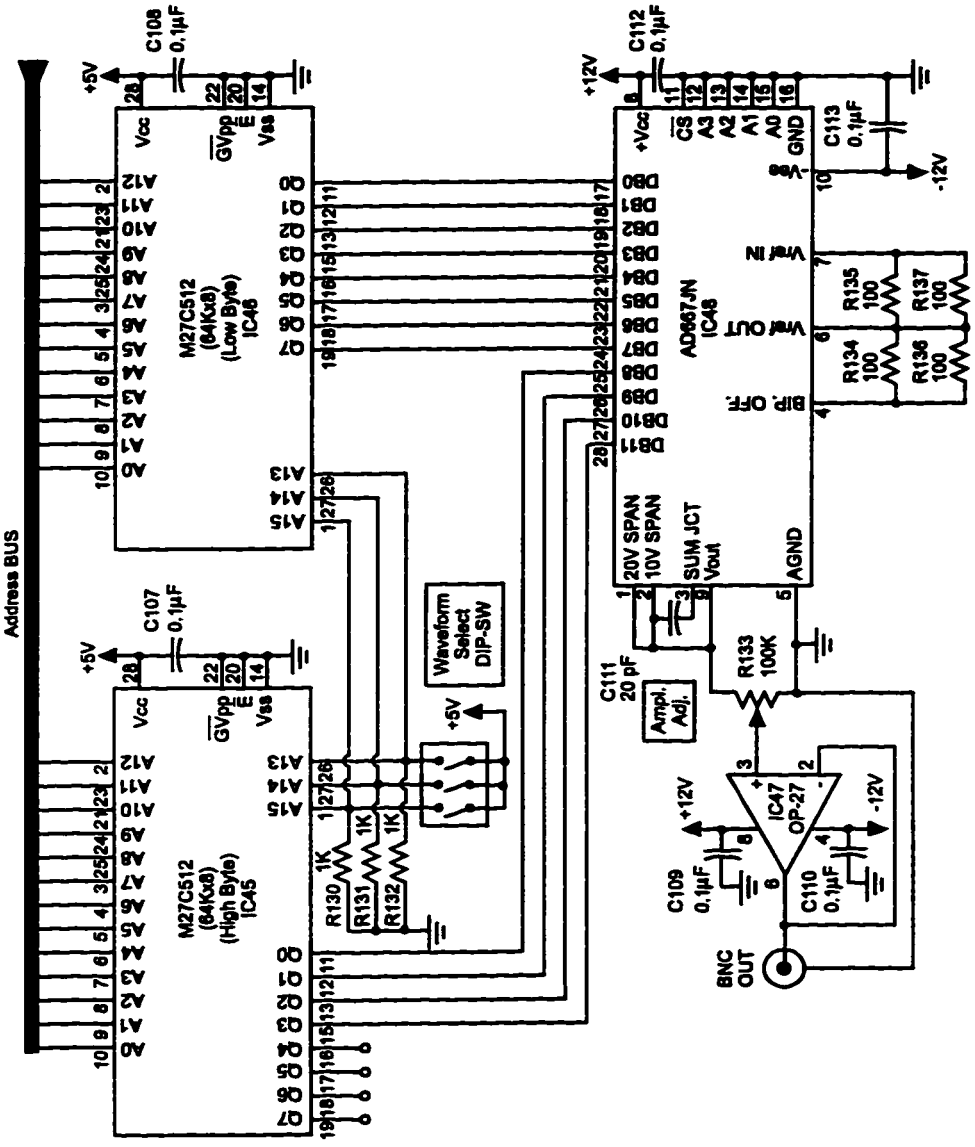

Figure 4.15: Digital waveform generator circuit part B

data was generated with the help of a custom-made computer program and written to a binary file. The binary file was then downloaded to the EPROM programmer and "burned" into the EPROMs. Along with the triangular wave profile data, sinusoidal, ramp and square wave profiles were also generated and stored at different start memory addresses. These start addresses are selected with the help of the DIP switches controlling the high-order address lines ($A13$-$A15$). Effectively, the type of wave is selected through the DIP switches. For the FM ranging circuit, however, a triangular signal will be used. The 12-bit digital data from the combined EPROM memories is then sent to $IC48$, a digital-to-analog converter which converts the digital values into corresponding analog values. $R133$ adjusts the amplitude of the output waveform which is then buffered by $IC47$, a voltage follower.

Figure 4.16 illustrates the power supply circuit for the digital waveform generator. This circuit consists of a standard power supply circuit. A center-tapped transformer $T1$ is rectified by the full-wave bridge rectifier $BR1$. Regulator $IC49$, a +12 V positive voltage regulator regulates the rectified and filtered voltage (through $C118$). Diode $D24$ is a protection diode in the event that the input to the regulator should become shorted, or at a lower potential than the +12 V side. In this case, the flowing current will be rerouted through the diode and not through the output of the regulator which could be damaged as it is only designed to source current, and not sink it. $IC50$ corresponds to the identical −12 V counterpart to the circuit. $LED12$ is the power indicator of the waveform generator. A +5 V supply is also derived from the +12 V through the use of $IC51$, a +5 V regulator.

4.7.2 Mechanical Design

The circuit was constructed using wire-wrapping and soldering methods. Low-noise techniques were employed such as minimizing wire runs and using star grounding to all integrated circuits. The digital oscillator circuit was mounted in a separate enclosure from the laser diode controller circuitry. It was designed as a self-contained device. Figure 4.17 shows a picture of the built digital waveform generator and enclosure. The wire-wrapped underside of the circuit is also shown along with the regulators and heat-sinks. A BNC output connector provides the signal output.

4.7.3 Circuit Performance

The waveforms generated by the circuit were compared against waveforms from a commercial off-the-shelf analog signal generator. The frequency sta-

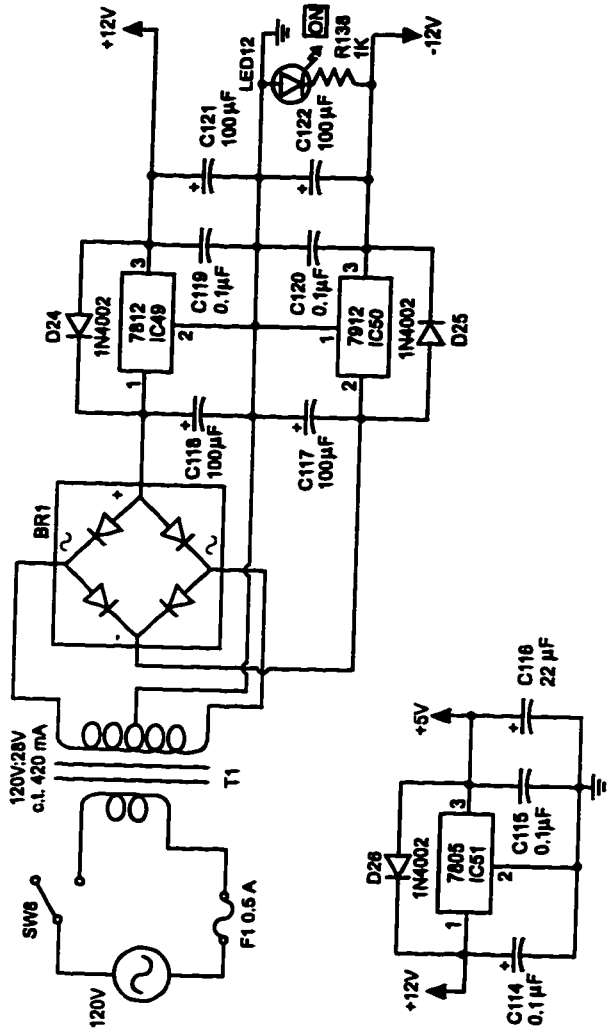

Figure 4.16: Digital waveform generator circuit part C

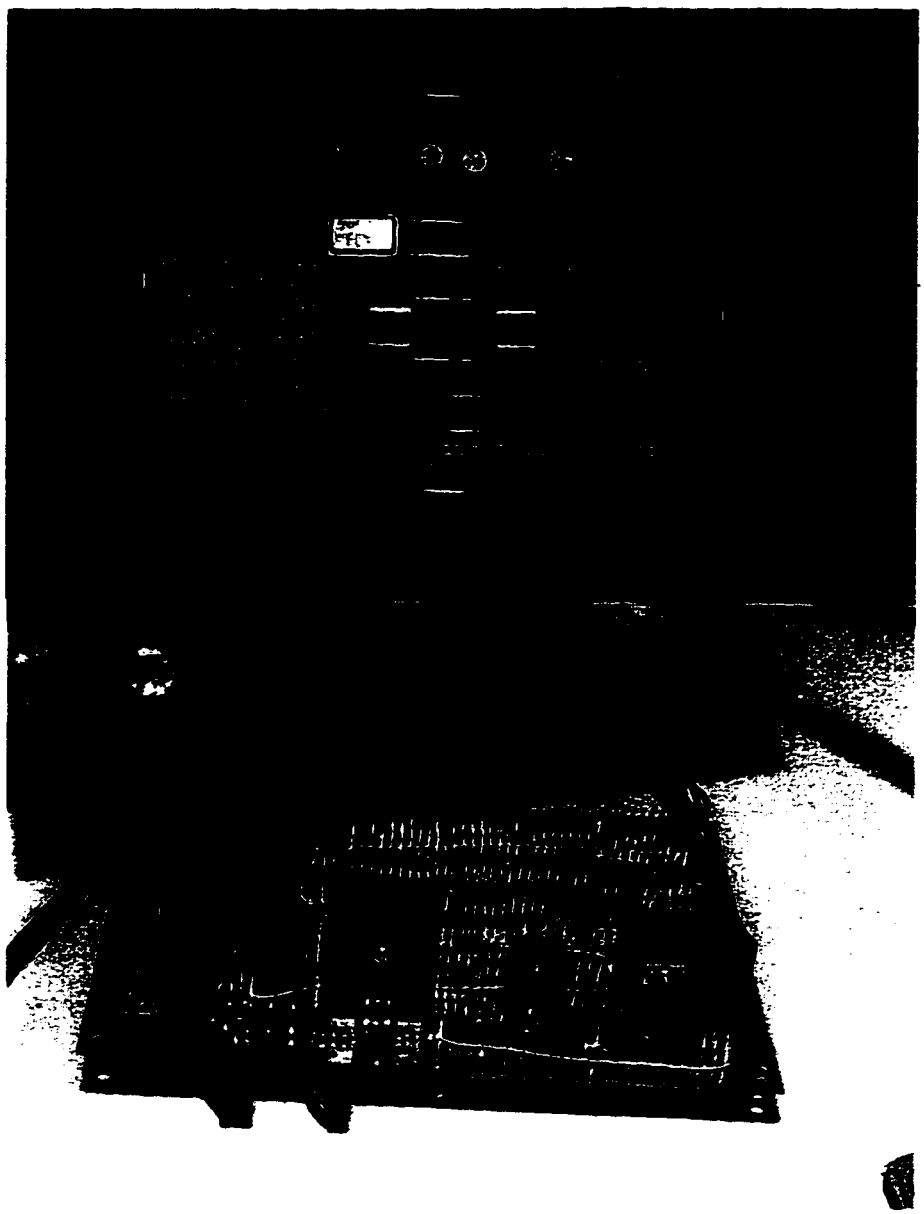

Figure 4.17: Picture of the built digital waveform generator and enclosure (top). The wire-wrapped underside of the circuit (bottom)

bility was far greater than what could be achieved with the analog unit. By locking the oscilloscope display to the digital wave and synchronizing to the analog unit, very rapid, random wandering of the relative phase and frequency were observed. The digital unit yields a frequency stability of $\pm 0.1\%$ of its selected oscillation frequency. Another marked improvement deals with the low harmonic distortion. Indeed, triangular signals in analog generators are often generated by passing a sinusoidal wave through a non-linear mapping diode network. This results in somewhat rounded peaks. With digital synthesis, near-perfect waves are generated. Even more conveniently, any arbitrarily shaped wave may be synthesized by simply reprogramming the EPROM data.

4.8 Complete 1 DOF Ranging System Prototype

The laser diode current controller, temperature controller and signal conditioning circuit were built and placed inside a clear plexiglass enclosure. A $\frac{3}{16}$ " thick plexiglass sheet was cut in appropriate pieces to form the box. Holes were drilled in the enclosure to allow mounting of hardware. Ventilation holes were made and a cooling fan was installed in order to evacuate the hot air from inside the enclosure. The inside of the plexiglass box was lined with a grounded metallic mesh providing electromagnetic interference (EMI) shielding and electrostatic discharge damage protection of the sensitive internal circuitry. Figure 4.18 shows a picture of the built laser diode controller and plexiglass enclosure. The three wire-wrapped circuits were stacked with the help of vertical copper rods. The top board is the temperature controller, the middle one is the laser diode current controller, and the bottom one, the signal conditioning circuit. Figure 4.19 shows a picture of the front of the prototype. The instrumentation panel is displayed along with the LCD digital panel meter monitoring the bias current setpoint of the laser diode, in milliamperes. The laser diode case temperature may also be displayed in degrees Celcius through a selection switch. The color label on the instrumentation panel was generated with a color inkjet printer and laminated with clear adhesive tape. The BNC modulation input connector is shown. Attached to the right of the unit is the stand-along digital waveform generator box prototype described previously. At the top right on the enclosure, a plastic wire harness carries all the wires going to the laser head unit. This unit is composed of the laser diode mounted in a heat sink along with the Peltier Junction used for temperature regulation as described in section 4.4.2. The laser head unit and plexiglass enclosure is illustrated

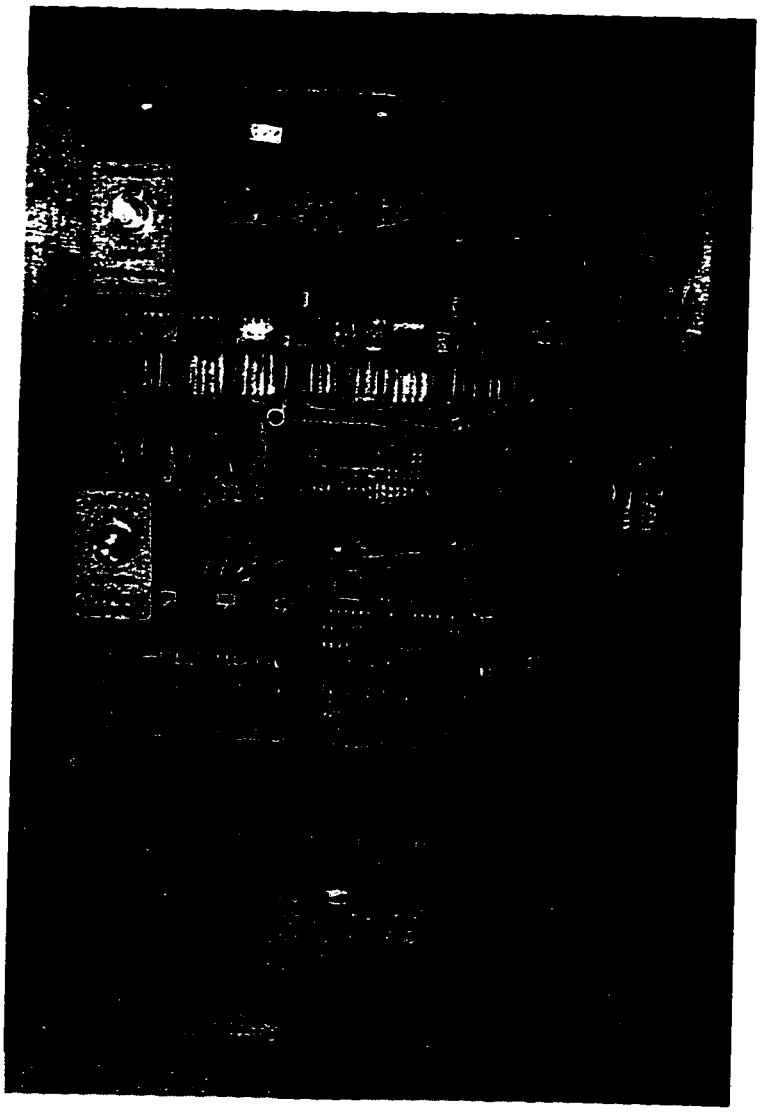

Figure 4.18: Picture of the built laser diode controller and plexiglass enclosure. The top board is temperature controller, the middle one is the laser diode current controller, and the bottom one, the signal conditioning circuit.

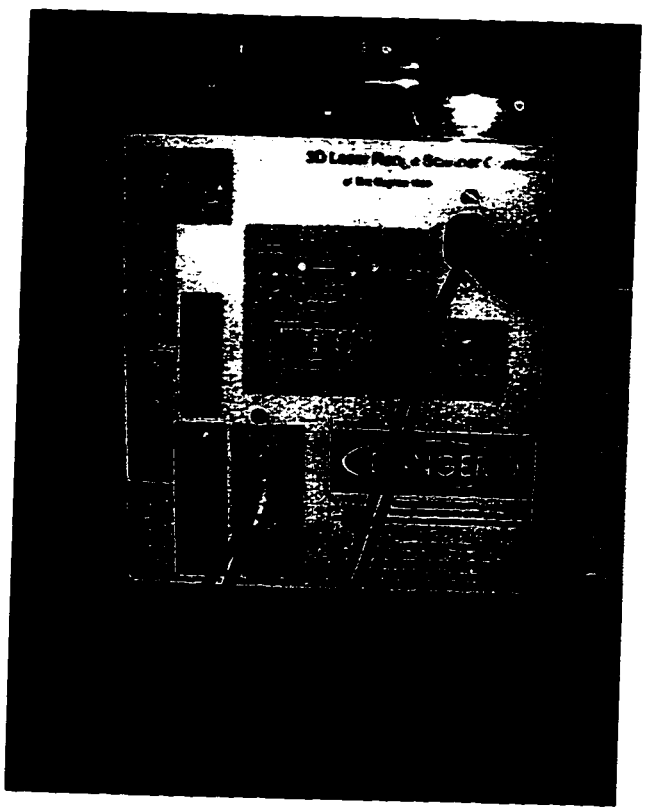

Figure 4.19: Front view of the laser diode controller prototype.

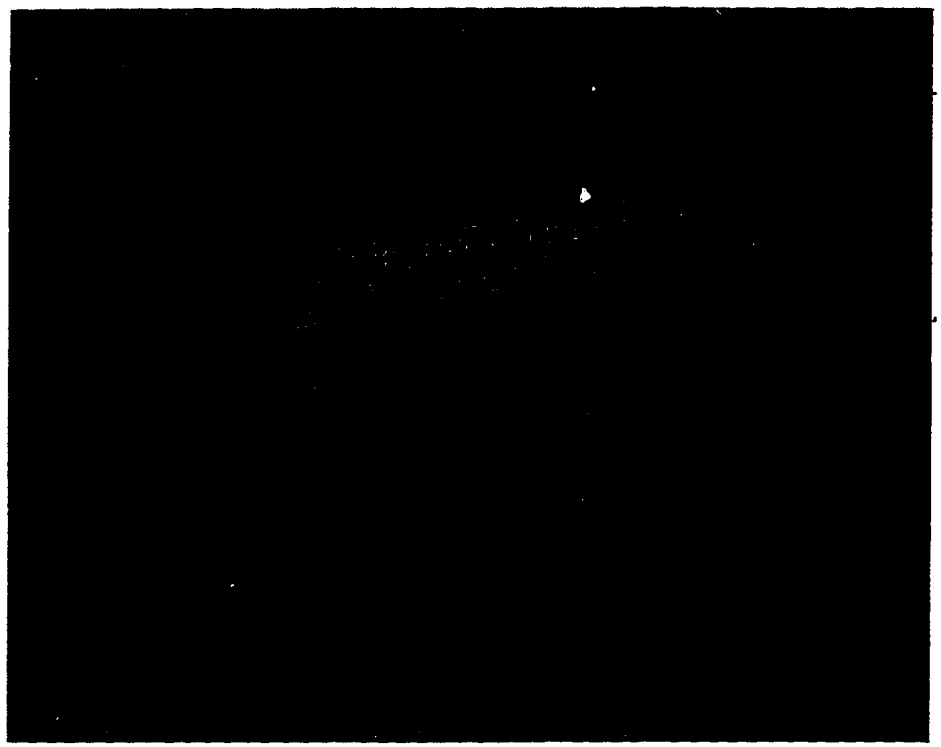

Figure 4.20: Laser head unit with enclosure

in Figure 4.20. Ventilation holes were placed all around the enclosure and grounded metallic mesh was used to line the interior walls. The laser beam exits from the front opening of the laser head. A standard $\frac{1}{4}$" threaded base mounting hole was made under the laser head unit to allow mounting on a tripod. Finally, Figure 4.21 shows the complete 1 DOF laser ranging system prototype.

4.9 Peak Detection Algorithm

A new algorithm was developed to process the signal output from the 1 DOF ranging unit and compute the corresponding range and velocity of a target. The algorithm was incorporated in a control software developed in C++ on a PC. The software is responsible for the control of the data acquisition card, for the processing of the digitized ranging signal from the laser ranging system, and for the displaying of the signal.

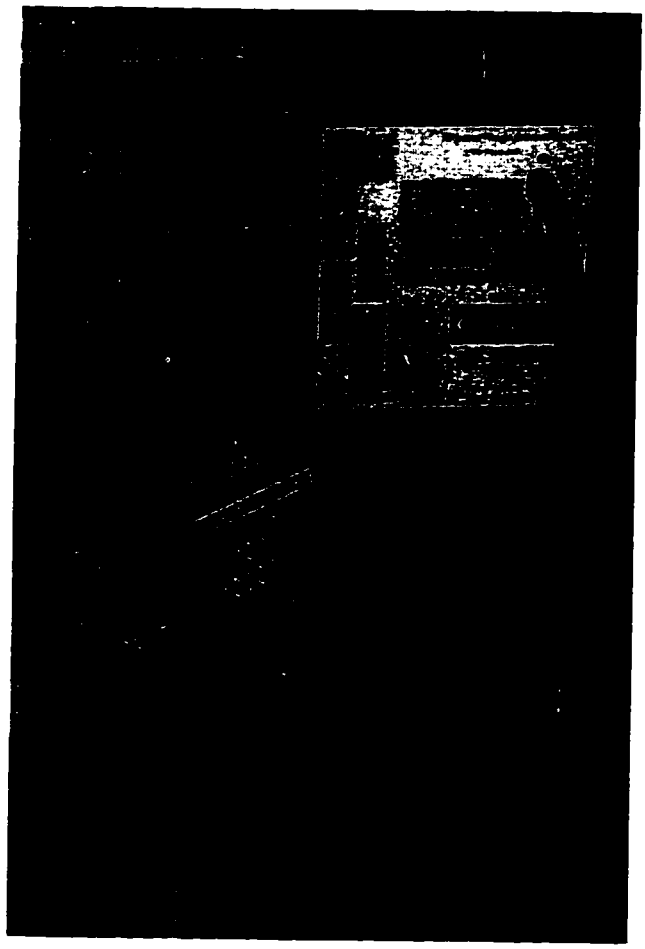

Figure 4.21: 1 DOF laser ranging system prototype

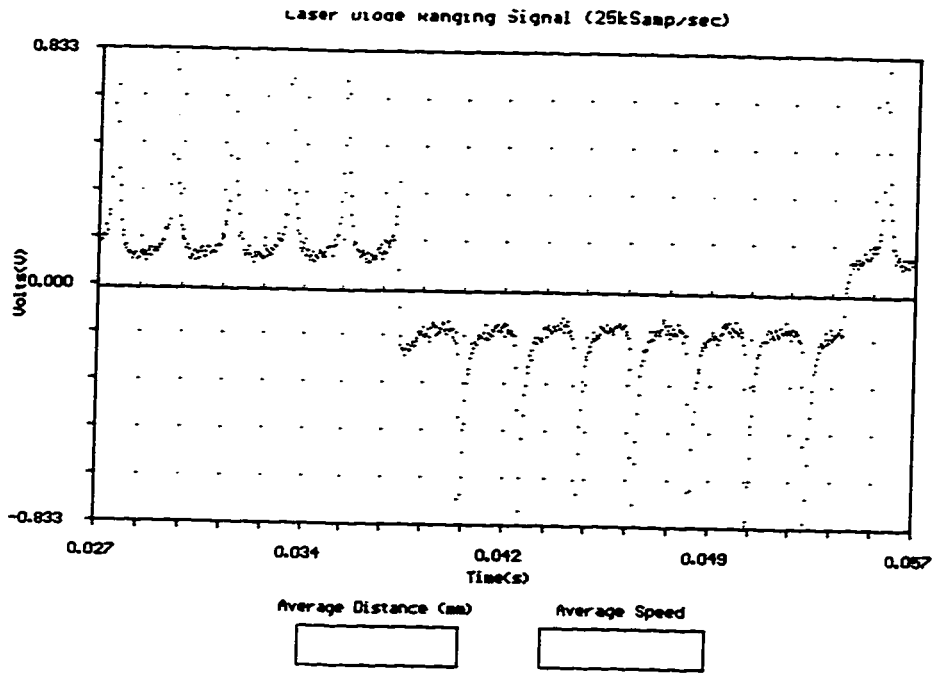

Figure 4.22: Screen capture of PC software showing digitized 1 DOF laser ranger signal.

Figure 4.22 is a screen capture of the main screen of the designed PC control software. A 0.1 s duration burst sample of the ranging signal has been acquired at a sampling rate of 25 kHz. The figure shows a zoomed portion of the acquired waveform covering one period, or 0.03 s (30 Hz modulating wave). The acquisition resolution is of 12 bits. The acquired signal is graphically displayed on a grid. As may be observed, the signal is composed of a sequence of alternating positive and negative "plateaus" of peaks with respect to the average of the signal computed and displayed as the horizontal reference line. It is desired to estimate the average spacing between all the contiguous positive peaks of all the positive plateaus and between all the contiguous negative peaks of all the negative plateaus. For straight ranging purposes, the positive and negative peak spacing may be combined, simplifying the computation. However, if velocity information is

also desired, discrimination between the two is necessary. The principle behind the technique developed for automatic average peak spacing detection is described in three steps. The first step involves the segmentation of the signal into positive and negative plateaus. In the second step, the peak detection and peak spacing estimation is performed on the segmented positive and negative plateau sections respectively. Finally, the third step consists of the mapping of the computed positive and negative peak average spacing into range and velocity measurements. Figure 4.23 is a diagram describing the technique.

4.9.1 Signal Filtering

The first processing step involves filtering of the noisy input signal. Two computationally simple filtering approaches were tried in order to yield a relatively clean and smooth signal. Median filtering, typically very good at eliminating small noisy "spikes" was first tried. The filtered signals often featured a large number of small discontinuous steps for which neighboring values were identical. Unfortunately, this result is undesirable as the derivative of this filtered signal will yield a large number of unnecessary zero-crossings which will have an adverse effect on the following peak spacing detection algorithm. For this reason, straightforward sliding window averaging of the signal was chosen over median filtering. Sliding window averaging yields a nice rounded continuous signal and tends to fill gaps. The size of the sliding window was determined experimentally as to yield an arbitrarily smooth signal. The parameter is user-selectable. It was found that by repeating the filtering operation a number of times, the filtering results were also improved. Here again, the number of filter passes were determined and set experimentally. Note that in repeating the sliding average filter operation a very large number of times, the resulting filter's unit sample response approaches the shape of a Gaussian distribution. Nonetheless, the filtering computation time increases with increased filter size and iterations, so time constraints may ultimately restrict the possible acceptable filtering characteristics. In practice, for the 1 DOF ranging system, a window size of 5 samples was selected while $1-2$ filter passes were performed.

4.9.2 Signal Segmentation

As may be observed from 4.22, the digitized ranging signal is composed of repetitive elevated "plateaus" of positive and negative peaks with respect to the signal average indicated by the reference horizontal line. The char-

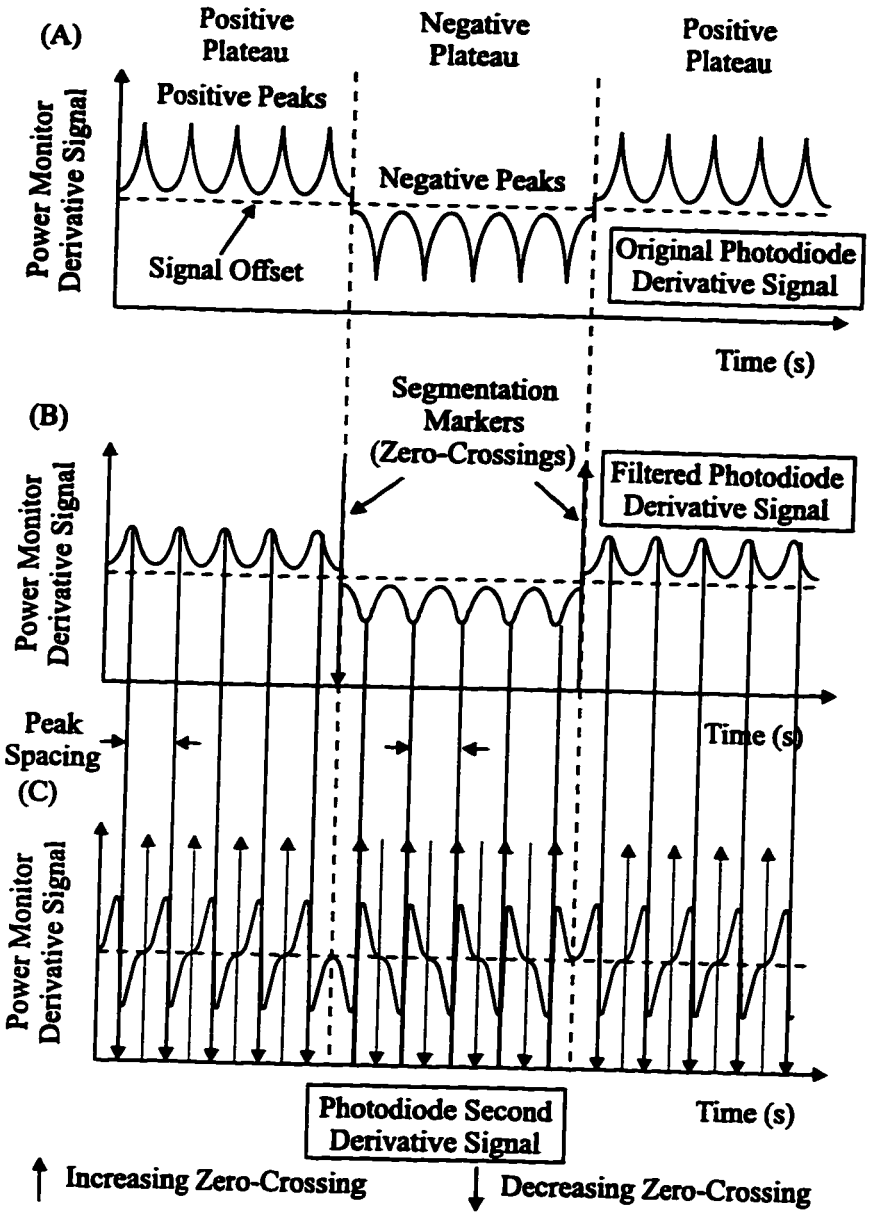

Figure 4.23: Diagram of the peak detection algorithm. (A) The signal offset is computed as a reference. (B) The signal is filtered and segmented. (C) The first derivative signal is computed and used to obtain the peak coordinates for positive and negative plateaus. Peak spacing is then obtained. Pruning and error checking is also performed to eliminate corrupt values.

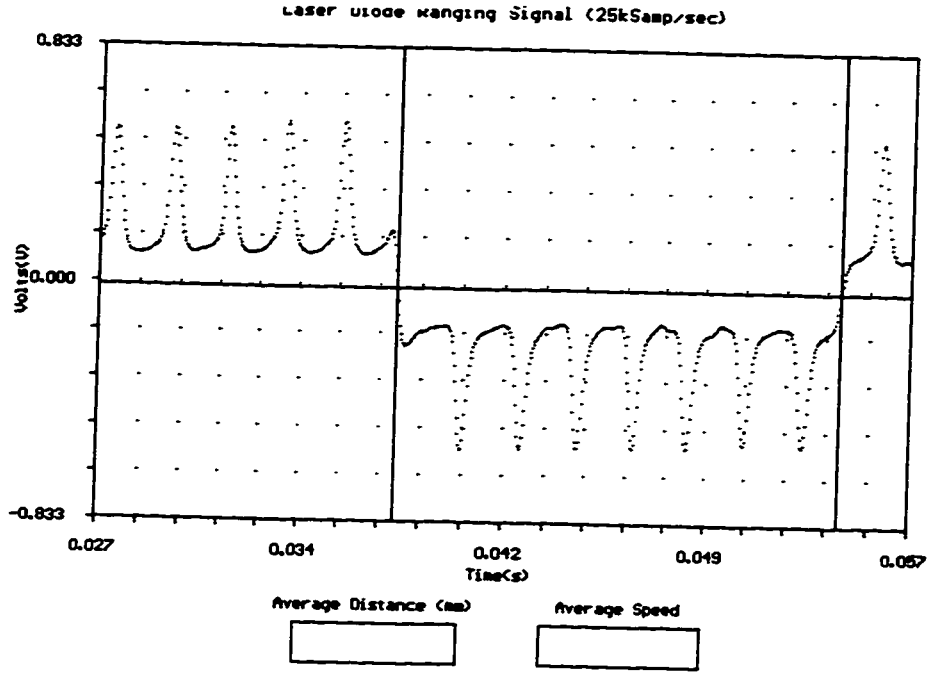

Figure 4.24: Screen capture of PC sofware showing filtered signal and first zero crossing detection for signal segmentation.

acteristics of the plateaus are set by the output signal conditioning circuit cutoff frequency and gain response (see section 4.6). A zero-crossing algorithm with directional discrimination was devised and implemented. The algorithm allows for linear subsample interpolation of the zero-crossing coordinate. It also detects whether the zero-crossing is a result of a transition from a negative value to a positive value or vice-versa. Both these specifications are needed for the segmentation. Figure 4.24 shows a screen capture of the filtered digitized signal along with vertical line markers indicating identified zero crossings by the detection algorithm. The location of the zero-crossing markers is computed with subsample interpolation accuracy. Note that the directional information of the zero-crossings is not shown on the figure, but is identified by the zero-crossing algorithm. A marker denoting a zero-crossing from a negative to a positive value will be referred to as an in-

creasing marker and the converse as a decreasing marker. At this stage, the zero-crossing markers serve to delimit the positive and negative plateaus for segmentation. A positive plateau within the signal will be bracketed by two consecutive markers, the first being an increasing marker, and the second, a decreasing marker. Correspondingly, a negative plateau will be bracketed by a decreasing marker followed by an increasing marker. If excessive noise causes the appearance of consecutive markers of the same direction, they are simply ignored, and the algorithm moves to the next potential candidates. Once the signal has been divided into multiple subsections respectively classified as being either a positive or a negative plateau, local peak detection is then performed within each plateau.

4.9.3 Peak Detection

In order to detect the center of the peaks forming a positive plateau, the derivative is taken. The zero crossings of the signal are then found and the coordinate of the center of the positive peaks will be given by the "decreasing" markers[1]. Correspondingly, for negative plateaus, the "increasing" markers will identify the location of the negative peak centers. Note that the operation performed is that of the identification of local maxima with downward concavity in positive plateaus and of local minima with upward concavity in negative plateaus. Figure 4.25 shows the identified markers of the derivative signal. Note that the markers in the figure are identified for the whole signal. Keep in mind that segmentation information from the previous figure (4.24) is used to differentiate the groups in which each marker belongs. For each positive plateau boundaries detected by the segmentation, all the enclosed markers are considered. From the first leftmost marker in a group, a running sequence of mutually opposite markers is seeked. For example, if the first marker in the segmented positive plateau is a decreasing marker, then the next two are verified as being respectively increasing and decreasing. If so, the signal is assumed not to be corrupt and the spacing between the two decreasing markers is taken as the first detected positive peak spacing. This values is added to a variable which keeps a running sum of all measured positive peak spacings of all the positive plateaus of the digitized signal. At the end of the computation, an average of the spacing measurement will be computed by dividing the value of the running sum variable by the number of detected positive peak spacings. If a sequence of non-alternating markers is identified, corruption of the signal is assumed.

[1]The increasing markers in a positive plateau will indicate the location of the minima (depressions) between the peaks.

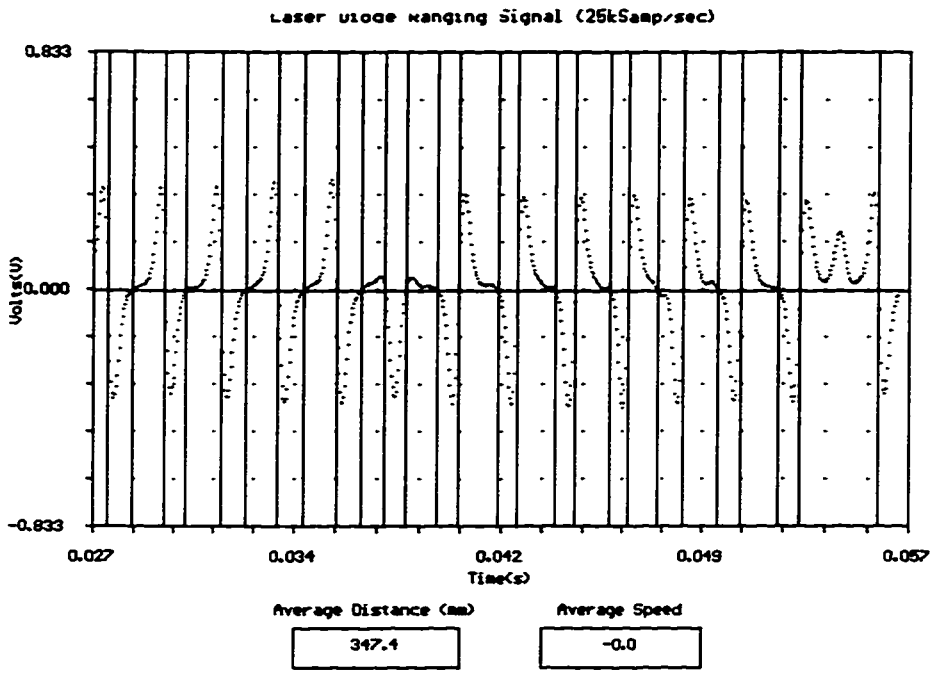

Figure 4.25: Screen capture of PC software showing derivative of acquired signal, filtering and second zero crossing detection for peak spacing estimation.

The algorithm then ignores the first marker and tries again with the second, third and the next marker. If again invalid, the algorithm moves on, and so on until the end of the plateau is reached. At the end, an average spacing value is computed for all positive peaks of all the positive plateaus. The same is done for the average spacing for all negative peaks of all the negative plateaus.

4.9.4 Median Pruning

Due to noise corruption, noise-induced markers may distort the measurements of the average peak spacing. Because of this, a "pruning" technique was devised to throw away suspicious values. In essence, for each plateau, all the peak spacings are computed. The median value of all the measured spacings is computed and used as a selection criterion. Each peak spacing value which differs by more than a user-specified percentage (typically 10%) of the median value is discarded.

4.9.5 Range and Velocity Determination

Once an average value for the positive peak and negative peak spacing is obtained, a mapping must be performed to obtain the desired range and velocity information. As described in section 3.4, the range information is computed by averaging the positive and negative peak spacing, thus measuring ν_0. The target range is proportional to the wavelength, the inverse of this quantity ($\lambda_0 = \frac{c}{\nu_0}$). Through calibration of the device at measured target positions, the slope and offset constants describing the linear relationship are determined. The range information is then computed by:

$$\text{Range} = \frac{\left(\frac{\overline{\text{spacing}_{pos.peak}} + \overline{\text{spacing}_{neg.peak}}}{2}\right)^{-1} - b_{range}}{m_{range}} \tag{4.1}$$

The overline indicates an average measurement. Since a triangular current modulation signal is used, the peak spacing expressed in seconds is proportional to the laser diode frequency excursion of the output laser light of the laser diode in Hz. Because of this, the spacing shall be directly expressed in Hz from now on. m_{range} is the calibration slope in $(\frac{Hz}{mm})$, and b_{range} is the offset in (Hz).

The velocity of the target is computed by taking the difference in the average negative peak spacing and positive peak spacing. The velocity of

the target is proportional to this quantity. Here again, through calibration, the slope and offset of the linear relationship will be determined to yield:

$$\text{Velocity} = \frac{(\overline{\text{spacing}_{neg.peak}} - \overline{\text{spacing}_{pos.peak}}) - b_{velocity}}{m_{velocity}} \tag{4.2}$$

$m_{velocity}$ is the calibration slope in $(\text{Hz}/\frac{mm}{s})$, and $b_{velocity}$ is the offset in (Hz). The overline indicates an average measurement.

Chapter 5

X-Y Laser Range Scanner

5.1 X-Y Galvanometers

An X-Y laser range scanner was designed and built by combining the 1 DOF laser ranger with an X-Y galvanometer beam steering unit. Figure 5.1 illustrates the setup. The laser head unit is mounted on an optical table as to emit a laser beam towards the beam steering unit built from off-the-shelf galvanometers. After being deflected by the galvanometer mirrors, the laser beam is projected towards a target to be imaged. The target as shown in the picture is a normal sheet of paper. Different objects are placed in front of the laser scanner in order to be imaged. Figure 5.2 shows a close up view of the galvanometers and the laser head unit. The first X galvanometer mirror rotates around the vertical axis providing lateral deflection of the laser beam. The small, low-inertia mirror allows for fast lateral sweeping of the laser beam into the optical axis of the second Y galvanometer mirror. This second galvanometer rotates around the horizontal axis providing vertical deflection of the beam. Since this second mirror is bulkier, the Y galvanometer usually moves slower than the X galvanometer and is chosen to sweep the line generated by the X galvanometer vertically.

5.2 Galvanometer Control

The galvanometers are driven by closed-loop galvanometer amplifiers. Their respective drive signals are generated through the D/A output of the PC data acquisition card. A control program was designed to scan the scene with the laser beam in a raster scan fashion while sampling range points on a regular grid.

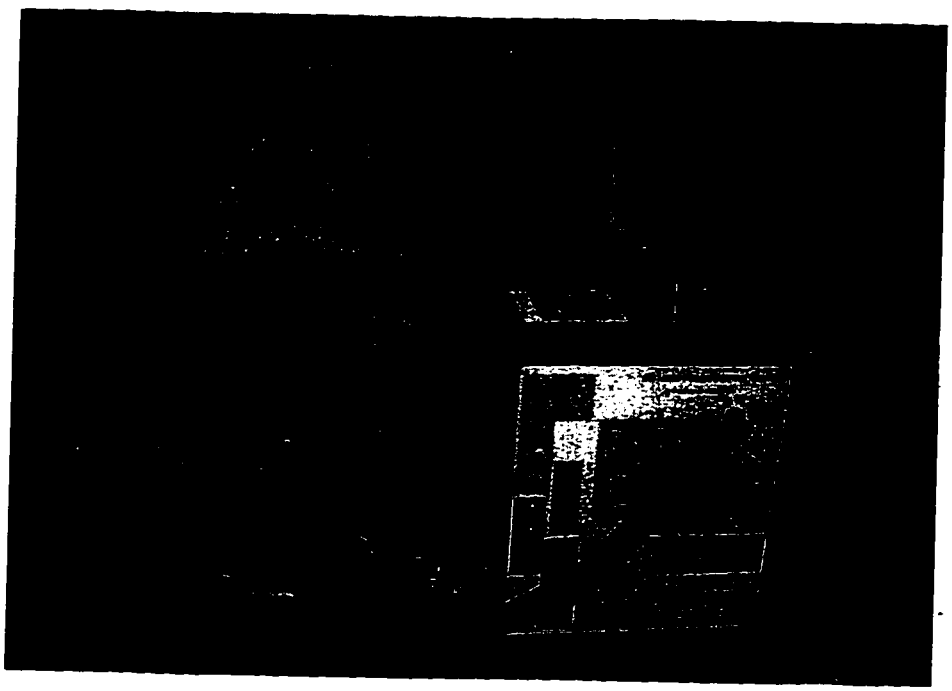

Figure 5.1: Complete laser range scanner setup

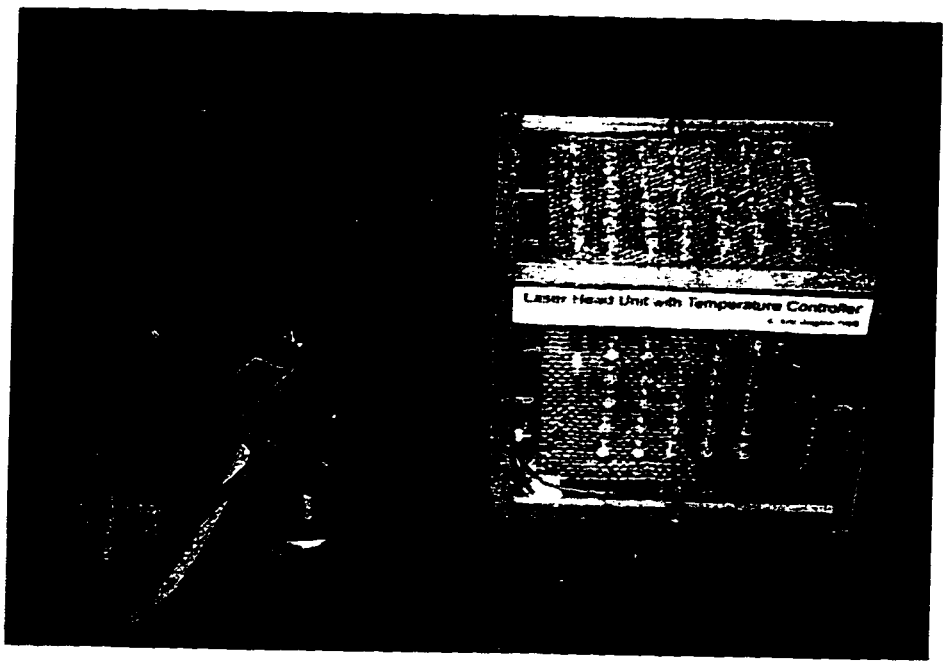

Figure 5.2: X-Y galvanometer beam steering unit setup

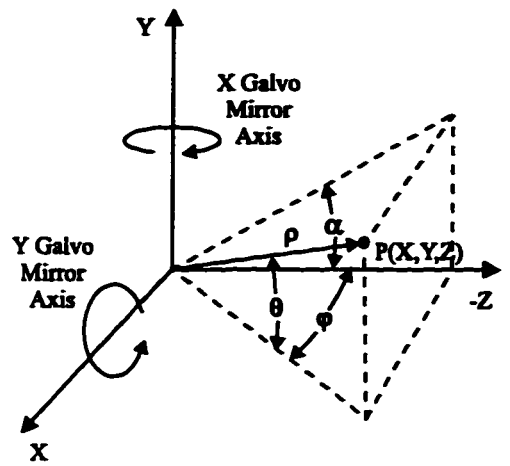

Figure 5.3: Range data correction. The range data is converted from a spherical coordinate system into a Cartesian coordinate system.

5.3 Data Correction

The galvanometer angles are controlled directly by the computer. Range measurements are performed representing the length of the laser beam. For every point, a data triplet corresponding to two deflection mirror angles (α, ϕ) and a range measurement ρ are obtained as shown in Figure 5.3. An important following step involves converting the range data points into intuitive Cartesian coordinates. This is accomplished through the mapping of data points from range scanner coordinates (α, ϕ, ρ), represented by a quasi-spherical coordinate system, into Cartesian coordinates (x, y, z). In a normal spherical system, a point is defined as having three coordinates (θ, ϕ, ρ) as illustrated in the figure. It may be observed that the angle of the X mirror corresponds directly to the ϕ angle of the spherical coordinate system. The angle of the Y mirror however, does not directly map to the θ value of the spherical coordinate system, but instead to its projection angle onto the $Y - Z$ plane. This is related to the fact that the Y galvanometer mirror rotates around a *fixed* horizontal axis and doesn't move with rotation of the other X deflection mirror. The relationship between the θ and α angles is given by:

$$\theta = \arctan(\tan(\alpha)\cos(\phi)) \tag{5.1}$$

Once θ is computed, the x, y, and z coordinates of a given point are obtained from standard spherical-to-Cartesian coordinate system transformations:

$$\begin{aligned} x &= \rho\cos(\theta)\sin(\phi) \\ y &= \rho\sin(\theta) \\ z &= -\rho\cos(\theta)\cos(\phi) \end{aligned} \tag{5.2}$$

This conversion is performed on each of the data points of the image. The image may then be displayed as a point set in 3D space. 3D viewing programs will usually allow moving of the user viewpoint around the point set. The point set may also be triangulated by simply forming small triangles with neighboring points. Triangle normals are then be used for artificial lighting of the imaged object.

5.4 Filtering

In order to eliminate ranging noise, filtering is performed on the 3D range images while the data is still in spherical coordinates (i.e. before the spherical-to-Cartesian data correction). The reason for this early filtering is that the main sensing axis along which the majority of the noise is distributed corresponds to the *range* measurement data coordinate ρ. If the filtering were done after the data correction, the noise would then be distributed along the x, y and z coordinates and would therefore be more difficult to isolate. The main filtering is performed through the use of a standard $n \times n$ median filter. The range image is considered as a flat two dimensional image on a regularly spaced grid whose coordinates corresponds to the α and ϕ angular coordinates of the mirrors. The pixel values of the grid correspond to the range measurement ρ of the data points. By scanning an $n \times n$ mask over the image, the median value of the neighborhood around a point is assigned to that point. Median filtering will usually eliminate very successfully isolated spikes over a neighborhood. In a similar fashion, average filtering could also be implemented. Here, instead of the median, the average range value over a neighborhood is computed. Finally, in order to eliminate the noise at the source, several range measurements may be taken in a fixed location and averaged. Time-varying Gaussian distributed noise will therefore be filtered out. The resulting variance of a measurement with Gaussian distributed noise decreases by a factor $\frac{1}{\sqrt{n}}$ where n is the number of measurements considered in the average.

Chapter 6

Experimentation

6.1 1 DOF Laser Ranging System

The prototype 1 DOF laser ranging unit was built and tested for ranging accuracy and linearity characterization. The original system configuration was built around a 486 DX2, 66 MHz PC with a very inexpensive 12 bit (A/D) converter card. This card had a top sampling rate of only 25 kHz. As a consequence of this low sampling rate, the top modulation frequency of the FM laser diode triangular modulation signal was limited to 60 Hz. This low modulation frequency translates into a one-point sampling time of roughly 0.1 s [1]. For higher accuracy ranging with 10 or 100 averaged range measurements, sampling times of 1 s to 10 s are expected. This is acceptable for the 1 DOF ranging system, but unacceptable for a 3D laser range scanner acquiring images of $128 \times 128 = 16384$ points per image. This would represent an image acquisition time of 27.3 min for a single range measurement per point and 1.89 days for 100 averaged range measurements per point! As a result of this, modifications to the 1 DOF system were made by using a faster, 1 MHz sampling rate 12 bit A/D card. The FM triangular modulation was increased to 5 kHz with the signal acquisition time decreased to 2.5 ms per point. This yields fastest possible image acquisition times of 41 *s* for a 128×128 image with a single range measurement taken per point and of 6.8 min for 10 averaged measurements per point. This by no means constitutes the maximum modulation frequency of the laser diode as they have been modulated up to the GHz frequency range [51] beyond which a sharp rolloff in the transfer function occurs. In practice, the limiting factor

[1] Sampling over a few cycles of the modulation signal is assumed for local averaging and more precise ranging results.

for the maximum FM triangular modulation signal frequency will be the maximum sampling rate of the data acquisition board.

A secondary limiting factor of the maximum achievable modulation frequency is also the gain-bandwidth product of the photodiode amplifier and signal conditioning circuit. Indeed, this circuit must be fast enough to respond to the transient nature of the photodiode signal. In the experimental system, this posed somewhat of a challenge as the existing signal conditioning circuit was simply modified in an ad hoc manner to accommodate this increased signal frequency. Because of this, a very noisy and non-optimal signal was obtained. Ideally, large gain-bandwidth product low-noise operational amplifiers would be used. The experiments were still performed quite successfully, but the maximum range of the system was reduced considerably due to the decreased signal-to-noise ratio (SNR).

Increasing the laser diode modulation frequency also eliminates a mechanical vibration sensitivity problem of the 1 DOF ranging system. Indeed, at 60 Hz, target or laser source vibrations in the order of the wavelength of the laser light give rise to false peaks and modulate the peak amplitude. Depending on the amplitude and potential Gaussian distribution or periodicity of the mechanical vibrations, this may however not be an important issue. Nonetheless, given a high modulation frequency, the relatively short signal sampling time required essentially freezes in time any mechanical motion as the sampling interval becomes negligible in comparison to the period of the mechanical vibrations. This proved to be an effective solution to the vibration sensitivities during experimentations.

6.1.1 Calibration

A necessary step before the 1 DOF laser ranging system may be used involves calibration of the system output into practical useful units. In this case, millimeter units were chosen. A computer-controlled calibration track system was used as shown in Figure 6.1 to displace a target made of a regular white piece of cardboard over a maximum distance of 1.4 m with submillimeter accuracy. The modulation frequency of the laser diode was set at 100 Hz since the bandwidth of the signal conditioning circuit was originally designed and optimized for this frequency range. The higher 5 kHz modulation frequency will require a future redesign of the amplifier and signal conditioning circuit to increase their bandwidth and improve the SNR.

Over a range of roughly 1.4 m, at 50 mm intervals, three different range signals were obtained for comparison. These signals correspond to the cases where 1, 10 and 100 range measurements per point are averaged, as shown

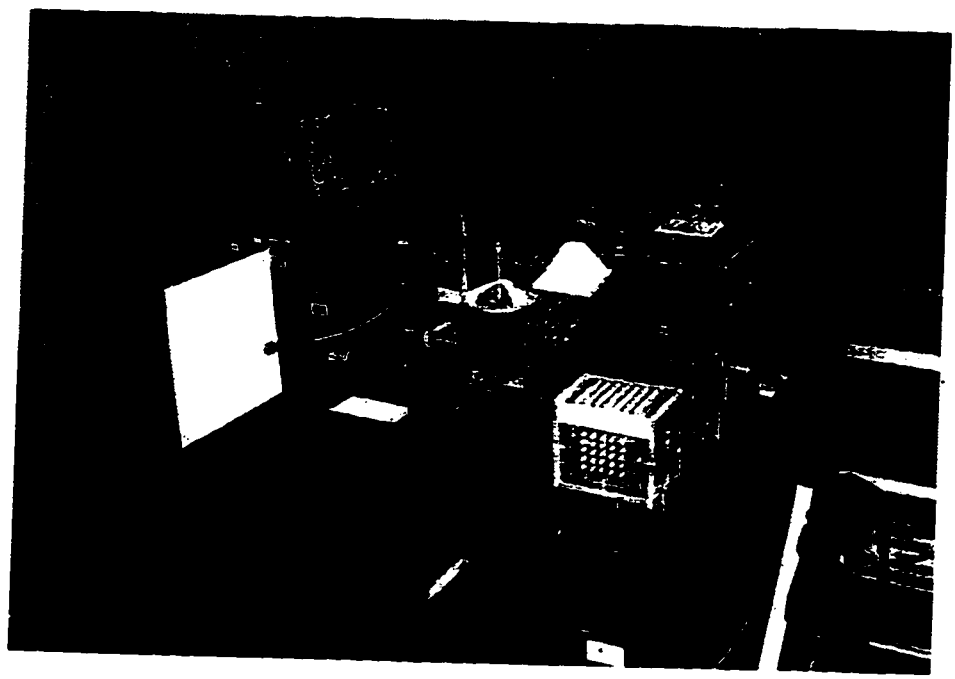

Figure 6.1: 1 DOF calibration table setup

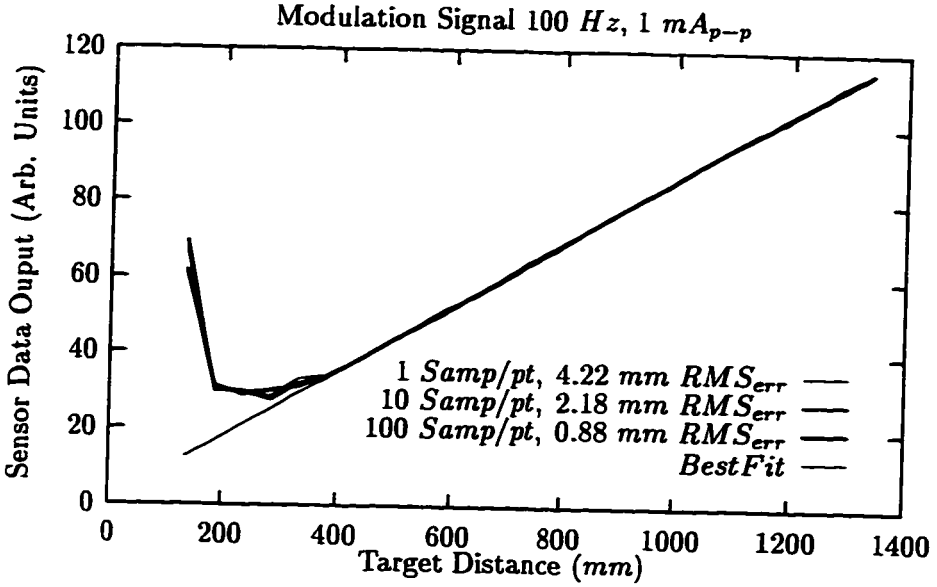

Figure 6.2: 1 DOF ranging calibration curves

in Figure 6.2. At this stage, the uncalibrated range signal measurements simply correspond to the inverse of the average positive and negative peak spacing as described in Equation 3.36. The three curves were measured from 135 mm in front of the laser diode up to an upper range of roughly 1400 mm corresponding to the limits of travel of the linear displacement table. As may be observed from the graph, a linear relationship exists between the ranging data and the target displacement. The initial non-linear excursion of the range data has been determined to be a signal processing artifact. Indeed, for very short excursions, the power fluctuation signal is extremely strong and the superimposed noise causes the false detection of zero crossings by the peak detection algorithm. It was observed experimentally that when a few more filter passes were added, a linear relationship was again observed at this lower end, though long range accuracy was degraded as the weaker signals were completely attenuated by the excessive filtering. Consequently, a tradeoff was chosen. This might suggest the use of alternative filtering techniques to ensure that weak peak signals are not removed by the filtering, while strong signals with significant noise components are adequately filtered before the zero crossings are detected. This poses a problem when long range measurements are performed. The power fluctuation derivative

signal used to recover range information was observed experimentally on an oscilloscope up to a target distance of roughly 5 m beyond which it was lost in the background noise. The detection and processing of the signal by the computer however stopped long before, at around 2 m at which point the amplitude was small enough so that the digitized signal had become much too distorted distorted to be accurate.

Since the relationship between the range data and the target displacement is highly linear, a simple linear regression is performed to recover the calibration parameters used to convert the range data into proper millimeter units. To this effect, a linear regression was performed through each of the three curves to find the slope and offset of the best-fitting curve. These two parameters are then used to convert the inverse average positive and negative peak spacing (range data) into a calibrated range measurement in millimeter units according to the following relation:

$$\text{Range(mm)} = \frac{\text{avg. peak spacing} - \text{best fit curve offset}}{\text{best fit curve slope}} \tag{6.1}$$

Note that the measurements from the graph before 485 mm were not used in the linear regression given the software signal processing configuration. It will therefore constitute the near ranging limit.

Linearity measurements were performed over the linear range sensing curve regions by finding the RMS error with respect to the best fit curves. In the case of a single measurement taken for every target position, an RMS error of 4.22 mm was found over the entire 485 mm to 1335 mm range. In the case where 10 measurements were averaged in every target position, an RMS error figure of 2.18 mm was obtained. Finally, when 100 measurements were averaged, an RMS error of 0.88 mm over the entire range was measured.

6.1.2 Target Reflectance Effects on Ranging Accuracy

In time-of-flight ranging systems, the return beam intensity fluctuation is typically responsible for severe distortions of the ranging signal. In order to observe the effects of decreasing levels of backscattered laser light, a polarizing filter was placed between the laser diode and a fixed target. The filter was rotated through 90^o at 5^o interval, producing a gradual attenuation of the return beam until complete attenuation was reached. At every point, 100 range measurements were averaged. The range data thus obtained is shown in Figure 6.3. The graph shows that the range measurements of a target placed at 337 mm in front of the laser diode are unaffected for polarization angles under 30^o. When the attenuation is larger however, the nonlinear

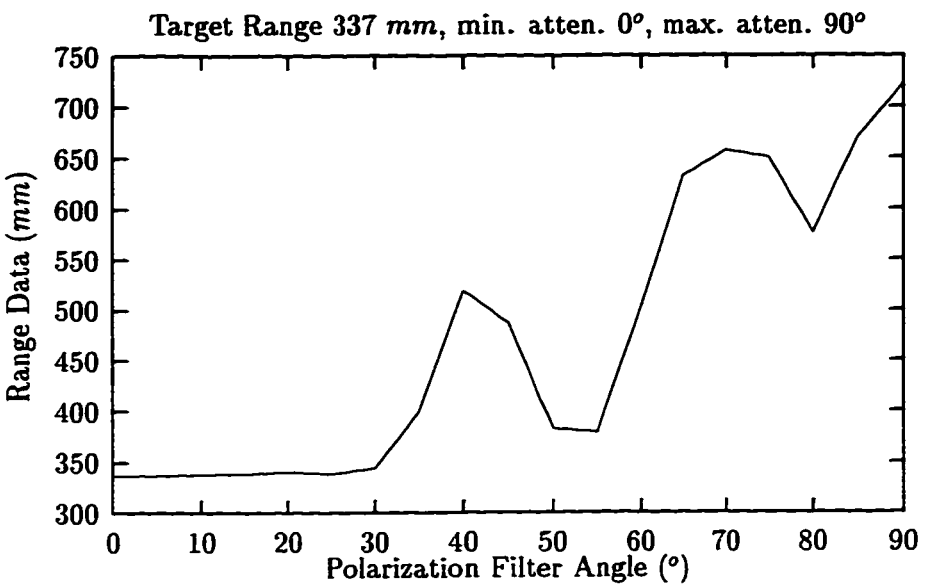

Figure 6.3: Ranging signal for fixed target given varying signal strength. A polarizing filter was used to attenuate the laser beam. The graph shows the ranging output over a filter rotation range of 90° given a fixed target at 337 mm.

jumps shown are an indication of the signal not being processed properly by the algorithm due to its small amplitude. Zero crossings are missed, or misidentified as a result of signal corruption. Indeed, after one filter pass, the peaks of the derivative signal are often eliminated. Note, however that it is possible to measure beyond the 30^o mark by eliminating the software filtering step. Nonetheless, eventually the signal becomes much too weak to be digitized adequately. As the signal was increasingly attenuated, the size of the peaks of the derivative signal displayed on an oscilloscope were observed to decrease as predicted by the theoretical model until the peaks disappeared when the signal was completely blocked.

6.1.3 Temperature Effects on Ranging Accuracy

Another interesting experiment performed involved the observation of the temperature sensitivity of the range measurements in order to determine empirically whether temperature regulation is really necessary. Using the temperature controller itself, the temperature setpoint was adjusted as to sweep a 14^oC temperature excursion with 1^o increments. A fixed target was placed in front of the laser diode at 337 mm and 100 range measurements were averaged for every point. Figure 6.4 illustrates the results. As the temperature increases, an upward trend in the range data is observed. Note that this data may also be partially affected by the peak detection technique. In general, the important is to choose a temperature operating point away from mode hops so that FM noise is reduced and stable linear modulation excursion as a function of input current exists. The graph shows the need for temperature regulation if the scanner is to be used in an environment where large temperature fluctuations occur, though not necessarily with a $\pm 0.001^oC$ accuracy. If the scanner is to be used in an enclosed area with reasonably steady temperature, then the temperature regulation might not be necessary, given of course an adequate initial machine warm-up time period.

6.1.4 Error Sources

One of the major hurdles of the 1 DOF laser ranging unit is laser speckle. This proves to be a major obstacle in most laser-based systems. Laser speckle is produced by the laser being reflected by a "rough" surface in comparison to the wavelength of the laser light. Most surfaces fall into this category. Some parts of the beam are reflected at different positions due to the uneven surface. This in turn induces a relative phase shift an results

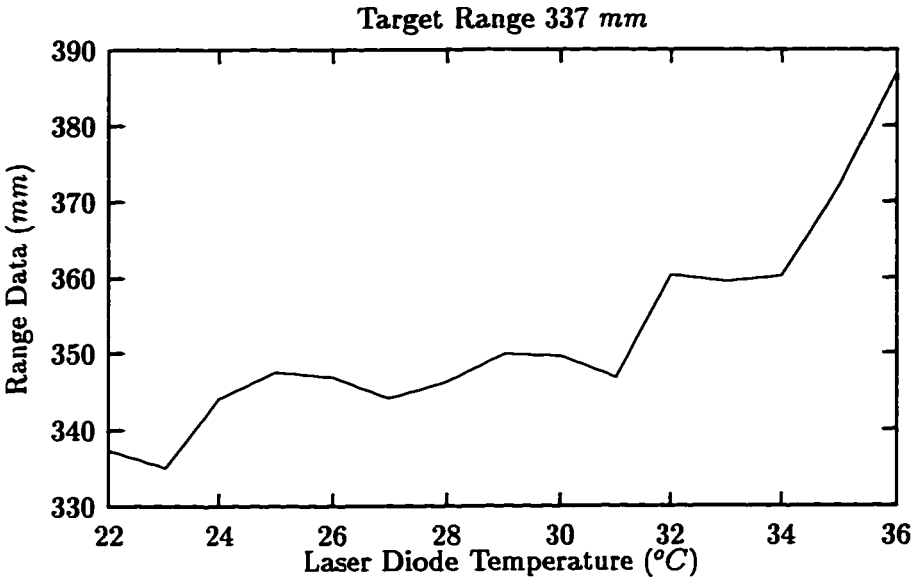

Figure 6.4: Temperature sensitivity of range measurements

in constructive and destructive interference throughout the return beam. This gives rise to the trademark "grainy" texture observed when a laser beam is reflected off a diffuse surface. Effectively, some areas of the return beam cross-section are highly attenuated through destructive interference and some others are brighter through constructive interference. With the self-mixing effect, since the laser diode's internal photodiode detects power fluctuations induced by backscattered laser light, some positions in relation to a diffuse reflector will result in negligible laser light feedback. In in some other positions, the light feedback will be very important. The speckle pattern is extremely sensitive to target motion, including lateral displacement. In practice, when directing the laser diode beam towards a target and monitoring the output power derivative signal, the resulting peaks are constantly in "motion" due to minute vibrations of either the target or the source. In some cases, the peaks can go from a strong level to an extremely weak level and back while the beam is aimed at a fixed spot. This effect becomes fairly important at long ranges where the feedback light intensity is already small to begin with. For closer distances, however, the natural vibrations of the target or source seem to vary the pattern such that when averaged over a number of measurements, the resulting range measure is accurate.

The second important source of error lies in the signal filtering and peak detection algorithm. Indeed, when the signal strength is weak, but still observable, the filtering completely removes the peaks in the derivative signal. When the signal is very strong, several filter passes are needed in order to avoid misidentification of zero crossings caused by signal noise. Overall, a different software filtering approach which does not depend on the signal strength should be used. Alternatively, an adaptive technique could also be developed whereby the number of filter passes are predetermined by a figure of merit of the input signal.

6.2 X-Y Laser Range Scanner

After coupling the calibrated 1 DOF laser ranging unit to X-Y galvanometers, the control program was modified to output galvanometer angle control signals through the two D/A converter output lines on the data acquisition board. The mirror angles swept were of approximately 12 degrees in both directions. The program was also modified to automatically control the mirror angles and perform signal acquisition and data processing as to save the range and angle measurements to file in ASCII format. Two separate programs are later used to filter and correct the ASCII file and output the range image in both MATLAB and VRML 3D file formats.

6.2.1 3D Ranging Error Measure

In order to quantify the 3D ranging error, a plane was placed in front of the laser range scanner at roughly 555 mm and its range image was taken at 10 measurements per point as illustrated in Figure 6.5. Note that the plane was at a slight angle with respect to the vertical as the beam was scanned in a region above the horizon due to the galvanometer setup. The image shown was median filtered with a 7×7 filter size in spherical coordinates and corrected with the model described in Section 5.3. A multiple linear regression was performed in order to fit a plane within the range data. RMS error measurements were then obtained. For the raw unfiltered sensor data, an RMS error figure of 10.2 mm over the entire plane was obtained. For the 7×7 median-filtered image shown in Figure 6.5, a 0.87 mm RMS error over the plane was obtained. This median filtering will be used for subsequent images. The reason for which the median filter produces such a drastic improvement in terms of accuracy is owed to the fact that the major noise component over the range image consists of random isolated spike noise when signal dropout occurs.

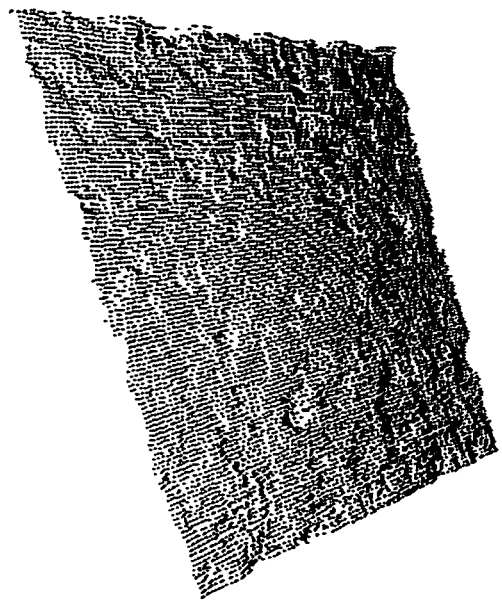

Figure 6.5: Range image of a reference plane

An observation should be made at this point. Since the sensing axis along which the error is distributed corresponds to the laser beam axis, the ranging errors along the $-z$ axis will be largest when the beam is perpendicular to the surface to be imaged, that is when the laser beam axis is aligned with the $-z$ axis. As the beam is steered away from this perpendicular beam, the ranging error becomes distributed along the x, y and $-z$ axis through the correction operation such that the error along the $-z$ axis at the edges of a range image is reduced though the x and y errors are increased.

Imaging of specular (reflective) surfaces proved to be problematic as it is for any other laser-based ranging system. The problem lies in the fact that most of the laser energy is reflected in an arbitrary direction usually away from the sensor and the backscattered light component is usually negligible. As a result, signal dropout was observed when images of reflective surfaces were taken.

6.2.2 Error Sources

As the galvanometers scan a scene, the laser spot is constantly in motion. The resulting laser speckle produces signal dropout for certain range points in the 3D image. As a result, the signal processing algorithm is not able to accurately detect the peak spacing and wrong range results occur. Overall this results in random spike noise over the image. This is why median filtering produces such a drastic improvement in the RMS error figure of the plane range image shown earlier. Median filtering is very good at eliminating isolated outliers in a given neighborhood. Alternatively, the outliers could be simply identified and marked as invalid points as is usually done with other scanners. The identification or segmentation is not particularly difficult as the spikes are usually large in size in comparison to most of the other data points.

6.2.3 Range Images

Here is a sampling of a few 3D range images acquired by the 3D laser range scanner. The images are all of size 128×128 and were all median filtered with a 7×7 filter size. The acquisition distance to the objects was roughly 700 mm. Figure 6.6 shows the range image of a small corrector fluid bottle. Several rotated views are shown to visually convey the true 3D structure of the range data. Here the range images are displayed as sparse point clouds. Figure 6.7 shows the range image of the plaster cast of a hand.

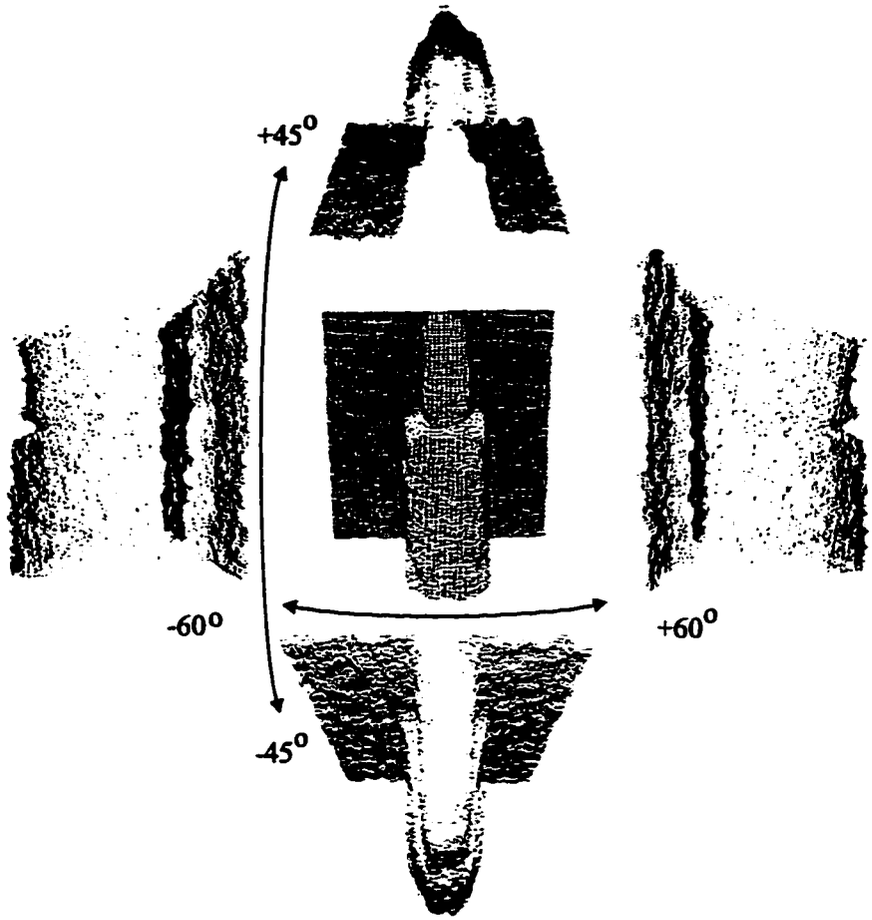

Figure 6.6: Range image of a corrector fluid bottle shown with a few rotated views conveying the 3D structure of the data

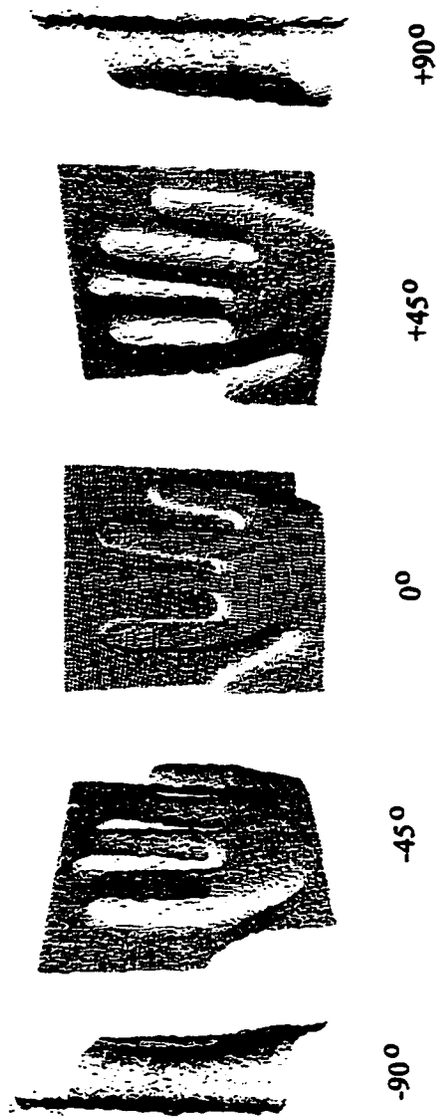

Figure 6.7: Rotated views showing range image of the plaster cast of a hand.

As an alternative rendering method to the sparse point cloud, it is possible to connect neighboring 3D data points to form discrete polygonal patches filling the gaps between these points, thus producing better looking images. At the same time, local polygon normals may be used to produce artificial shading based on a virtual light source placed in the scene. Triangulation is an example of a polygonal surface approximation where neighboring data points are used as vertices of small triangles. Figure 6.8 A) shows a range image of a pyramid displayed in point cloud format. After being triangulated, the same image is displayed with flat shading B) where the brightness of each triangle is set to a unique value related to the triangle's orientation with respect to the light source. This produces an intuitive 3D image; nonetheless, connecting lines between triangles appear. An alternative technique in C) called Gouraud shading allows for a gradation of brightness across each triangle so that a smooth and continuous brightness progression occurs between neighboring triangles through interpolation. This results in a smooth, apparently continuous surface to the observer. Figure 6.9 illustrates the range image data and Gouraud shaded rendering of the front-end of a miniature Porsche toy car.

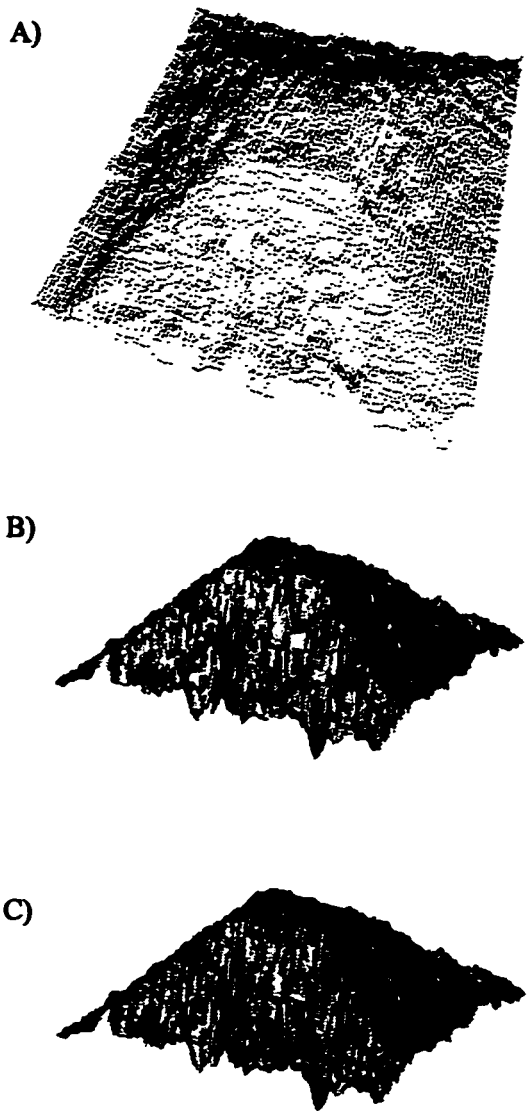

Figure 6.8: Range image of a pyramid showing rendering techniques. A) Range data displayed as point cloud. B) Triangulated image with flat artificial shading. C) Triangulated image with interpolated Gouraud shading.

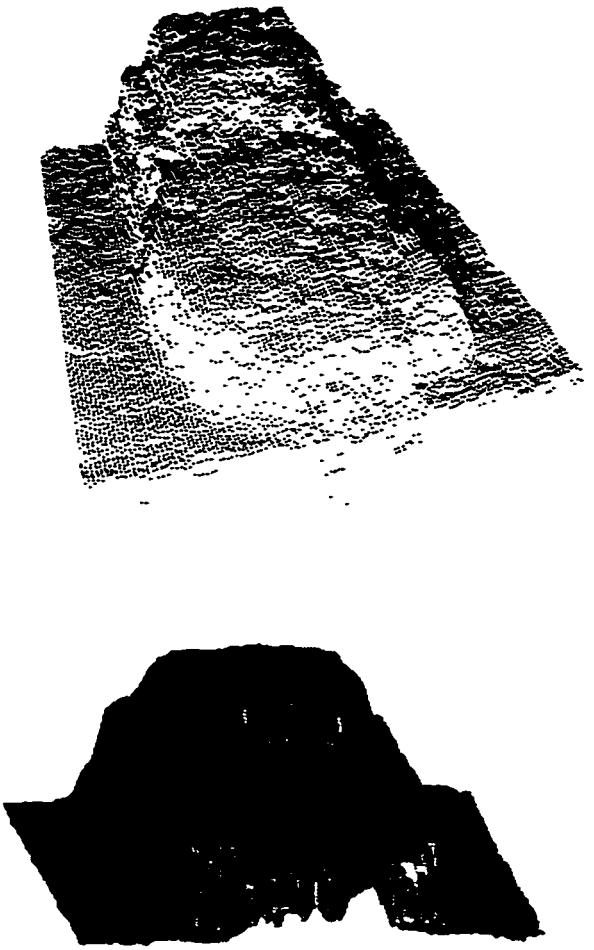

Figure 6.9: Range image of the front-end of a miniature Porsche toy car

Chapter 7

Conclusion

The theory and design of a low-cost portable and accurate three-dimensional laser range scanner based on the self-mixing effect in a laser diode was developed and presented. In this special 3D range scanner, a simple low-cost laser diode was used both as a sensor and as a laser light source.

The benefits of this system over existing laser-based systems are numerous. First, the use of a simple laser diode as a source and sensor yields a very low-cost solution to the ranging problem. No external optical sensing elements (i.e. CCD array) are required to compute range information. The coaxial nature of the source and detector also eliminates shadowing problems associated with triangulation laser range scanners. The coherent detection technique also ensures constant ranging errors over the useful workspace unlike triangulation-based systems. An added benefit of using the self-mixing effect lies in the possibility to obtain velocity as well and range information from a single measurement. Also, interferometric scale measurements are possible by using the system in a fixed frequency regime.

The major disadvantage of the technique lies in the laser speckle problem which reduces dynamic range of the sensor. Speckle paterns are influenced by the target surface roughness and are modulated by mechanical vibrations. A second limitation of the technique related to the maximum mesurable range involves the coherence length of the laser. This coherence length is a fundamental property of the lasing device.

This work constitutes only the second known implementation of a 3D laser range scanner based on the self-mixing effect. An extension to the existing theory on the self-mixing effect in laser diodes has been presented in order to obtain theoretical curves matching the experimental curves obtained. Considerable insight into the self-mixing effect was gained from the

analysis of the developed theoretical model. Consequently, the 3D laser range scanner prototype was operated at a considerably higher laser diode modulation frequency than first planned in order to solve a mechanical sensitivity problem. Four novel circuits were devised to control the functions of the low-cost laser range scanner. A high accuracy ($\pm 1 \mu A$) circuit with protection features was designed to drive the laser diode and amplify the signal from the internal monitor photodiode. A high accuracy temperature controller ($\pm 0.001^{\circ}C$ accuracy) was designed based on a thermoelectric device for temperature stabilization of the laser diode for high frequency stability. A signal conditioning circuit was designed to enhance the detected interferometric signal for digital processing. A high stability digital triangular signal generator circuit was designed as the signal source for the modulation. Finally, a new signal processing algorithm was devised to automatically detect the mode hop spacing and calculate target range and velocity.

Experimentation on the prototype system was performed in two steps. First, precise characterization of the solitary 1 DOF laser ranging system was performed over a range of roughly 485 mm to 1400 mm using a computerized calibration table. RMS ranging errors of 0.88 mm over this range were measured by averaging 100 samples per point. The second stage of experimentation involved the addition of a beam steering unit to the 1 DOF ranger. A white cardboard target was placed in front of the range scanner at a distance of 555 mm in order to characterize the accuracy of the 3D range scanner. A 3D range image of the target was acquired. A correction model was developed and used to convert the data from the scanner's quasi-spherical coordinate system into Cartesian coordinates. Through fitting of a 3D plane within the range data, RMS errors of 10.2 mm over the plane were obtained from the raw sensor data. After filtering of the image, RMS errors of 0.87 mm were obtained. It was observed that the major noise component within the range images consisted of random spike noise consistent with signal dropout caused mainly by laser speckle. Several other range images were acquired and rendered by approximating the sampled surface with discrete polygonal patches defined from the range data, and allowing for artificial shading.

The major interest in the use of laser diodes for metrology is based on their low-cost, compactness, ease of use, and mostly versatility. In fact, through the theory developed, it was shown that a simple laser diode may be used to recover range information to a target along with velocity information (including directional discrimination) with the FM modulation technique presented. Moreover, interferometric scale measurements are also possible by setting a fixed current setpoint, thus a fixed output frequency.

Target motion then induces well-know fringe shifts corresponding to target displacements of $\frac{\lambda}{2}$, where λ is the wavelength of the laser light. By adding an external beam-splitter and a photodiode, it is also possible to measure the intensity of the return beam. The ability to resolve all those quantities with good accuracy in a single measurement makes this approach very appealing.

The developed low-cost 3D range scanner has a variety of possible applications. The field of robotics for example, faces numerous difficult challenges which may potentially be solved through the use of 3D vision. Autonomous navigation, environment mapping, automated task execution are a few of these problems. In other areas, 3D vision also has promising applications: reverse engineering (automated CAD model generation), rapid prototyping, automated assembly line quality control inspection, and motion analysis to name a few. Over the past decade, the emergence of 3D range scanning technology has proven to generate a tremendous amount of interest within the academic community where range scanning has superseded conventional stereo vision, and also within the industry where the technology has opened a whole new range of possibilities.

Bibliography

[1] M. Rioux, *Digital 3-D imaging: theory and applications* SPIE Proceedings, Videometrics III, International Symposium on Photonics and Sensors and Controls for Commercial Applications, Boston, MA. vol. 2350, pp. 2-15, Oct. 31-Nov. 4, 1994.

[2] M. Rioux, *Digital images of shapes* Proceedings of the First International Conference on Range Image Standard and Range Image Toolboxes, Villeurbanne, France. pp. 14-16, Oct. 14-15, 1993.

[3] G. Godin, G. Roth, and P. Boulanger, *Using laser geometric sensing for rapid product development* Proceedings of the Intelligent Manufacturing Systems International Conference on Rapid Product Development, Stuttgart, Germany, pp. 403-416, Jan. 31-Feb. 2, 1994.

[4] M. Rioux, *Color 3-D electronic imaging of the surface of the human body* SPIE Proceedings, Automatic Systems for the Identification and Inspection of Humans, San Diego, CA. vol. 2277, pp. 42-54, Jul. 28-29, 1994.

[5] D.A. Simon, M. Hebert, and T. Kanade, *Real-time 3-D pose estimation usig a high-speed range sensor* IEEE International Conference on Robotics and Automation, San Diego, CA. pp. 2235-2240, May 8-13, 1994.

[6] D.G. Laurin, M. Rioux, *Three dimensional object tracking from range images using sine wave coding and fourier transform* SPIE Proceedings, Videometrics II, Boston, MA. vol. 2067, pp. 252-265, Sept. 7-10, 1993.

[7] M. Rioux, G. Godin, F. Blais, and R. Baribeau *Differential inspection of shapes using optical 3-D measurements* Optical 3-D Measurement Techniques II: Applications in Inspection, Quality Control and Robotics, Zurich, Switzerland. pp. 402-409, Oct. 4-7, 1993.

[8] F.R. Livingstone, L. King, J.-A. Beraldin, and M. Rioux *Development of a real-time laser scanning system for object recognition, inspection, ans robot control* SPIE Proceedings, Telemanipulator Technology, and Space Telerobotics, Boston, MA. vol. 2057, pp. 454-461, Sep. 7-10, 1993.

[9] E. Gagnon, J.-F. Rivest, M. Greenspan, and N. Burtnyk, *A computer-assisted range image registration system for nuclear waste cleanup* IEEE Instrumentation and Measurement Technology Conference, Brussels, Belgium. vol. 1, pp. 106-110, Jun. 4-6, 1996.

[10] T. Bosch, N. Servagent, and R. Chellali, *A scanning range finder using the self-mixing effect inside a laser diode for 3-D vision* IEEE Instrumentation and Measurement Technology Conference, Brussels, Belgium. vol. 1, pp. 226-231, Jun. 4-6, 1996.

[11] L. Korba, W. McMath, and S. Yeung, *Range sensor array for an experimental mars rover* Proceedings of the Knowledge-Based Systems and Robotics Workshop, Ottawa, Ont., pp. 39-45, Nov. 14-17, 1993.

[12] L. Korba, S. Elgazzar, and T. Welch, *Active infrared sensors for mobile robots* IEEE Trans. Instrum. Meas., vol. 43, no. 2, pp. 283-287, 1994.

[13] D. Mackay, R. Liscano, L. Korba, and S. Elgazzar, *Vehicle control for underground mine navigation* Proceedings of the 1995 Summer Computer Simulation Conference, Ottawa, Ont., Jul. 24-26, 1995.

[14] A. Kosaka, and J. Pan, *Purdue experiments in model-based vision for hallway navigation* Proceedings of the Workshop on Vision for Robots in IROS'95 Conference, Pittsburgh, PA. pp. 87-96, 1995.

[15] K.S. Fu, R.C. Gonzalez, C.S.G. Lee *Robotics: control, sensing, vision, intelligence* McGraw-Hill, ISBN 0-07-022625-3, 1987.

[16] W.M. Wang, K.T.V Grattan, W.J.O. Boyle, and A.W. Palmer, *Active optical feedback in a dual-diode laser configuration applied to displacement measurements with a wide dynamic range* Appl. Opt., vol. 33, No. 10, pp. 1795-1800, April 1994.

[17] G. Beheim, *Fiber-optic interferometer using frequency-modulated laser-diodes* Appl. Opt., vol. 25, No. 19, pp. 3469-3472, Oct. 1986.

[18] S.F. Collins, W.X. Huang, M.M. Murphy, K.T.V. Grattan, and A.W. Palmer, *Ranging measurements over a 20 metre path using an intensity-chirped laser diode* Meas. Sci. Technol. 5, pp. 753-755, 1994.

[19] R.A. Jarvis, *A perspective on range finding techniques for computer vision* IEEE Trans. Pattern Anal. Machine Intell., vol. PAMI-5, no. 2, pp. 122-139, 1983.

[20] M. Rioux, F. Blais, J.A. Beraldin, and P. Boulanger *Range imaging sensors development at NRC laboratories* Proceedings of the IEEE Workshop on Interpretation of 3D Scenes, Austin, TX. pp. 154-160, Nov. 27-29, 1989.

[21] R.A. Jarvis, *A laser time-of-flight range sanner for robotic vision* IEEE Trans. Pattern Anal. Machine Intell., vol. PAMI-5, no. 5, pp. 505-512, 1983.

[22] M.J. Rudd, *A laser doppler velocimeter employing the laser as a mixer-oscillator* J. Scientif. Instrum., vol. 1, pp. 723-726, 1968.

[23] W.M. Wang, W.J.O. Boyle, K.T.V. Grattan, and A.W. Palmer, *Self-mixing interference inside a diode laser: experimental observations and theoretical analysis* Appl. Opt., vol. 32, pp. 1551-1558, 1993.

[24] E.T. Shimizu, *Directional discrimination in the self-mixing type laser Doppler velocimeter* Appl. Opt., vol. 26, pp. 4541-4544, Nov. 1987.

[25] P.J. de Groot, G.M. Gallatin, and S.H. Macomber, *Ranging and velocimetry signal generation in a backscatter-modulated laser diode* Appl. Opt., vol. 27, No. 21, pp. 4475-4480, 1988.

[26] H.W. Jentink, F.F.M de Mul, H.E. Suichies, J.G. Aarnoudse, and J. Greve, *Small laser Doppler velocimeter based on the self-mixing effect in a diode laser* Appl. Opt., vol. 27, No. 2, pp. 379-385, 1988.

[27] J.H. Churnside, *Laser Doppler velocimetry by modulating a CO_2 laser with backscattered light* Appl. Opt., vol. 23, pp. 61-65, 1984.

[28] J.H. Churnside, *Signal-to-noise in a backscatter-modulated Doppler velocimeter* Appl. Opt., vol. 23, pp. 2079-2106, 1984.

[29] Y. Mitsuhashi, T. Morikawa, K. Sakurai, and J. Shimada, *Self-coupled optical pickup* Opt. Commun., vol. 17, pp. 95-97, Apr. 1976.

[30] A. Dandridge, R.O. Miles, and T.G. Giallorenz, *Diode laser sensor* Electron. Lett., vol. 16, pp. 948-949, 1980.

[31] G. Beheim, and K. Fritch, *Range finding using frequency-modulated laser diode* Appl. Opt., vol. 25, pp. 1439-1442, 1986.

[32] S. Shinoara, H. Yoshida, H. Ikeda, K.-I. Nishide, and M. Sumi, *Compact and high-precision range finder with wide dynamic range and its application* IEEE Trans. Instrum. Meas., vol. 41, no. 1, pp. 40-44, 1992.

[33] M.K. Koelink, M. Slot, F.F.M. de Mul, J. Greve, R. Graaff, A.C.M. Dassel, and J.G. Aarnoudse, *Glass-fiber self-mixing diode laser Doppler velocimeter* Meas. Sci. Technol., vol. 3, pp. 33-37, 1992.

[34] T. Morikawa, Y. Mitsuhashi, and J. Shimada, *Return-beam induced oscillations in self-coupled semiconductor lasers* Electron. Lett., vol. 12, pp. 435-436, Aug. 1976.

[35] I. Ikushima, and M. Maeda, *Self-coupled phenomena of semiconductor lasers caused by a optical fiber* IEEE J. Quantum Electron., vol. QE-14, pp. 331-332, May. 1978.

[36] N. Chinone, K. Aiki, and R. Ito, *Stabilization of semiconductor laser outputs by a mirror close to a laser facet* Appl. Phys. Lett., vol. 33, pp. 990-992, Dec. 1978.

[37] R. Lang, K. Kobayashi, *External optical feedback effects on semiconductor injection laser properties* IEEE J. Quant. Electron., vol. QE-16, pp. 347-355, Dec. 1980.

[38] G.A. Acket, D. Lenstra, A.J. den Boef, and B.H. Verbeek, *The influence of feedback intensity on longitudinal mode properties and optical noise in index-guided semiconductor lasers* IEEE J. Quantum Electron. QE-20, 1163-1169 (1984).

[39] J.H. Osmundsen, and N. Grade, *Influence of optical feedback on laser frequency spectrum and threshold conditions* IEEE J. Quant. Electron. vol. QE-19, pp. 465-469, 1983.

[40] W.M. Wang, K.T.V. Grattan, A.W. Palmer, and W.J.O. Boyle, *Self-mixing interference inside a single-mode diode laser for optical sensing applications* J. Lightwave Technol., vol. 12, no. 9 pp. 1577-1587, 1994.

[41] D. Lenstra, B.H. Verbeek, and A.J. Den Boef, *Coherence collapse in single-mode semiconductor lasers due to optical feedback* IEEE J. Quant. Elec., vol. QE-21, no. 6, pp. 674-679, June 1985.

[42] S. Shinohara, A. Mochizuki, H. Yoshida, and M. Sumi, *Laser Doppler velocimeter using the self-mixing effect of a semiconductor laser diode* Appl. Opt., vol. 25, No. 9, pp. 1417-1419, 1986.

[43] S. Shinoara, H. Naito, H. Yoshida, H. Ikeda, and M. Sumi, *Compact and versatile self-mixing type semiconductor laser Doppler velocimeters with direction-discrimination circuit* IEEE Trans. Instrum. Meas., vol. 38, no. 2, pp. 574-577, 1989.

[44] J. Mark, E. Bodtker, and B. Tromborg, *Measurement of Rayleigh backscatter-induced linewidth reduction* Electron. Lett., vol. 21, pp. 1008-1009, 1985.

[45] J.S. Cohen, and D. Lenstraa, *Spectral properties of the coherence collapsed state of a semiconductor laser with delayed optical feedback* IEEE J. Quant. Elec., vol. 25, no. 6, pp. 1143-1151, June 1989.

[46] J.S. Cohen, F. Wittgrefe, M.D. Hoogerland, and J.P. Woerdman, *Optical spectra of a semiconductor laser with incoherent optical feedback* IEEE J. Quant. Elec., vol. 26, no. 6, pp. 982-990, June 1990.

[47] W.A. Hamel, M.P. van Exeter, and J.P. Woerdman, *Coherence properties of a semiconductor laser with feedback from a distant reflector: experiment and theory* IEEE J. Quant. Elec., vol. 28, no. 6, pp. 1459-1469, June 1992.

[48] J.T. Verdeyen, *Laser electronics,* 3^{rd} *ed.* Prentice Hall Series in Solid State Physical Electronics, ISBN 0-13-706666-X, 1995.

[49] K. Petermann, *Laser diode modulation and noise.* Dordrecht, The Netherlands: Kluwer Academic, ISBN 90-277-2672-8, 1988.

[50] M.K. Koelink, M. Slot, F.F.M. de Mul, J. Greve, R. Graaff, A.C.M. Dassel, and J.G. Aarnoudse, *Laser doppler velocimeter based on the self-mixing effect in a fiber-coupled semiconductor laser: theory* Appl. Opt. 31, 3401-3408 (1992).

[51] A. Dandridge, and L. Goldberg, *Current-induced frequency modulation in diode lasers* Electron. Lett. 18, 302, 1982.

[52] L. Goldberg, H.F. Taylor, and J.F. Weller, *Time-dependant thermal effects in current-modulated semiconductor lasers* Electron. Lett. 17, pp. 497-499, 1981.

[53] S. Kobayashi, Y. Yamamoto, and T. Kimura, *Modulation frequency characteristics of directly optical frequency modulated AlGaAs semiconductor lasers* Electron. Lett. 17, pp. 350-351, 1981.

[54] S. Donati, L. Falzoni, S. Merlo, *A PC-interfaced, compact laser-diode feedback interferometer for displacement measurements* IEEE Trans. Instrum. Meas., vol. 45, no. 6, pp. 942-947, 1996.

[55] C.E. Wieman, L. Hollberg, *Using diode lasers for atomic physics* Rev. Sci. Inst., vol. 62, no. 1, pp. 1-21, January 1991.

[56] C.C. Bradley, J. Chen, and R.G. Hulet *Instrumentation for the stable operation of laser diodes* Rev. Sci. Inst., vol. 61, no. 8, pp. 2097-2101, August 1990.

[57] P. Horowitz, and W. Hill, *The art of electronics* 2^{nd} ed., Cambridge University Press, Cambridge, 1989.

[58] K.G. Libbrecht, J.L. Hall, *A low-noise high-speed diode laser current controller* Rev. Sci. Inst., vol. 64, no. 8, pp. 2133-2135, August 1993.

[59] M.S. Cafferty, E.D. Thompson, *Stable current supply with protection circuits for a lead-salt laser diode* Rev. Sci. Inst., vol. 60, no. 9, pp. 2896-2901, September 1989.